NOTE TO USERS

This reproduction is the best copy available.

UMI

University of Alberta

Third-Order Nonlinearities of Novel *iso*-Polydiacetylenes Studied by a Differential Optical Kerr Effect Detection Technique

By

Aaron David Slepkov ©

A thesis submitted to the Faculty of Graduate Studies and Research in partial fulfilment of the requirements for the degree of Master of Science

Department of Physics

Edmonton, Alberta

Spring 2002

National Library of Canada
Acquisitions and Bibliographic Services
395 Wellington Street
Ottawa ON K1A 0N4
Canada

Bibliothèque nationale du Canada
Acquisitions et services bibliographiques
395, rue Wellington
Ottawa ON K1A 0N4
Canada

Your file Votre référence

Our file Notre référence

The author has granted a non-exclusive licence allowing the National Library of Canada to reproduce, loan, distribute or sell copies of this thesis in microform, paper or electronic formats.

L'auteur a accordé une licence non exclusive permettant à la Bibliothèque nationale du Canada de reproduire, prêter, distribuer ou vendre des copies de cette thèse sous la forme de microfiche/film, de reproduction sur papier ou sur format électronique.

The author retains ownership of the copyright in this thesis. Neither the thesis nor substantial extracts from it may be printed or otherwise reproduced without the author's permission.

L'auteur conserve la propriété du droit d'auteur qui protège cette thèse. Ni la thèse ni des extraits substantiels de celle-ci ne doivent être imprimés ou autrement reproduits sans son autorisation.

0-612-69759-2

Canada

University of Alberta

Library Release Form

NAME OF AUTHOR:	Aaron David Slepkov
TITLE OF THESIS:	Third-Order Nonlinearities of Novel *iso*-Polydiacetylenes Studied by a Differential Optical Kerr Effect Detection Technique
DEGREE:	Master of Science
YEAR THIS DEGREE GRANTED:	2002

Permission is hereby granted to the University of Alberta Library to reproduce single copies of this thesis and to lend or sell such copies for private, scholarly or scientific research purposes only.

The author reserves all other publication and other rights in association with the copyright in the thesis, and except as herein before provided neither the thesis nor any substantial portion thereof may be printed or otherwise reproduced in any material form whatever without the author's prior written permission.

Aaron Slepkov.

Aaron David Slepkov
Department of Physics
University of Alberta
Edmonton, AB
Canada T6G 2J1

January 3rd, 2002

Writing is an adventure. To begin with, it is a toy and an amusement. Then it becomes a mistress, then it becomes a master, then it becomes a tyrant. The last phase is that just as you are about to be reconciled to your servitude, you kill the monster and fling him to the public.

-Winston Churchill

University of Alberta

Faculty of Graduate Studies and Research

The undersigned certify that they have read, and recommend to the Faculty of Graduate Studies and Research for acceptance, a thesis entitled **Third-Order Nonlinearities of Novel iso-Polydiacetylenes Studied by a Differential Optical Kerr Effect Detection Technique** submitted by **Aaron David Slepkov** in partial fulfillment of the requirements for the degree of Master of Science

Dr. Frank Hegmann

Dr. Rik Tykwinski

Dr. John Beamish

Dr. Frank Marsiglio

DATE: January 3rd, 2002

ABSTRACT

We have studied the third-order optical nonlinearities of an iso-polydiacetylene (iso-PDA) oligomer series. The iso-PDAs are composed of a cross-conjugated framework, and as such offer the opportunity to study the differences between electronic communication in standard linearly-conjugated systems and novel cross-conjugated systems. This is the first study of third-order nonlinearities as a function of cross-conjugated path length. The examination of optical properties in iso-PDAs is further augmented with UV-Vis absorption spectra, and the linear absorption of these samples is also studied as a function of cross-conjugated path length. We have found that as the number of repeat units is increased, the low-energy wavelength of maximum absorption, λ_{max}, does not increase appreciably, and, in fact, saturates by the heptamer sample. On the other hand, the second hyperpolarisabilities of these samples are seen to increase linearly as a function of chain length, suggesting contributions from the fixed length linearly-conjugated arms, rather than the extension of a cross-conjugated path. The largest nonlinearities were observed in the heptamer sample with a second hyperpolarisability relative to the THF solvent of $\gamma_{heptamer}/\gamma_{THF} = (181\pm9)$. In addition, Non-instantaneous dynamics are observed in the samples. This behaviour arises in the oligomers' Kerr response roughly 0.4 ps after maximum pump-probe overlap and is not present in the solvent signal.

The ultrafast third-order nonlinearities were measured with 100 fs, 800 nm pulses at a repitition rate of 1 kHz using a new Kerr gate that represents a modification to the standard optical heterodyne detection optical Kerr effect (OHD-OKE) technique. This

technique, called DOKE (differential optical Kerr effect) detection, offers signals that are linear with the pump beam intensity. Furthermore, DOKE detection offers an elegant means by which the real and imaginary components of the nonlinearities may be separated. This work presents an extensive description and characterisation of this new Kerr gate arrangement.

Acknowledgements

Let me first thank my supervisor, Dr. Frank Hegmann. Frank is always excited about the research in the lab and his enthusiasm is quite contagious. I thank him for pushing me to attend conferences, make posters and get our work published. I particularly thank you, Frank, for finding me research that is both suitable for a chemist and a physicist—a task that required you to brush up on another discipline! I would also like to thank my committee. Dr. Rik Tykwinski, my co-supervisor has provided me with a great collaboration. Rik, you have always treated me with more patience than I deserved, thank you! Dr. John Beamish, whom I have often treated as my personal guidance councillor, has not once told me to go away—something even my wife has to do every so often. Furthermore, John's extensive knowledge in experimentation has impacted my research directly, a fact he will soon be aware of when he reads a certain Appendix. Thanks John, for all of your help. Finally, Dr. Frank Marsiglio, who became a last minute committee member despite having no room on his plate. Thanks, Frank, for having eyes bigger than your stomach.

I have tremendous respect and gratitude for Dr. Kenji Kamada, who is an old hand at the optical Kerr effect, and who has precipitated the success with my research. Kenji, you have provided me guidance and support, but mostly, you gave me confidence to navigate uncharted waters –thank you!

My thanks go to Lynn Chandler who acted as a guardian angle throughout my degree. Lynn, thank you for all of your help! In addition, Don Mullin and Tony Walford, two extremely apt Tradesmen, have my utmost gratitude for their help, service, and instruction when it came to building or designing anything. I would like to acknowledge the work of Yuming Zhao, who synthesised all of our organic samples. Yuming has been a great collaborator, always taking my senseless deadlines in stride. Yuming, you make the synthesis of these oligomers seem deceptively easy! I would like to thank my colleague and friend Tobias Herman. Toby, I know you're sick of the same "Nonlinear Optics" slide that I make you edit for every talk. I promise you'll never have to see it again. Finally, I thank Kristine Lui, my lab-mate and good friend. Kris, you are always so

meticulous in your work. You have helped me choose to work towards research that is fundamentally correct, rather than superficially flashy.

A year ago I would have thanked my girlfriend Emily DiBattista who has always given me so much love and support. She is single-handedly responsible for my not quitting during the first eight months at the U of A. Thank you, Emily, my wife!

Generous funding was provided by NSERC and the University of Alberta.

TABLE OF CONTENTS

QUOTE: WINSTON CHURCHILL

ABSTRACT

LIST OF TABLES

LIST OF FIGURES

1 INTRODUCTION 1

1.1 MOTIVATION 1
1.2 NONLINEAR OPTICS 5
1.2.1 Third-order susceptibility, $\chi^{(3)}$ 5
1.2.2 Molecular Hyperpolarisabilities: 8
1.3 THE OPTICAL KERR EFFECT: 10
1.3.1 Standard Optical Kerr Gates: 11

2 DIFFERENTIAL OPTICAL KERR EFFECT (DOKE) 16

2.1 DOKE LAYOUT 16
2.2 DOKE FORMULATIONS 19
2.3 DOKE SIGNAL DETECTION 22
2.3.1 Finding The Zero Probe Delay time (τ_D=0) Stage Setting 23

3 PRELIMINARY WORK: DOKE SETUP CHARACTERISATION 24

3.1 BEAM DIAGNOSTICS 24
3.1.1 Beam Autocorrelation 25
3.1.2 Spatial Beam Profiles 29
3.1.3 Laser Power and Alignment Drifts 31
3.2 OPTICAL KERR GATE: CHARACTERISATION 34
3.2.1 Power Laws 34
3.2.2 DOKE Polarisation Conditions 38

4 EXPERIMENTAL 40

4.1 SAMPLE PREPARATION 40
4.1.1 Cross-conjugated iso-polydiacetylene oligomer series 41
4.2 CONCENTRATION TESTS 42
4.3 CUVETTE EFFECTS AND BLANK MEASUREMENTS 45
4.4 COMPARING RESULTS WITH THE LITERATURE 48

5 RESULTS AND DISCUSSION 50

5.1 ABSOLUTE REFERENCE AND THF NONLINEARITIES 50
5.2 SCAN SERIES 51
5.3 OLIGOMER SERIES NONLINEARITIES 53
5.3.1 Time-Resolved Scans 53
5.3.2 On-Peak Scans 54
5.3.3 Sample Second Hyperpolarisabilities 56
5.3.4 A Non-Instantaneous Sample Response Component 60

6 CONCLUSIONS 62

7 FUTURE DIRECTIONS 64

APPENDIX A **65**

LOCK-IN AMPLIFIER CONSIDERATIONS 65
LINE FILTERS 65

APPENDIX B **67**

PUMP BEAM REFERENCE DETECTION 67

APPENDIX C **69**

OHD-OKE AND DOKE SIGNAL DETECTION 69
STANDARD OHD-OKE 70
DOKE 73
A GRAPHICAL COMPARISON 77

APPENDIX D **79**

KERR SIGNALS FROM VARIOUS MATERIALS 79
Carbon Tetrachloride, CCl_4 ..... *79*
Carbon Disulphide, CS_2 ..... *81*
Amorphous Arsenic-Doped Selenium *82*

APPENDIX E **85**

BALANCED PHOTODIODE SCHEMATICS AND CALIBRATIONS 85
Schematics *85*
Calibration *86*
"A+B" to "A"+"B" Calibration *86*
A+B as a post-sample probe reference *87*

APPENDIX F **89**

CONCENTRATION NORMALISATION OF $\chi^{(3)}$ SIGNAL IN FIGURE 5.4 89

APPENDIX G **91**

SAMPLE CALCULATIONS FOR $\chi^{(3)}_{THF}$ AND γ_{THF} 91

REFERENCES **93**

LIST OF TABLES

Table 5.1: Summary of results for the iso-polydiacetylene oligomer series. . γ_s and γ_{THF} are the second hyperpolarisabilities of the oligomer samples and THF reference, respectively. n is the number of repeat units in the oligomer. 57

Table C.1: Some symbols and matrix representations for various optical elements. 70

Table G.1: A list of values to be used in calculating $\chi_{THF}^{(3)}$ and γ_{THF} 91

LIST OF FIGURES

Figure 1.1: Resonance structures for a conjugated organic system. (a) Three conjugation paths along the molecule; residual groups R_1 and R_3 are trans to each other and linearly-conjugated along path "a". Residual groups R_2 and R_3 are cis to each other and linearly-conjugated along path "b". Residual groups R_1 and R_2 are geminally linked along cross-conjugated path "c". (b) description of how resonance structures can be viewed with electron delocalisation. (c) Four resonance contributors: (i) is the most stable and prominent contributor; (ii) and (iii) are also contributors, and (iv) is highly unstable and improbable as a realistic resonance contributor. (Adapted from Tykwinski et. al. 1998 [13]) 4

Figure 1.2: Two Optical Kerr Effect Detection Techniques. (a) The standard Heterodyne detection layout, with fully crossed polarisers. The sample is pumped at 45 degrees to the analyser polarisation. A birefringence is induced in the sample between the dirctions parallel and perpendicular to the pump polarization. (b) The optically heterodyned detection arrangement. The polariser is rotated by a small (heterodyne) angle, θ, allowing some "local oscillator" light into the Kerr-gate. A quarter-wave plate is inserted in the probe beam, oriented with fast axis perpendicular to the analyser. The pumping and birefringence conditions are congruent to the homodyne setup. 15

Figure 2.1: Schematic of the differential optical Kerr effect (DOKE) detection layout. PD-A: rejected probe beam photodiode detector; PD-B: transmitted probe beam photodiode detector; PD-C: probe reference photodiode detector; BS-1: beam splitter; BS-2: Brewster's Window as a beam splitter; $\lambda/4$: quarter-wave plate; $\lambda/2$: half-wave plate; D: D-mirror; P: Glan-laser polariser; A: Glan-laser polariser as an analyser; L: lens; S: sample cell; CH: chopper; PC: computer. 16

Figure 2.2: A close-up of the DOKE detection layout. The single photodiode detector of the homodyne and heterodyne detection schemes is replaced by differential detectors, analysing the full probe beam intensity. The quarter-wave plate is oriented to give circular probe polarisation at the sample. 17

Figure 2.3: The $\sin^2(\phi)$ describing the transmitted light from a polariser-analyser pair, uncrossed by angle ϕ. The starting points for three detection techniques are shown, where an induced birefringence would represent a small movement along the curve, $\delta\phi$. The dashed line shows the linear regime. 21

Figure 3.1: BBO second-harmonic autocorrelation signals at the sample location for various compressor settings. The shortest pulse is observed at a compressor setting of 19.5mm. The longest, most degraded, pulse is observed at 15.5mm. 26

Figure 3.2: THF Kerr signals for different compressor settings: Note that the signals are not entirely symmetric. However, the asymmetries are very small and the FWHM is a good representation of the pulse duration providing an in situ autocorrelation method. 28

Figure 3.3: Pump and probe spatial beam profiles. (a) Spatial profile of the probe beam, showing a spot size of 235 μm and (b) spatial profile of the pump beam, showing a spot size of 490 μm. Solid lines are Gaussian fits, showing near-ideal spatial profiles. 30

Figure 3.4: Drawing of spatial profile detection equipment: The photodiode detector is behind a 25 μm pinhole that is attached to a x-y adjustable mount. The entire setup is on a variable z stage, giving 3-dimensional mobility. The beam is scanned along the x-direction, yielding the beam's spatial, cross-sectional, profile. 32

Figure 3.5: Kerr Signals for a scan series showing the effects of drift in laser pointing. The composition but not the concentrations of samples #1-3 should be ignored. The arrow illustrates how both a lowering and time-shifting of the signal is observed. 33

Figure 3.6: Dependence of DOKE signal on pump beam powers for (a) a dilute iso-polydiacetylene dimer sample in THF and (b) a CS_2 reference sample. Nonlinearities are kept below $\sin\phi < 0.2$. Lines are regression fits, showing good linear behaviour. 35

Figure 3.7: Dependence of DOKE signal on pump beam power for a THF standard. The solid line is a guide to the eye showing good signal linearity to well above 10 mW. 36

Figure 3.8: Dependence of DOKE signal on probe beam power for a dilute iso-polydiacetylene dimer sample in THF. Nonlinearities are kept below $\sin\phi < 0.1$. The solid line is a regression fit, showing good linear behaviour. 37

Figure 3.9: CS_2 Kerr signals for the four DOKE polarisation conditions. This is an example of a sample with no $\mathrm{Im}(\chi^{(3)})$ component. 38

Figure 4.1: Chemical structure of the *iso*-polydiacetylene oligomers showing (a) the monomer, (b) the repeat unit, and (c) the heptamer sample. The longest linearly-conjugated segment present in the $n \geq 2$ molecules is shown as a thick line in the heptamer structure..... 41

Figure 4.2: (a) UV-Vis absorption spectra of the oligomer samples at the concentrations used for the OKE studies. The scale shows that the absorption edge, λ_0 has nearly saturated by the heptamer (n = 7) sample. (b) The full absorption spectrum for the oligomer samples, n is the number of repeat units in the sample. The lowest energy wavelength of maximum absorption, λ_{max}, does not appreciably shift from the dimer to the heptamer..... 42

Figure 4.3: Concentration test for an iso-polydiacetylene dimer. A concentration of 0M represents a pure THF blank. Dashed line is a linear fit showing excellent linearity in this concentration range..... 44

Figure 4.4: Depth of focus (D.O.F) and Gaussian beam waist (W_0). (a) A gradual focus allows for a long depth of focus, and the entire sample cell experiences a similar beam intensity profile. (b) A sharp focus with a short depth of focus; the sample in the centre experiences a markedly different intensity profile than the outer cell walls. The depth of focus is the range over which the beam diameter, W, is smaller than $\sqrt{2} \times W_0$. 47

Figure 4.5: A comparison of Kerr signals from a THF sample, a 2.5mm sample of Quartz, and an empty quartz sample cuvette. 47

Figure 5.1: Time-resolved Kerr response of THF reference/solvent and iso-PDA oligomer sample solution. The molarity of each sample in THF is indicated in square brackets..... 54

Figure 5.2: On-peak A-B (nonlinear Kerr response) and A+B (probe reference) signals for a monomer sample. The nonlinear response shows considerably more noise than the probe reference signal. Dashed lines are guides to the eye.. 55

Figure 5.3: Molecular second hyperpolarisability of the oligomer samples, γ_S, relative to the absolute THF hyperpolarisability, γ_{THF}, as a function of oligomer repeat length, n. The solid line is a linear fit to the data for n = 2, 3, 5, and 7 (dimer to heptamer). 57

Figure 5.4: Magnified view of the tail region of the Kerr response for the oligomer samples showing a non-instantaneous excitation feature at 0.4 ps. The size of the hump increases with n, but remains at the same temporal position for all samples. The dotted line is a THF reference showing no deviation from smooth signal decay. To emphasise the presence of the hump, Kerr signals for each sample have been normalised to the monomer concentration. The hump does not appear at negative time delays..... 61

Figure A.1: CS_2 Kerr signals for various lock-in amplifier Line filter settings, showing significant signal removal. 66

Figure B.1: Pump beam reference detection layout. The pump beam is split by a glass window set at Brewster's angle, and sent downwards from the 6" height to the 3" height. Pump beam is initially polarised vertically. 68

Figure C.1: Transmitted light through the Kerr gate for three detection techniques. δ, is the heterodyning angle, where the homodyne technique operates at $\delta=0$. The OHD-OKE signal is shown for a heterodyning angle of 15°..... 78

Figure D.1: Kerr response of CCl_4 showing the excitation of phonon modes. (a) Time-resolved CCl_4 Kerr signal and (b) the FFT spectrum of the Kerr response, showing the excitation of two modes at 220 cm^{-1} and 313 cm^{-1}. 80

Figure D.2: Kerr signals from CS_2 and CCl_4 standards. Inset: semi-log plot showing a 1.72 ps relaxation time (straight line) in the tail of the CS_2 signal. 81

Figure D.3: DOKE responses of a 0.3 mm thick sample of arsenic-doped selenium and THF (for comparison). In addition, the post-sample probe reference signals, A+B, are provided..... 82

Figure D.4: Absorption spectrum of a 0.3 mm arsenic-doped selenium sample, showing considerable absorption at 800 nm. 83

Figure D.5: FFT spectrum of the Kerr response of a 0.3 mm thick, amorphous, sample of arsenic-doped selenium. A vibrational mode is excited at 243 cm^{-1}. 84

Figure E.1: A schematic of the balanced photodiodes detector used for our DOKE measurements. All details needed to build a suitable replica are provided. 85

1 INTRODUCTION

1.1 Motivation

A nonlinear optical (NLO) process is one in which light alters the optical properties of a medium with which it interacts. In most cases these changes are only noticeable when intense light is used. With the emergence of laser technology, intense monochromatic light is easily generated, and many nonlinear optical phenomena have been observed in the last four decades [1]. Some second-order nonlinear optical processes include frequency doubling, optical rectification, optical parametric amplification, sum and difference frequency generation, and photorefractive effects. Second-order NLO processes have been studied extensively and their current uses abound in the field of laser research. Third-order optical processes include self-focusing, third-harmonic generation and optically induced birefringence. The latter, also known as the optical Kerr effect (OKE), is particularly interesting in its applicability to all-optical switching. All-optical processes are predicted to replace electronics as the next evolution in computing [2,3]. In all-optical switching, light beams act both as the traffic controllers and as the vehicles for information. With the advent of femtosecond light pulses, all-optical processes are orders of magnitude faster than electronics [4]. Bringing all-optical switching to fruition hinges on finding a material with proper third-order nonlinear optical properties. There is no set standard for such criteria; however, the material of choice will require adequate transparency at the desired optical frequencies, as well as a large light-induced phase shift. The latter property depends on the third-order bulk susceptibility, $\chi^{(3)}$.

In the past, researchers have scrambled to find the material with highest $\chi^{(3)}$ or molecular second hyperpolarisability, γ. At present, the race has not yielded a material with suitable properties, but, early on, the benefit of delocalised electronic structure has pointed towards π-conjugated organics as potential candidate materials. Organic compounds such as oligomers and chromophores have high optical transparency,

synthetic versatility, rapid response times and low cost as added advantages towards application viability.

The role of π-electron delocalisation path lengths in polymers has been studied extensively[5]. It has been found that extending the linear-conjugation in oligomers by increasing the number of double and triple bonds significantly increases the oligomer's nonlinearities [3,5,6]. However, a major obstacle to finding viable polymeric materials is the "nonlinearity-transparency trade-off" [7]. Although polymers with high nonlinearities, such as the polydiacetylenes have been discovered as the linearly-conjugated path length is increased, the opacity of the polymer also increases [8,9], rendering these materials less suitable for practical applications. Increasing the conjugation-length provides a longer delocalisation path, lowering the electronic band gap. This means that the molecule's absorption edge, λ_0[*] shifts to higher wavelengths. Furthermore, long linearly-conjugated polymers are typically unstable in the lab [8].

It is doubtful that the current trend of trying to maximise γ solely by increasing the conjugation path will lead to the material of choice for all-optical switching purposes. With this realisation, several research groups have identified the need to study a variety of material aspects that give rise to third-order nonlinearities. A useful library of structure-property relationships of π-conjugated systems is needed. Some properties previously studied include symmetry, pendant functionality and planarity [11-15]. A major aspect of γ processes in these systems is the electronic delocalisation itself. The role of electronic conjugation has been identified as crucial to nonlinear optical processes, yet the π-electron communication processes in $\chi^{(3)}$ materials have been inadequately studied.

---

[*] Note: λ_{max} is the lowest energy wavelength of maximum absorption. λ_0, on the other hand, is the low energy absorption edge, and is defined as the wavelength at which the absorption edge slope intersects the wavelength axis. Often, these two quantities are used interchangeably, representing the band-gap energy of the molecule. However, for compounds with exitonic levels between the valence and conduction bands, the distinction between λ_0 and λ_{max} becomes important, with λ_{max} corresponding to the band-gap energy [10].

Studies examining various aspects of pendant functionality on a conjugated framework confirm that communication efficiencies follow the trend *trans>cis>>geminal* in compounds of the type presented in Figure 1.1 [13]. These studies find that while trans and cis groups contribute relatively equally to $\chi^{(3)}$, the geminal position is nearly inactive. This is attributed to the fact that the trans and cis groups are part of a linearly-conjugated π-bridge over which delocalised electrons are fairly free to polarise. With the aid of resonance structures, it is seen that electrons are delocalised over a linearly-conjugated path. Figure 1.1 presents an example of an organic system that contains both linearly-conjugated and cross-conjugated paths. In Fig. 1.1 (c), we see that stable resonance contributors may be drawn for both the trans and cis configurations. Here, electronic communication may be envisioned between residual groups R_1 and R_3 in the trans configuration, and between R_1 and R_4 in the cis configuration. However, resonance structures that involve communication over the cross-conjugated bridge (between R_1 and R_2, for example) are high in energy and are not realistic contributors [16]. Thus, valence bond theory predicts very little π-delocalisation across the cross-conjugated bridge. However, other bonding models, such as molecular orbital (MO) theory, reveal that some communication across such a bridge is possible [16]. Since studying the electronic nonlinearities in organic molecules tells us about π-electron communication in such systems, studies of nonlinearities in cross-conjugated oligomers may help better describe the extent of electronic delocalisation over cross-conjugated bridges.

With the compilation of specific engineering aspects of $\chi^{(3)}$ and γ in mind, we have sought to study more closely the role of cross-conjugated π-electron communication in third-order optical nonlinearities of organic systems. With cross-conjugated communication expected to be the weakest link in a conjugated $\chi^{(3)}$ material, it is crucial to study this particular structure-property relationship. Constructing materials for practical $\chi^{(3)}$ applications will require careful engineering of all molecular aspects, particularly those aspects that may typically hinder the third-order nonlinear responses.

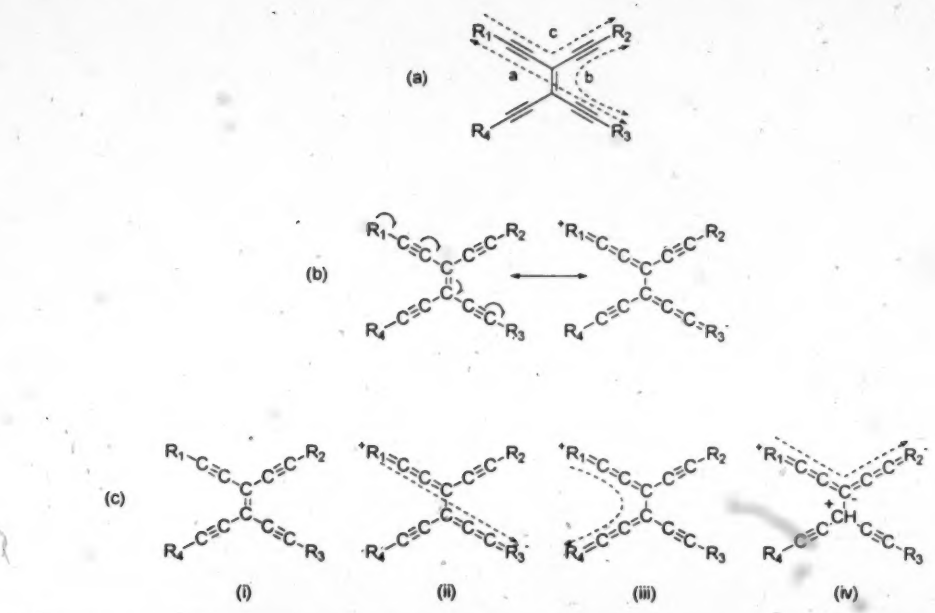

Figure 1.1: Resonance structures for a conjugated organic system. (a) Three conjugation paths along the molecule; residual groups R_1 and R_3 are trans to each other and linearly-conjugated along path "a". Residual groups R_2 and R_3 are cis to each other and linearly-conjugated along path "b". Residual groups R_1 and R_2 are geminally linked along cross-conjugated path "c". (b) description of how resonance structures can be viewed with electron delocalisation. (c) Four resonance contributors: (i) is the most stable and prominent contributor; (ii) and (iii) are also contributors, and (iv) is highly unstable and improbable as a realistic resonance contributor. (Adapted from Tykwinski et. al. 1998 [13])

A second motivation for studying oligomers with cross-conjugated backbones arises from their two-dimensional nature. In linearly-conjugated molecules, increasing their 1-D nature by adding double and triple bonds increases $\chi^{(3)}$ while shifting the absorption edge to higher wavelengths, as mentioned above. However, it has been shown that in such systems, moving out dendritically towards two dimensions does not significantly increase the absorption wavelength [13]. Similarly, systems composed of a cross-conjugated backbone and linearly-conjugated paths hatching out to two dimensions should afford an increase in $\chi^{(3)}$ due to the increased number of linearly-conjugated paths, while the absorption wavelength edge, λ_0, should remain relatively constant. As the

number of repeat units is increased in the cross-conjugated oligomer, the overall number of linearly-conjugated paths increases, while the longest linearly-conjugated path remains of constant length (as is discussed later in §4.1.1).

This work presents the first optical Kerr effect studies on a novel cross-conjugated iso-polydiacetylene-based oligomer series. The relationship between the oligomeric length and the third-orderoptical nonlinearities ($\chi^{(3)}$ and γ) are explored. Furthermore, the "nonlinearity-transparency trade-off" is examined by comparing UV-vis absorption spectra as the oligomer chain length is increased.

In addition to presenting the nonlinear optical properties of this oligomer series, this work reports the construction and use of a new optical Kerr-gate detection layout. The technique is dubbed differential optical Kerr effect (DOKE) detection, and represents a significant modification to a more widely used technique called optical heterodyne detection optical Kerr effect (OHD-OKE) [17].

1.2 Nonlinear Optics

1.2.1 Third-order susceptibility, $\chi^{(3)}$

Nonlinear optical processes are those in which light interacts with a medium to change the medium's optical properties.

At low electric fields, the polarisation of a material, $\vec{P}$, is linear with the applied electric field, E, according to:

$$\vec{P} = \varepsilon_0 \chi \cdot \vec{E}, \tag{1.1}$$

where χ is the linear susceptibility of the material and ε_0 is the permittivity of free-space. At higher electric fields, the polarisation is no longer strictly linear with susceptibility and is represented by a power series expansion in the electric field as

$$\vec{P} = \varepsilon_0\left(\chi^{(1)} \cdot \vec{E} + \chi^{(2)} : \vec{E}\vec{E} + \chi^{(3)} \vdots \vec{E}\vec{E}\vec{E}\right) + \ldots \tag{1.2}$$

where, $\chi^{(1)}$, $\chi^{(2)}$ *and* $\chi^{(3)}$ are the first-order, second-order and third-order susceptibilities and are second, third and fourth rank tensors, respectively. In general, the second-, third-, and higher-order susceptibilities are progressively much smaller than the linear susceptibility. With typical field intensities, $\chi^{(1)}E:\chi^{(2)}E^2:\chi^{(3)}E^3 \approx 1:10^{-6}:10^{-12}$, thus requiring extremely large optical fields in order to observe nonlinear effects.

Inserting an electric field represented by

$$E = E_0 \cos(\omega t - kz) \tag{1.3}$$

into Eq. 1.2 gives

$$\begin{aligned} P &= \varepsilon_0\left(\chi^{(1)}E_0\cos(\omega t - kz) + \chi^{(2)}E_0^2\cos^2(\omega t - kz) + \chi^{(3)}E_0^3\cos^3(\omega t - kz)\right) \\ &= \varepsilon_0\chi^{(1)}E_0\cos(\omega t - kz) + \frac{1}{2}\varepsilon_0\chi^{(2)}E_0^2\left(1 + \cos(2\omega t - 2kz)\right) \\ &\quad + \varepsilon_0\chi^{(3)}E_0^3\left(\frac{3}{4}\cos(\omega t - kz) + \frac{1}{2}\cos(3\omega t - 3kz)\right) \end{aligned} \tag{1.4}$$

Clearly, by allowing such nonlinear terms beyond Eq. 1.1, the interaction of intense light with matter can manifest new wavelengths of light, including a constant, DC component.

The first term in Eq. 1.4 is the linear term. The second term is a $\chi^{(2)}$ term and is frequency independent. This term gives rise to optical rectification [18]. The other $\chi^{(2)}$ term is a 2ω term and gives rise to second harmonic generation. The fourth term is $\chi^{(3)}$ dependent and contains the original frequency ω. It is this term which is of main interest to this report since it gives rise to the optical Kerr effect. Finally, the last term is also a third-order, $\chi^{(3)}$ process that gives rise to third-harmonic generation. In general, $\chi^{(3)}$ is comprised of both real and imaginary components. $\mathrm{Re}(\chi^{(3)})$ terms lead to self-action effects arising from the intensity-dependent change in refractive index, while $\mathrm{Im}(\chi^{(3)})$ terms give rise to attenuative processes such as two-photon absorption [18].

Experimentally, this work is interested in those processes occurring at the original optical frequency, ω;

$$P = \varepsilon_0 \chi^{(1)} E_0 \cos(\omega t - kz) + \frac{1}{2}\varepsilon_0 \chi^{(2)} E_0^2 + \frac{3}{4}\varepsilon_0 \chi^{(3)} E_0^3 \cos(\omega t - kz). \quad (1.5)$$

The second order susceptibility $\chi^{(2)}$ (as all even-ordered terms in the expansion) is symmetry controlled, and can be shown to vanish for centrosymmetric systems [19]. The first-order and third-order terms (as all odd-ordered terms in the expansion) are present for all symmetries, including the case of the isotropic mediums studied in this work. Comparing Eqs. 1.1 and 1.5, and accounting for the symmetry arguments given above we may define an effective susceptibility of

$$\chi_{eff} = \chi^{(1)} + \frac{3}{4}\chi^{(3)} E_0^2. \quad (1.6)$$

Typically, the index of refraction is given by

$$n_0^2 = \varepsilon_r = 1 + \chi, \quad (1.7)$$

where ε_r is the relative dielectric constant of the material. Thus, by analogy, the "new" index of refraction, containing nonlinear terms, may be described by

$$n^2 = 1 + \chi_{eff} = 1 + \left(\chi^{(1)} + \frac{3}{4}\chi^{(3)} E_0^2 \right). \quad (1.8)$$

The purely nonlinear component in the index of refraction is therefore

$$n^2 - n_0^2 = \frac{3}{4}\chi^{(3)} E_0^2. \quad (1.9)$$

Recalling that the nonlinear index change, $\Delta n = n - n_0$ is much smaller than n_0 yields an expression for an intensity-dependent index of refraction,

$$n = n_0 + \frac{3}{8}\frac{\chi^{(3)} E_0^2}{n_0}$$
$$= n_0 + \frac{3\chi^{(3)}}{4c\varepsilon_0 n_o^2} I, \tag{1.10}$$

when defining the intensity as $I = \frac{E_0^2 c \varepsilon_0 n_0}{2}$, where c is the speed of light, and ε_0 is the permitivitty of free space. Thus, the typical definition of the Kerr effect as an intensity dependent, optically-induced birefringence, is given by

$$\Delta n = n - n_0 = \frac{3\chi^{(3)}}{4c\varepsilon_0 n_o^2} I = n'_2 I. \tag{1.11}$$

The preceding relationships are in SI units, where n'_2 has units of m^2/W and $\chi^{(3)}$ has units m^2/V^2. Currently, it is quite popular to report $\chi^{(3)}$ in esu units, while reporting n'_2 in SI units. Hence a useful definition of $\chi^{(3)}$ is

$$n_2(SI) = \frac{120\pi^2}{c n_o^2}\chi^{(3)}(esu) = \frac{3.9\times10^{-6}}{n_o^2}\chi^{(3)}(esu). \tag{1.12}$$

1.2.2 Molecular Hyperpolarisabilities:

The preceding discussion of macroscopic material polarisability may be extended to microscopic systems and molecules. In analogy to Eq. 1.1, the microscopic polarisability is typically given by the dipole moment,

$$\vec{p} = \mu = \varepsilon_0 \alpha \cdot \vec{E}, \tag{1.13}$$

and may be written in general to have higher order terms,

$$\vec{p} = \varepsilon_0 \left(\alpha \cdot \vec{E} + \beta : \vec{E}\vec{E} + \gamma : \vec{E}\vec{E}\vec{E} + ... \right) \tag{1.14}$$

where α, β and γ are known as the linear polarisability, first hyperpolarisability and second hyperpolarisability and are the tensor counterparts of $\chi^{(1)}$, $\chi^{(2)}$ and $\chi^{(3)}$, respectively. However, the microscopic polarisabilities α, β and γ have molecular co-ordinate systems which may be entirely different than those of the macroscopic susceptibilities, having laboratory co-ordinate axes.

The same symmetry arguments follow for the molecular polarisabilities as those previously described for the susceptibilities. Thus, non-centrosymmetric molecules will have a β component. However, for molecules studied in solution, or any centrosymmetric media, the second-order term will be suppressed by isotropic averaging and only $\chi^{(1)}$ and $\chi^{(3)}$ terms will contribute [18]. Thus, extracting molecular polarisabilities from studies on macroscopic systems yield only those components allowed by the symmetry of the medium studied. Extracting molecular coefficients from studies on bulk materials is further complicated by local field effects [20]. This "local field effect" is an intensification of the external optical electric field felt by the solute and is due to the "reaction field" on the solute by the solvent orientation. The local field relates the macroscopic polarising electric field to the actual polarising (including depolarisation) field 'felt' by the molecules. Precisely accounting for this local field is complicated. However, in the case of non-interacting, non-polar, solutions (or pure liquids) of anisotropic symmetry, the Lorentz field factor is widely used and considered quite accurate [18,21]. The Lorentz factor is given by

$$L(\omega) = \frac{n_0^2(\omega) + 2}{3}. \tag{1.15}$$

This factor modifies the electric field in the solution such that E is generally replaced by E x L when electric field effects on the solute molecules are desired. Since the macroscopic susceptibility $\chi^{(3)}$ is a summed average of all the molecular hyperpolarisabilities, it is possible to relate $\chi^{(3)}$ to γ by [18]

$$\chi^{(3)} = L^4 N_c \langle \gamma \rangle, \tag{1.16}$$

where N_c is the molecular number density in cm^{-3} and $\langle \gamma \rangle$ is the orientationally averaged second-order hyperpolarisability. [22]

In the case of dilute sample solutions, assuming that the two species are non-interacting, the sample third-order susceptibility $\chi^{(3)}$ is considered a superposition of the independent component susceptibilities. Thus, if one knows the solvent $\chi^{(3)}_{solvent}$, one can extract the solute hyperpolarisabilities from

$$\chi^{(3)} = L^4 \left[N_{c\,(solute)} \langle \gamma_{solute} \rangle \right] + \chi^{(3)}_{solvent}. \tag{1.17}$$

Note that this equation assumes that the number of solute molecules is small enough in comparison to the solvent molecules that they do not affect the solvent molecules and that the solvent concentration is unaltered from purity, allowing $\chi^{(3)}_{solvent}$ to be used.

1.3 The Optical Kerr Effect:

As discussed above, the optical Kerr effect (OKE) is an optically induced birefringence. Specifically, polarised light interacts with an isotropic medium modifying the index of refraction along the axis of polarisation [23]. This induces an anisotropy in the material and produces a sample with different indices of refraction along and orthogonal to the incident pumping polarisation. Consequently, other, differently polarised beams incident on the pumped sample "see" this birefringence and may

experience phase retardations leading to an overall rotation in polarisation. This type of pump-probe spectroscopy gives us information about the strength of the third-order nonlinearity of the sample.

1.3.1 Standard Optical Kerr Gates:

In a standard (homodyne) Kerr gate [24] an intense, linearly polarised pump pulse excites a birefringence in an isotropic medium. This change in the index of refraction, $\delta n = n_{//} - n_{\perp}$, between the parallel and perpendicular axes to the pump polarisation can be probed by a weaker pulse that is polarised at 45° to the exciting pulse as seen in Fig. 1.2(a). The induced birefringence, δn, manifests as a retardation in the probe beam polarisation. This retardation may be detected by use of a post-sample analyser. Furthermore, the probe beam may be time-delayed with respect to the pump pulse, yielding a time-resolved excitation profile.

For materials with fast electronic processes, only when the probe beam is closely overlapped in time with the pump beam is the birefringence produced, and probe light exits the crossed polarisers. The signal (J/m^2) exiting the homodyne Kerr gate is given by [25]

$$S_t(\tau_D) = \varepsilon_0 c n_0 \int_{-\infty}^{\infty} \left\langle E^2_{probe}(t-\tau_D) \right\rangle \sin^2\left(\frac{\delta\phi(t)}{2}\right) dt , \tag{1.18}$$

where E_{probe} is the probe electric field, τ_D is the delay time between the probe and pump beams, and $\delta\phi(t)$ is the time dependent optically induced phase shift given by

$$\delta\phi(t) = \frac{2\pi l}{\lambda} \delta n(t) , \tag{1.19}$$

where, λ is the wavelength of light and l is the interaction (or sample) length. The birefringence, δn is given by

$$\delta n(t) = n_2^f \left\langle E_{pump}^2(t) \right\rangle + \sum_i \frac{n_{2i}^s}{\tau_i} \int_{-\infty}^{t} \left\langle E_{pump}^2(t') \right\rangle e^{-\left(\frac{(t-t')}{\tau_i}\right)} dt', \tag{1.20}$$

where n_2^f is the induced birefringence that arises due to fast responses, shorter than the pulse time; n_{2i}^s is the induced birefringence that arises due to "slow" response i, having a relaxation time of τ_i. The first term refers to the near-instantaneous electronic response (or all of the responses faster than the pump-probe autocorrelation time). The second term is a sum over all longer timed processes. Typically, the fast responses dominate for on-peak response($\tau_D=0$) and δn is approximated by

$$\delta n(t) = n_2 \left\langle E_{pump}^2(t) \right\rangle = n_2 \frac{1}{\varepsilon_0 c n_0} I_{pump} e^{-\left(\frac{t}{\tau_{pump}}\right)^2}, \tag{1.21}$$

where $\left\langle E_i^2(t) \right\rangle = \frac{1}{2}\left|E_i^2\right| e^{-\left(\frac{t}{\tau_i}\right)^2}$, and n_2 is the total optically induced birefringence. From Eq. 1.11:

$$\delta n(t) = n(t) - n_o = n_2 \left\langle E_{pump}^2(t) \right\rangle = n_2 I_{pump}, \tag{1.22}$$

where $n_2 = \varepsilon_0 c n_0 n_2$. The Kerr signal is now

$$S_t(\tau_D) = \int_{-\infty}^{\infty} I_{probe} e^{-\left(\frac{t-\tau_D}{\tau_{probe}}\right)^2} \sin^2\left(\frac{\pi d}{\lambda c \varepsilon_0 n_0} n_2 I_{pump} e^{-\left(\frac{t}{\tau_{pump}}\right)^2} \right) dt. \tag{1.23}$$

By making an important assumption that $\delta\phi(t)$ is small ($\delta\phi(t)<0.1$) we can use the $\sin(\delta\phi(t)) \approx \delta\phi(t)$ approximation. Thus the detected Kerr signal is

$$S_t(\tau_D) = \frac{\pi^2 l^2}{\lambda^2} \frac{1}{(c\varepsilon_0 n_0)^2} I_{probe} I_{pump}^2 n_2^2 \int_{-\infty}^{\infty} e^{-\left(\frac{t-\tau_D}{\tau_{probe}}\right)^2} e^{-2\left(\frac{t}{\tau_{pump}}\right)^2} dt . \tag{1.24}$$

Again, if we are only concerned with the peak value of $\chi^{(3)}$, then we may use

$$\begin{aligned} S_t(0) &= \frac{\pi^2 l^2}{\lambda^2} \frac{1}{(c\varepsilon_0 n_0)^2} I_{probe} I_{pump}^2 n_2^2 \int_{-\infty}^{\infty} e^{-\left(\frac{1}{\tau_{probe}^2} + \frac{2}{\tau_{pump}^2}\right) t^2} dt \\ &= \frac{\pi^2 l^2}{\lambda^2} \frac{1}{(c\varepsilon_0 n_0)^2} I_{probe} I_{pump}^2 n_2^2 \sqrt{\frac{\pi \tau_{probe}^2 \tau_{pump}^2}{\tau_{pump}^2 + 2\tau_{probe}^2}} \\ &\text{For} \quad \tau_{probe} = \tau_{pump} = \tau_{pulse} \\ &= \frac{\pi^{3/2} l^2}{\sqrt{3}\lambda^2} \frac{1}{(c\varepsilon_0 n_0)^2} I_{probe} I_{pump}^2 n_2^2 \tau_{pulse} \end{aligned} \tag{1.25}$$

and reconciling our definitions of δn from Eq. 1.22 as well as using our definition for $\chi^{(3)}$ from Eq. 1.11 we get

$$\begin{aligned} S_t(0) &= \frac{\pi^{3/2} l^2}{\sqrt{3}\lambda^2} \tau_{pulse} I_{probe} I^2{}_{pump} n'^2_2 \\ &= \frac{9\pi^2 l^2}{16\sqrt{3}\lambda^2} \frac{1}{(c\varepsilon_0)^2} \frac{1}{n_0^4} \tau_{pulse} (\chi^{(3)})^2 I_{probe} I^2{}_{pump} \end{aligned} \tag{1.26}$$

Since this detection scheme operates with crossed polarisers, the detected signal is proportional to the square of the pump intensity. As a drawback, this technique is unable to separate the real and imaginary components of $\chi^{(3)}$. Furthermore, because this detection scheme operates with fully crossed polarisers, minimal leakage through the polarisers and scattered light means that the signal obtained may be of the same order or smaller than the background noise.

In an attempt to separate the real and imaginary components of $\chi^{(3)}$ and to obtain signals much larger than the ambient scatter noise, another detection scheme, optical heterodyne detection optical Kerr effect (OHD-OKE)[17,26-28] is used by the vast majority of researchers. The OHD-OKE detection setup is shown in Fig. 1.2(b). In this scheme, a quarter-wave plate is placed between the probe polariser and sample such that the long axis of the quarter-wave plate is parallel to the polariser. By slightly rotating the polariser, $\pi/2$ out-of-phase light may be added to the probe beam, and the real part of the nonlinear response may be directly obtained from the Kerr signal. This scheme works in the regime where the crossed-polariser signal is linear with pump intensity.

We have introduced a new technique called differential optical Kerr effect (DOKE) detection, as discussed in the next chapter (§2).

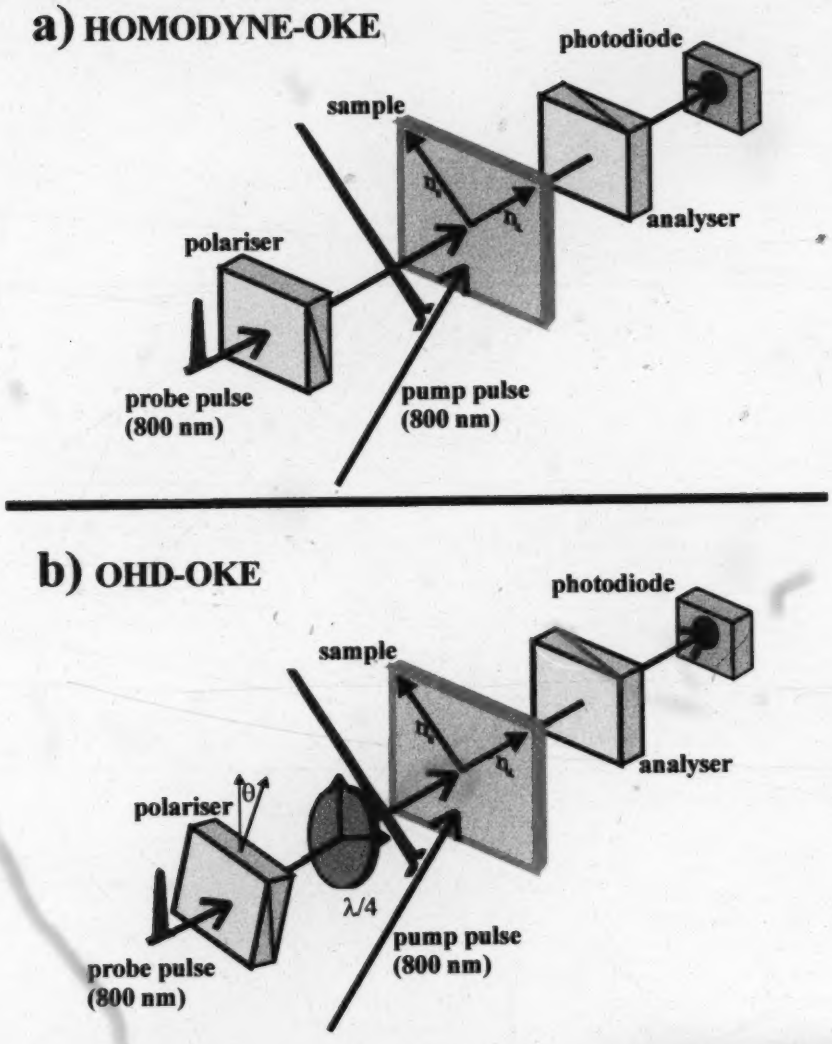

Figure 1.2: **Two Optical Kerr Effect Detection Techniques. (a) The standard Heterodyne detection layout, with fully crossed polarisers. The sample is pumped at 45 degrees to the analyser polarisation. A birefringence is induced in the sample between the dirctions parallel and perpendicular to the pump polarization. (b) The optically heterodyned detection arrangement. The polariser is rotated by a small (heterodyne) angle, θ, allowing some "local oscillator" light into the Kerr-gate. A quarter-wave plate is inserted in the probe beam, oriented with fast axis perpendicular to the analyser. The pumping and birefringence conditions are congruent to the homodyne setup.**

2 DIFFERENTIAL OPTICAL KERR EFFECT (DOKE)

2.1 DOKE LAYOUT

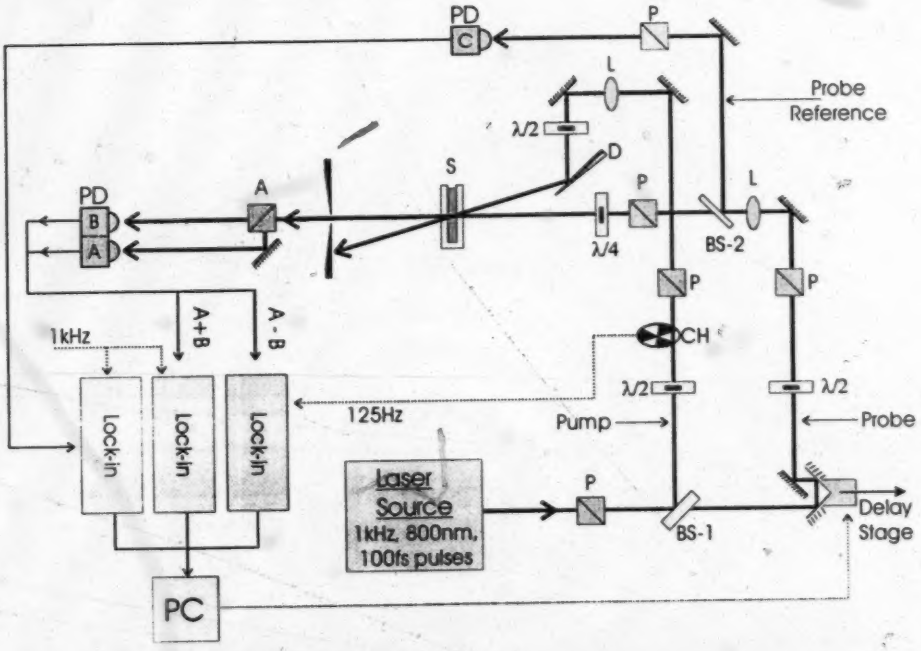

Figure 2.1: Schematic of the differential optical Kerr effect (DOKE) detection layout. PD-A: rejected probe beam photodiode detector; PD-B: transmitted probe beam photodiode detector; PD-C: probe reference photodiode detector; BS-1: beam splitter; BS-2: Brewster's Window as a beam splitter; λ/4: quarter-wave plate; λ/2: half-wave plate; D: D-mirror; P: Glan-laser polariser; A: Glan-laser polariser as an analyser; L: lens; S: sample cell; CH: chopper; PC: computer.

Figure 2.1 illustrates the main features of our DOKE gate layout. A Ti:sapphire laser amplifier generates 800 nm, 100 fs pulses at a repetition rate of 1 kHz. The beam is split in two for the pump and probe beams, with the beamsplitter providing a 20:1, pump:probe energy ratio. The probe pulse is time-delayed with respect to the pump pulse

by a computer controlled retro-reflector delay stage along the probe arm, with 0.7 fs step resolution. The pump pulse is chopped by a 50% duty cycle, 125 Hz chopper (CH). Using a half-wave plate, the pump pulse is polarised 45° to the horizontal and is focused onto a 1 mm path-length quartz cuvette that is filled with a sample solution (S). The pump beam is directed to the sample with the aid of a special mirror called a "D-mirror" (D). This is a semicircular mirror in a circular mount. Thus, the pump beam is reflected from an area near the flat edge of the mirror, while the probe beam can pass through the complimentary semicircular space between the mount and mirror. The D-shaped mirror allows the pump and probe beams to be nearly collinear.

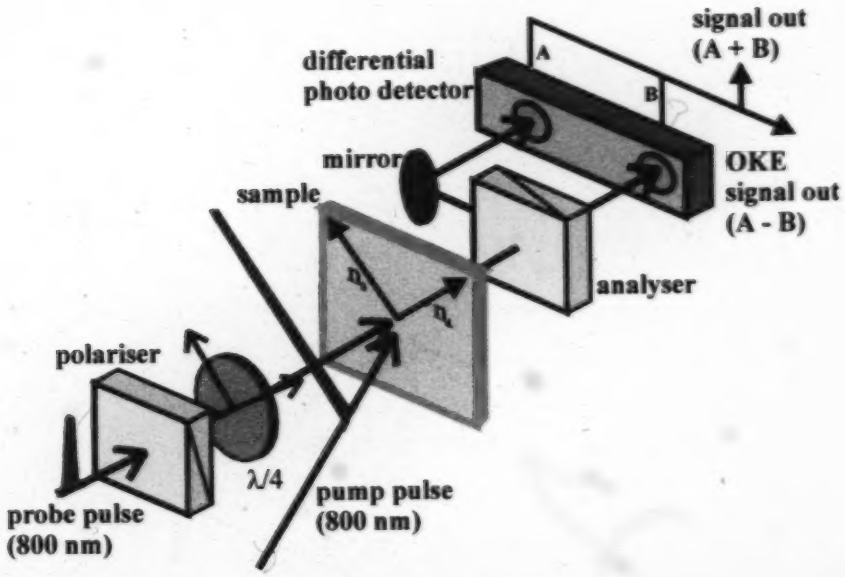

Figure 2.2: A close-up of the DOKE detection layout. The single photodiode detector of the homodyne and heterodyne detection schemes is replaced by differential detectors, analysing the full probe beam intensity. The quarter-wave plate is oriented to give circular probe polarisation at the sample.

A close-up of the DOKE detection arrangement in the vicinity of the sample is presented in Fig. 2.2. The much weaker probe beam is polarised vertically and then passes through a quarter-wave plate (λ/4) producing circular polarised probe light. The probe light is focused to overlap in the sample with the near-collinear pump beam (θ<5°).

The probe focus is tighter than that of the pump to ensure uniform pump intensity over the probe beam area. The pump beam is blocked after the sample, while the probe light is allowed to travel to a Glan-Laser polariser acting as the analyser. Here, the transmitted and rejected beams are separated and directed to balanced photodiodes (BPD). Photodiode "A" receives the rejected beam, and photodiode "B" receives the transmitted beam. The sum and difference ("A+B" and "A-B", respectively) of these signals are sent to separate lock-in amplifiers. The A-B signal is detected at 125 Hz, and A+B is detected at 1 kHz. Lock-in detection at the chopper frequency of 125 Hz presents some minor but important difficulties discussed in Appendix A. Finally, these signals are sent to a personal computer (PC) used for data acquisition and delay-stage control.

DOKE detection utilises both the quarter-wave plate and analyser differently than OHD. Furthermore, because signals are analysed from differential detectors, rather than a single photodiode, DOKE detection technique represents a significant modification to the OHD-OKE scheme. DOKE detection is quite similar to various optical biasing schemes routinely used in free-space electro-optic sampling of THz pulses [29,30].

A probe beam reference is present in our layout, providing an important diagnostic tool. A pellicle beamsplitter divides the probe beam at a ratio of approximately 20:1 allowing 95% of the probe intensity to continue to the sample. The other 5% is sent to a photodiode (PD-C) detector and then to a lock-in amplifier referenced to 1 kHz. Normally, the A+B signal acts as our main probe beam detector, because it provides us information regarding the post-sample probe intensity. However, the pre-sample probe detector aids in beam diagnostics, and provides information regarding pulse behaviour. Also, comparisons between A+B and our C detectors alert us to sample-related problems such as scatter and absorption. Although the probe reference signal was used for nearly all scans presented in this work, it does not contribute quantitatively to our analysis. The qualitative contributions of this important diagnostic tool, however, cannot be overstated.

A pump beam reference is also present in our layout, although it is not shown in Fig. 2.1. Because neither A nor B photodiodes detect the pump beam directly, a separate pump reference is needed. Ideally, the pump and probe beams should be coherently synchronised, allowing the probe reference to double as a pump reference. There is a

considerable difference in the two beam paths, however, each having a different array of optics to traverse. Thus, the probe beam uses a separate reference detector. As with the pre-sample probe reference, the pre-sample pump reference signals are not necessary for the quantitative analysis of most scans presented in this work. An exception to this is presented in the pump power-law test discussed in §3.2.1. Detection of the pump reference beam presents an interesting challenge, and the specifics of the pump reference layout are presented in Appendix B.

2.2 *DOKE Formulations*

The key features of the DOKE setup are that the A-B detection acts as our Kerr effect signal, while in the absence of nonlinear absorption and other $\mathrm{Im}(\chi^{(3)})$ processes, A+B acts as a probe beam reference. In the presence of nonlinear absorption (two-photon absorption [31,32], for example) the signal of A+B acts as an independent detection of the $\mathrm{Im}(\chi^{(3)})$ processes. The photodiodes are calibrated in such a way that in the absence of any birefringence, A and B signals are equal and A-B gives a zero background level. Regardless, it should be noted that instead of (A-B), Δ(A-B) at 125Hz is actually detected; this being the actual modulation of the pump beam intensity. Δ(A-B) also gives a zero baseline signal in the absence of birefringence.

Consider a vertically polarised probe beam and a sample with an induced birefringence of $\delta\phi = \phi' + i\phi''$, where ϕ' and ϕ'' are the real and imaginary components of the phase retardation, respectively. If after passing through a quarter-wave plate set with fast axis at 45°, the beam is incident on the sample, the detected signal ratio is given by

$$\frac{A-B}{A+B} = \frac{\sin\phi'}{\cosh\phi''} \tag{2.1}$$

This relationship is valid when the pump and probe beams are polarised 45° to each other. However, when the pump is polarised vertically (parallel to the pre-quarter-wave plate probe pulse polarisation) the detected signal ratio is

$$\frac{A-B}{A+B} = \tanh \phi'' ; \tag{2.2}$$

containing only imaginary components of $\chi^{(3)}$. Thus, by alternating between the two pump polarisation conditions, it is possible to obtain the separate ϕ' and ϕ'' terms, yielding the real and imaginary $\chi^{(3)}$ components. Clearly, in the absence of absorptive nonlinearities, $\phi'' = 0$, Eq. 2.2 gives a null signal and Eq. 2.1 is simply

$$\frac{A-B}{A+B} = \sin \phi' ; \tag{2.3}$$

a purely real response. The complete derivations of the preceding equations as well as analogous equations for OHD-OKE are given in Appendix C.

The preceding considerations account for nonlinear absorption. Linear probe absorption is independent of probe delay time, and should not lead to signal modulation at the pump frequency of 125 Hz. Linear absorption simply leads to an overall lowering of A+B signal. An excellent example of the effects of both linear and nonlinear absorption on DOKE signals is presented in Appendix D for a thin amorphous sample of arsenic-doped selenium.

Much like the heterodyne scheme, DOKE detection signals are linear with pump and probe intensity. However, because the DOKE technique probes the sample with circular light, it should afford a larger dynamic range of linear signal than the heterodyne scheme that probes the sample with light that is slightly elliptical. As an illustration of the fundamental differences between the three Kerr gate layouts, the descriptions of the signals transmitted through a polariser-analyser pair for small birefringences and various optical biasing conditions is useful. Figure 2.3 shows both the transmitted light intensity $(\sin^2(\phi))$ curve as a function of the un-crossing angle, ϕ, and the various positions along the curve at which three detection techniques operate. In standard homodyne detection, the square dependence of detected signal to pump intensity arises from detection with crossed polarisers. Here, no background light exits the analyser, and any small

birefringence allows for only small amounts of light to traverse the crossed polarisers. However, if the polarisers are slightly uncrossed, the shift up the $sin^2(\phi)$ curve may approach a linear regime. Heterodyne detection looks to tap into this linear regime by manually moving the system out of crossed-polarisation. The standard OHD-OKE technique, however uncrosses the polariser by only few degrees in order to approach the linear regime. Thus, the signals are linearly dependent on I_{pump}. The heart of the linear regime in the $sin^2(\phi)$ curve is at a 45°. The differential optical Kerr effect detection looks to reside here by probing with circular light, optically biasing the system to 45°. Thus it may be said that DOKE affords a larger linear dynamic range than OHD-OKE. The preceding discussion is given in an attempt to provide some physical, or intuitive, illustration of the differences in transmitted signals between the three detection techniques. For an exact graphical relationship between the homodyne, heterodyne and differential Kerr gate techniques, see Fig. C.1 in Appendix C.

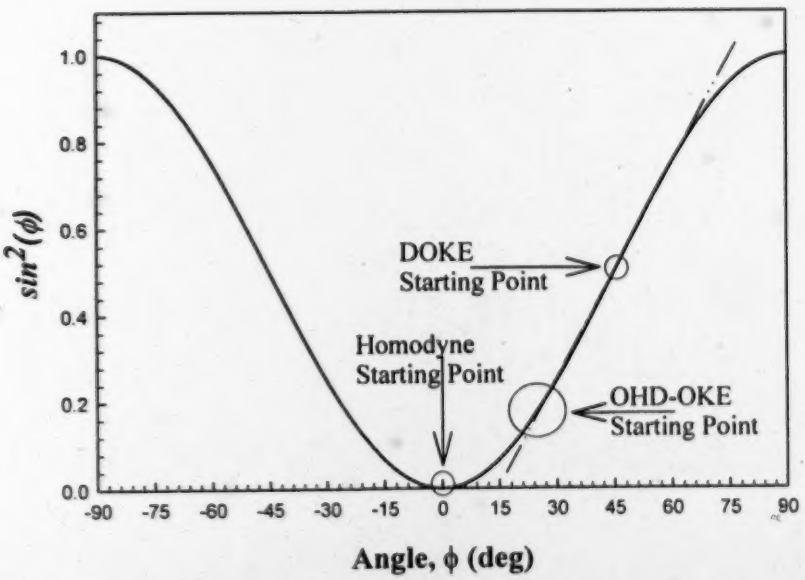

Figure 2.3: **The $sin^2(\phi)$ describing the transmitted light from a polariser-analyser pair, uncrossed by angle ϕ. The starting points for three detection techniques are shown, where an induced birefringence would represent a small movement along the curve, $\delta\phi$. The dashed line shows the linear regime.**

2.3 *DOKE Signal Detection*

The photodiodes are not ultrafast detectors. These silicon photodiodes have typical response times in the nanosecond regime which is much slower than the femtosecond-scale excitations we are studying. One of the benefits of pump-probe spectroscopy is that fast detectors are unnecessary. Each scan consists of hundreds of probe and pump pulses. For any particular delay-stage setting, a constant pump-probe delay time is present. Because the sample reaches equilibrium between consecutive pump pulses, we can remain at any time delay setting for as long as needed before moving to the next time setting. Over this time, the averaged photodiode signals are collected and they contribute to one data point corresponding to the particular time delay setting. Thus, although we detect the time-domain signal of the excitations, we do this with the aid of hundreds of thousands of pulses. This has the advantage of allowing as many scan averages as needed, reducing the ill-effects of laser intensity fluctuations. Averaging is done, to some extent, at the lock-in amplifier by selecting the detection time constant. Typically, this was set at 100 ms, which is equivalent to 100 probe pulses at the 1 kHz laser repetition rate. Furthermore signal-to-noise is further improved by averaging several complete scans. Thus, rather than averaging the data points as they are obtained, complete scans are averaged to yield a final Kerr signal of the sample. This method compensates best for systematic signal drift. Typically, between one and five scans were averaged to obtain the final signal profiles presented herein. A previously constructed set of balanced photodiodes was used as a template in constructing the balanced photodiode detector used for our DOKE detection. Appendix E shows the circuit schematics and initial diagnostics for this detector. Although the detector has two photodiodes, A and B, it also contains an adder so that it has three outputs in total; "A" output, "B" output, and "A+B" output. The "A+B" output is not equal quantitatively to "A" + "B". Therefore, the signals must be calibrated in such a way as to make "A" + "B" = "A+B" in order for our (A-B)/(A+B) analysis to work (see Appendix E). The A+B output is sent directly to a lock-in amplifier. To obtain the A-B signal, both A and B outputs are sent to a second lock-in that subtracts the signals directly using a differential amplifier.

2.3.1 *Finding The Zero Probe Delay time (τ_D=0) Stage Setting*

The first step to obtaining any Kerr signal is finding the exact stage position of maximum pump-probe temporal overlap, otherwise known as zero probe delay time, τ_D=0. Once this position is established, it should not change from day to day. However, any change in the experimental setup, such as laser alignment or sample position, affects the pump-probe overlap time. Kerr signals are often small and typically last for less than 1ps. Thus, there is a range of 0.3 mm over which signals may be observed. This makes locating the τ_D=0 position with an oscilloscope or with the lock-in amplifier difficult. A good procedure for finding the overlap time involves placing a thin (0.1mm) β-BBO crystal affixed to a rotating mount at the sample position. As the 800 nm pump and probe light pass through the crystal, they are frequency doubled to give two 400 nm beams. These beams are observed as two blue spots on a white card placed behind the crystal. The pump and probe beams are first overlapped spatially in the crystal, and the β-BBO is rotated to allow equal intensity of the two blue beams. When the two beams are temporally overlapped, a third 400 nm beam emerges at an angle bisecting the pump and probe beams [33]. This beam appears as a third, faint, spot between the pump and probe spots. In reality, as the stage sweeps past the τ_D=0 position, the middle beam lasts for only a fraction of a second, appearing as a short flicker of light between the two spots. If the card is placed far back enough, so that the two outer spots are separated by more than a centimetre, the flicker of the middle beam is more easily observed. At this point, the stage is moved back to find the position that gives the brightest middle spot. This position corresponds to maximum temporal overlap between the pump and probe beams. Replacing the BBO with the sample will then yield a Kerr signal on the oscilloscope or lock-in amplifier. Adjusting the pump beam with the "D-mirror" will yield the maximum spatial overlap of the pulses and thus the maximum on-peak Kerr signal.

3 PRELIMINARY WORK: DOKE SETUP CHARACTERISATION

The major goal of my research was to design and construct the first optical Kerr gate in our lab. Studying beam diagnostics and detector behaviours occupied much of the development time. In addition, becoming familiar with the intricacies of our particular Kerr gate occupied an extremely large portion of the research process. Verification of the correct beam intensity power laws and typical sample relaxation times as well as a slue of other characterisations had to be completed before we could confidently proceed with the testing of actual samples. Thus, this section provides a few examples of the many diagnostics that were necessary to complete before we could claim to have a properly working optical Kerr gate. Furthermore, I hope to give the reader some indication of the quality that can be expected of such diagnostics.

3.1 Beam Diagnostics

There are several laser and beam diagnostics relevant to optical Kerr spectroscopy that need to be discussed: First, autocorrelations at the sample location tell us about pulse duration. The pulse duration impacts the quality and shape of the Kerr signals. Furthermore, the exact pulse duration is needed for the measurement of absolute $\chi^{(3)}$ and γ values. Second, the probe and pump beam profiles at the sample location need to be examined since the spatial profile of the beam further impacts the quality of the Kerr signal. In addition, the beam waist is a necessary parameter in the calculation of exact $\chi^{(3)}$ values. Finally, general laser behaviour such as power- and pointing-drifts affect the intensity and quality of the Kerr signal. The first two diagnostics can help us improve our laser beam quality at the sample, while the last two diagnostics help identify the roots of certain detrimental features in our scans.

3.1.1 *Beam Autocorrelation*

The shape of time-resolved Kerr scans are determined both by scanning pulses' autocorrelation, and by long-relaxation-time effects. The latter are discussed elsewhere in this report (see for example, Appendix D). Nonlinear effects with near-instantaneous relaxation times follow the pulses' autocorrelation in a time-resolved Kerr signal [34]. In many samples, the nonlinearity arises solely from the electronic polarisabilities and the scan is an autocorrelation of the laser pulse, with the peak height providing all the necessary information about $\chi^{(3)}$. To resolve responses that are not instantaneous, the researcher needs short pulses with symmetric, Gaussian, time-profiles. Furthermore, in Eq. 1.26, I_{pump} and I_{probe} are measured in W/cm^2 and are obtained from the beam powers and spot sizes at the sample location. Thus, knowledge of the pulse duration is crucial. Laser pulses may be near-ideal at the source yet extremely degraded by the time they arrive at the sample. Prior to reaching the sample, the pulses travel through a jungle of optical elements, all of which degrade the beam to some extent. Cube polarisers, lenses, and wave-plates lead to dispersion in the beam and any dust on mirrors or any other optical elements further add considerable group velocity dispersions (GVD) that degrades the beam [35]. One method of obtaining near ideal pulses at the sample position is to provide negative chirp to the beam at the laser output [35-37]. Thus, as the beam propagates through dispersing elements, the negative chirp compensates for positive GVD and a near-ideal beam arrives at the sample. In our Ti:sapphire laser amplifier system, one of the last optical elements before the amplifier output is a beam compressor. The compressor setting determines the time-profile of the exiting pulses, and can be adjusted to provide chirps in the pulse.

Figure 3.1 shows the beam autocorrelation at the sample position, for various compressor settings. These autocorrelation scans were obtained by collecting the frequency-doubled light emitted from a 0.1 mm thick β-BBO crystal at the sample position [37-38]. The second harmonic light is then sent to a gallium phosphide photodiode detector.

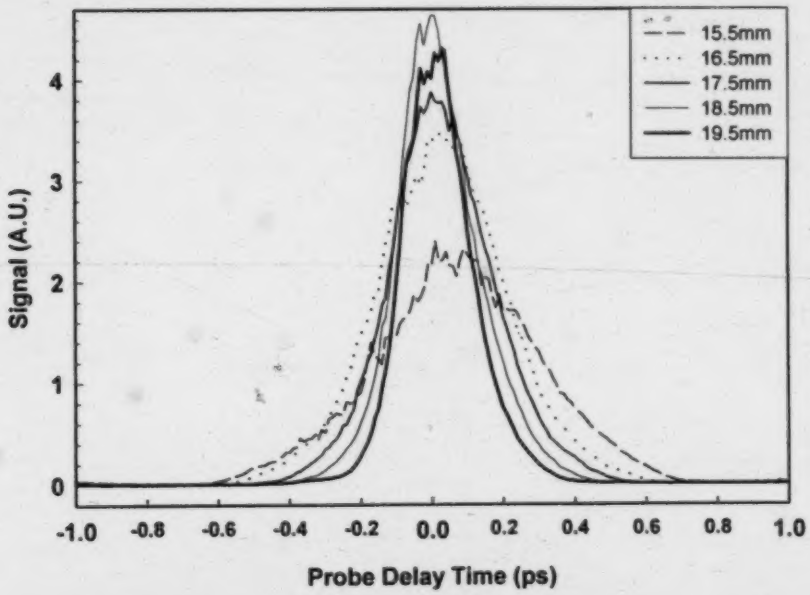

Figure 3.1: BBO second-harmonic autocorrelation signals at the sample location for various compressor settings. The shortest pulse is observed at a compressor setting of 19.5mm. The longest, most degraded, pulse is observed at 15.5mm.

In this pump-probe autocorrelation technique [39], varying the probe delay time with the computerised delay stage gives a time scan of the wave-mixing processes in the BBO crystal. When non-collinear pump and probe pulses are temporally overlapped in the crystal, the crystal emits a third frequency-doubled beam at an angle bisecting the two other beams, as described in §2.3.1. The time scan of this process gives the beam autocorrelation. Figure 3.1 shows that the pulse becomes wider in time as the compressor setting is moved from a setting of "19.5 mm" to a setting of "15.5 mm"; where the compressor setting positions are absolute, with reference to an arbitrary "0 mm" position. Typically, the pulse width is calculated as either $\sqrt{2} \times FWHM$ from a Gaussian beam or as $1.54 \times FWHM$ from a sech^2 shaped beam [40], where FWHM stands for Full-Width-at-Half-Max. Traditionally, the pulse width is calculated as for a sech^2 pulse regardless of the actual pulse shape. For a compressor setting of "19.5 mm" the pulse is its

narrowest, with a Full-Width-at-Half-Max of 215 fs and a $sech^2$ autocorrelation pulse width of 140 fs. The compressor setting that gives an ideal pulse at the laser output is "15.5 mm". However, a compressor setting of "15.5 mm" yields a pulse that continues to degrade, providing a pulse of width longer than 500 fs at the sample position. Thus, we found that providing a negative chirp in the pulse yields a better pulse at the sample position [35]. Determination of pulse quality at the laser output is best accomplished by taking an autocorrelation of the pulse at the output. However, the beam is extremely intense at the laser output, and thus, focusing the beam ionises the air and produces a "spark". Various nonlinear processes occur in the vicinity of the spark such that adjusting the compressor until best continuum generation is observed (rainbow) is sufficinet indication of pulse quality. A poor quality pulse has sufficient energy to ionise the air, but the pulse duration is too long to generate more than second harmonic light, and the resulting light is a mixture of first and second harmonic light (800 nm red and 400 nm blue).

As previously mentioned, the time-resolved OKE signal can provide a near perfect autocorrelation when the sample response is purely electronic –and therefore considered to be instantaneous. This allows the use of the Kerr gate setup for an in-situ autocorrelation. Figure 3.2 shows some recent Kerr signals of tetrahydrofuran (THF) at various compressor settings. Clearly, these peaks are not as symmetric as the BBO autocorrelation profiles of Fig. 3.1. THF has a small, non-instantaneous component to its third-order nonlinear response. As a result, the scans are nearly symmetric autocorrelations, but contain a slight, visible post-peak component. Since this longer relaxation-time component is so small, the signal FWHM is still a good in-situ pulse-width indicator. Before the scans, the laser output was checked and the best pulse was generated when the compressor setting was "14 mm". However, at the sample location, the best pulse is obtained with a compressor setting of 18.5 mm. Again, this shows the need for introducing a considerable negative chirp to the output pulses. The advantage to in-situ autocorrelations is that they can be obtained without modification to the Kerr Gate. In many cases, the same scans obtained for our primary research on novel and interesting samples may be used as autocorrelations –or at the very least– indications of the pulse duration for the experiment. The in-situ technique is even more useful when

using a perfectly symmetric sample such as CCl_4. Such samples provide more symmetric scan profiles because they only have electronic nonlinearities. CCl_4 scans are discussed further in Appendix D.

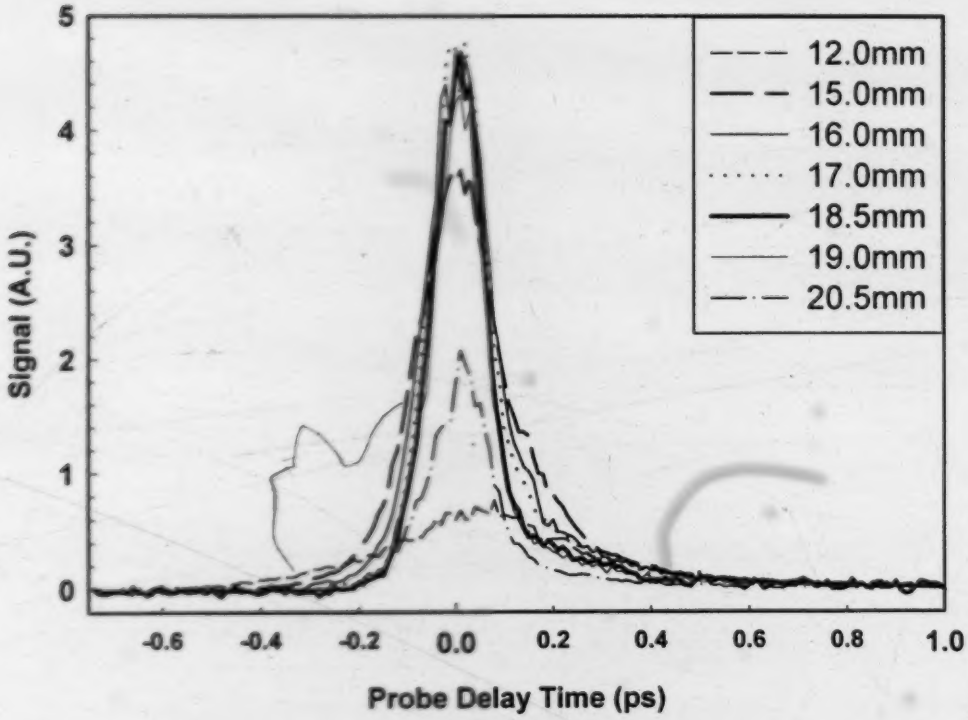

Figure 3.2: **THF Kerr signals for different compressor settings: Note that the signals are not entirely symmetric. However, the asymmetries are very small and the FWHM is a good representation of the pulse duration providing an in situ autocorrelation method.**

3.1.2 *Spatial Beam Profiles*

The spatial beam profile describes the intensity profile of the beam's cross-section. Ideally, this is a two-dimensional profile, however for most purposes, a beam cross section along one transverse axis is sufficient. A Gaussian time pulse should have a Gaussian spatial profile. However, any degradation or dispersion in the beam will lead to non-transform-limited pulses and a less-than-ideal beam profile, particularly at the outer wings. Because the beam is focused at the sample, the spatial profile shape is not crucial, however, it should be roughly symmetric with a flat or rounded peak.

The beam profile is mainly needed for intensity calculations. When calculating the pump and probe intensities for Eq. 1.26, an assumption is made that the pulses have square-pulse intensity profiles. This assumption simplifies the Kerr signal analysis considerably [25]. Although we use the square-pulse approximation in our calculations, the spatial profile is necessary for obtaining the spot size at the sample location. Being spatially unbound, the Gaussian beam has no naturally indicated definition of spot width. Traditionally, the beam diameter is measured as the full width between the $1/e^2 = 0.135$ points of the peak intensity [41]. Figure 3.3 shows the pump and probe beam spatial profiles at the sample. Taking the pump beam profile as an example, Fig. 3.3(b) shows a pump peak intensity of 3000 A.U. Thus, the radius may be interpolated from an intensity of

$$\frac{1}{e^2}(3000 A.U.) = 400 A.U. \tag{3.1}$$

The diameter at 400 A.U. is 0.490 mm or 490 μm. Thus, the pump beam spot size is 490 μm. Likewise, the probe beam diameter is 235 μm, as can be seen from Fig. 3.3(a).

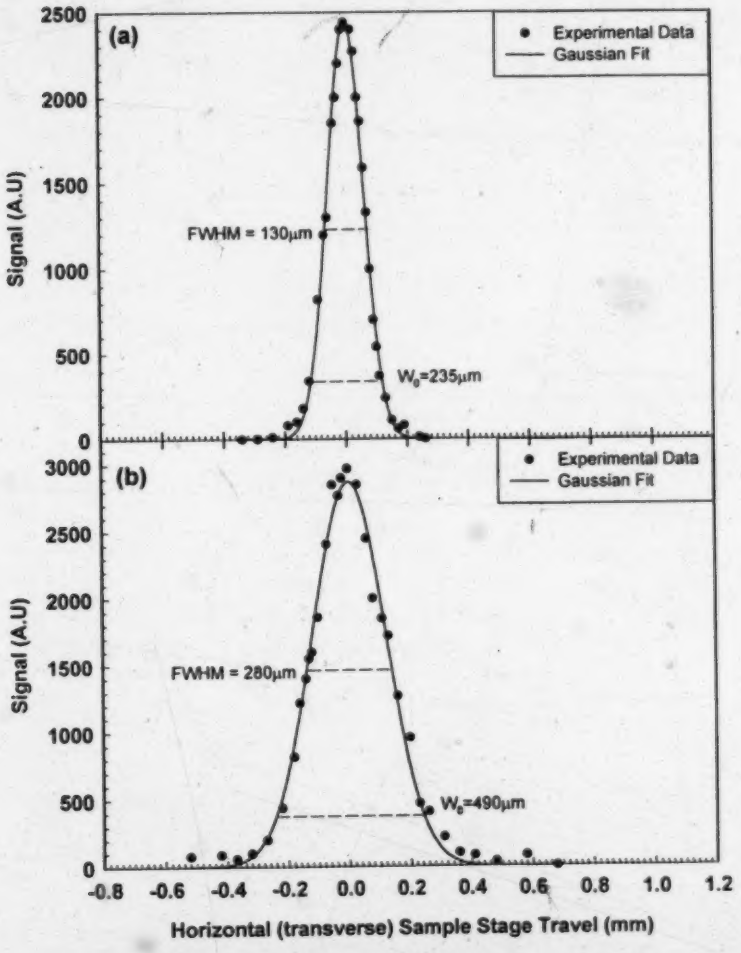

Figure 3.3: Pump and probe spatial beam profiles. (a) Spatial profile of the probe beam, showing a spot size of 235 μm and (b) spatial profile of the pump beam, showing a spot size of 490 μm. Solid lines are Gaussian fits, showing near-ideal spatial profiles.

The preceding scans were obtained as illustrated in Fig. 3.4. The sample holder, already on a z-x horizontal stage, is replaced by a mount composed of a 25 μm pinhole masking a small photodiode detector. The detector is 1 cm behind the pinhole. The detector signal is then relayed to an oscilloscope. This mount is on an x-y stage, allowing small adjustments in the vertical plane. The pinhole is placed at the pump-probe overlap area at the typical sample location. The pinhole/detector mount is moved to an initial

position that gives the greatest thorough-signal. The signal intensity is obtained and recorded from the oscilloscope. The pinhole/detector is then moved transversely along the x direction across the beam. Intensities are recorded at various x positions yielding a one-dimensional beam profile. As a check, the pinhole is returned to the initial position and then the beam's cross section is scanned along the y-direction, confirming that the FWHM intensity is at roughly the same radius as in the horizontal axis. In the case of Fig. 3.4, the beam diameter along the y-direction was equal to that of the x-direction suggesting the beam is circular in cross section.

3.1.3 Laser Power and Alignment Drifts

A steady laser source is always desirable whenever laser light is used as a spectroscopic tool. Minimal pulse-to-pulse intensity fluctuations are particularly important for the detection of optical Kerr effect signals [3]. However, all pulsed laser systems experience pulse-to-pulse fluctuations and laser intensity drift. The direct effect of laser power drift (if to lower power) is a lowering of the Kerr signal. Thus, with large laser drift, or pulse-to-pulse fluctuations, it is increasingly difficult to obtain precise and reproducible results. Monotonic drifts in laser power often mean that, as the day progresses, the power slowly drifts to lower powers. Often, the total drift is 10% over a period of a few hours, but it can be as large as 30% an hour. A slow laser power drift is not as detrimental to the scans as the rapid pulse-to-pulse fluctuations because of reference beam normalisations. Furthermore, the slow power drifts can be seen from scan to scan as a lowering of both the peak Kerr signal intensity and the overall reference signals.

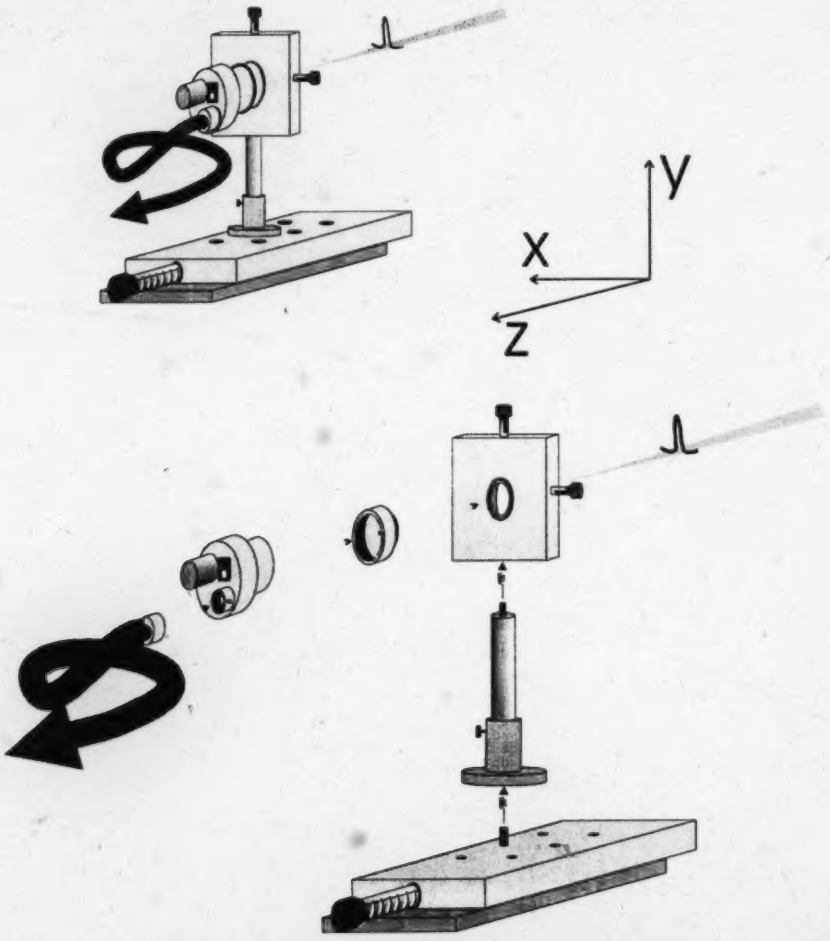

Figure 3.4: Drawing of spatial profile detection equipment: The photodiode detector is behind a 25 μm pinhole that is attached to a x-y adjustable mount. The entire setup is on a variable z stage, giving 3-dimensional mobility. The beam is scanned along the x-direction, yielding the beam's spatial, cross-sectional, profile.

A more subtle problem is drift in laser pointing. Since the laser path can be as large as 6 m from source to sample, a shift of 0.002° at the source will lead to a transverse displacement, of 200 μm at the sample; more than enough to separate the once-overlapped pump and probe beams. Drifts in laser pointing have the effect of decreasing the detected signal by providing poor pump-probe overlap and an incomplete sampling of the sample birefringence. Also, a transverse drift in the pulse wavefront leads

to shifts in arrival times; in effect, the pulse travels a little further to get to the sample, and the overlap time is slightly modified. It is this change in the pulse timing that allows us to distinguish between intensity and pointing fluctuations.

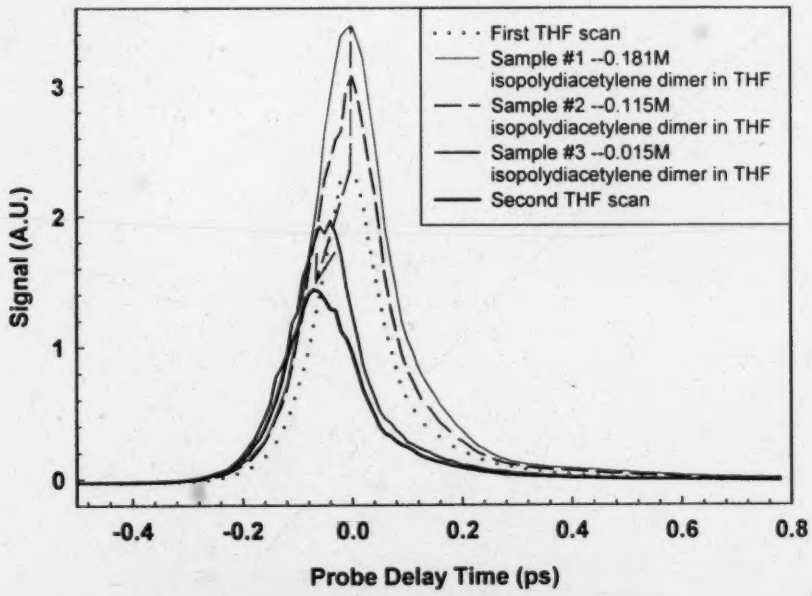

Figure 3.5: Kerr Signals for a scan series showing the effects of drift in laser pointing. The composition but not the concentrations of samples #1-3 should be ignored. The arrow illustrates how both a lowering and time-shifting of the signal is observed.

Figure 3.5 shows a scan sequence in which pointing drift is present. The figure contains five Kerr signals. The three sample signals are expected to decrease in order, as they are composed of decreasing sample concentrations in THF. The THF peaks were obtained from the reference sample and should, ideally, overlap. These signals were obtained by normalising the original Kerr responses to the laser power reference. Thus, the lowering in peak values from one THF scan to the next is not attributable to drifts in laser intensity. One possible explanation is that the pump and probe beams became less overlapped resulting in the induced birefringence of the sample being only partially scanned. This conclusion is further substantiated by the observable time-shifts in the signal peaks. Beginning with the first THF scan it is clear that the τ_D=0 condition is

shifting to earlier times. These two scans were taken 90 minutes apart [42]. An overall shift of 70 fs is present between the two THF peaks. A 70 fs shift corresponds to a longitudinal beam displacement of 21 μm. This is a very small shift, and with the collimating and focusing present in beam path, it is not unreasonable to imagine that the pump-probe overlap might be only slightly affected, giving a lowered Kerr Signal. Thus, the observation of both a scan-to-scan τ_D=0 shift and a scan-to-scan lowering of the peak intensity may be indicative of drifts in laser pointing rather than pulse-to-pulse fluctuations. Of course, the presence of peak intensity drifts without overlap time shifts is a clear indication of an unstable laser source.

3.2 *Optical Kerr Gate: Characterisation*

Before a new Kerr gate can be used to generate publishable data, there are several tests that must be conducted. In this work I can not hope to present all of the diagnostic tests that were conducted throughout the various phases of this research. However, some of these tests are fundamental to the workings of our particular Kerr gate and require mentioning. First, obtaining the proper power laws describing the detected signal dependence on the pump and probe intensities is crucial for showing that the DOKE detection works as we predict in §2.2. Another test that helps to substantiate theories laid out in §2.2 involves showing DOKE signals for four polarisation cases: when the pump beam excites the sample i) at 45° to the analyser, ii) parallel to the analyser, iii) at -45° to the analyser and iv) perpendicular to the analyser.

3.2.1 *Power Laws*

One of the fundamental aspects of both the OHD-OKE and DOKE detection techniques is that they are designed to work with a linear dependence between signal and pump intensity. This contrasts with the homodyne detection layout that obtains signals that are a function of I^2_{pump}. All three techniques count on linear probe power

dependence. Thus, it is necessary to show that the Kerr signals obey these power laws before any data derived from our DOKE system may be presented.

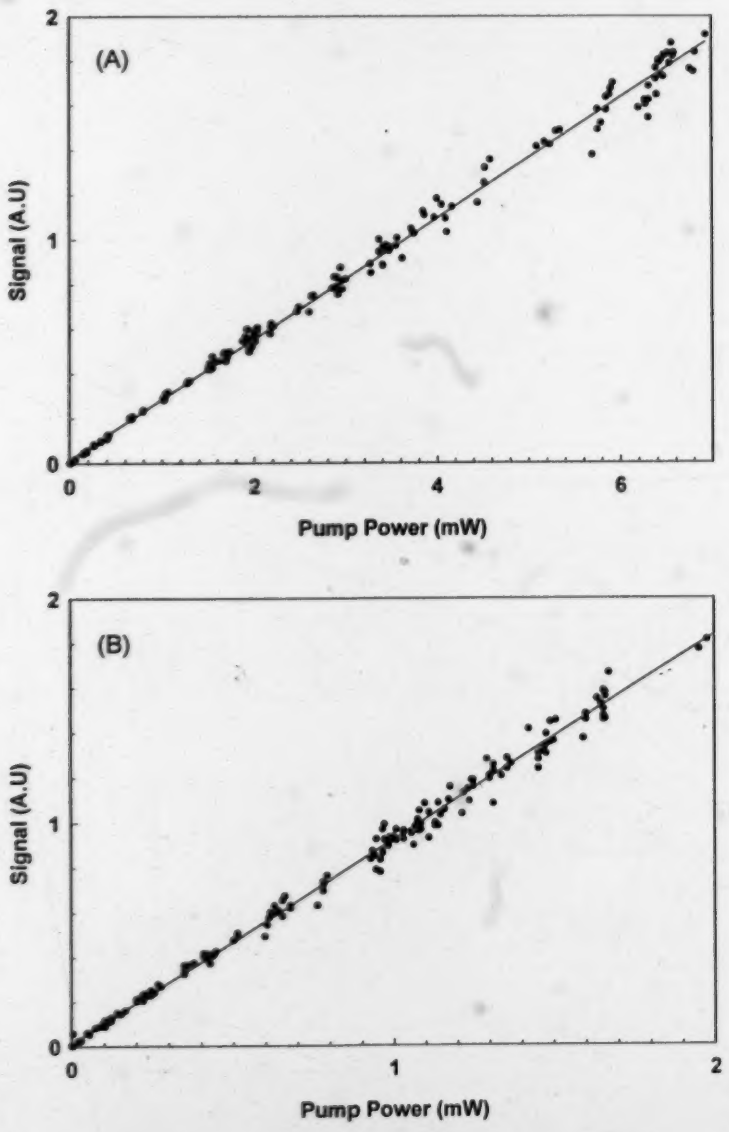

Figure 3.6: **Dependence of DOKE signal on pump beam powers for (a) a dilute iso-polydiacetylene dimer sample in THF and (b) a CS_2 reference sample. Nonlinearities are kept below $\sin\phi < 0.2$. Lines are regression fits, showing good linear behaviour.**

Figure 3.6 shows pump power laws on two different samples; an iso-polydiacetylene compound and a CS_2 standard. For the iso-polydiacetylene dimer, the typical pump powers used are 0.5-6 mW. For CS_2, the typical pump powers used are 0.3-0.8 mW. Thus, our experiments are in the linear regime. Clearly, up to an "A-B" signal modulation of 20% ($sin^2\phi < 0.2$) we have linear dependence between the Kerr signal and pump intensity. This is a very large linearity range. Despite the fact that Fig. 3.6 shows great signal linearity, it is essential to expand the pump powers in the test to see where the linear behaviour breaks down. Figure 3.7 shows DOKE signals as a function of pump beam power for THF, our typical reference sample. This pump power range far exceeds the typical powers used in our DOKE experiments. The linear range is seen to extend from zero signal up to about 10 mW. After this range, the signal behaves in a complicated manner: The $\sin\phi \approx \phi$ approximation is no longer valid; a very large birefringence moves us away from n=1 in the $\sin^n\phi$ dependence of the signal and towards more complex signal behaviour. In addition, signal saturation and dispersion effects arise. We typically use pump powers of 3 mW-4 mW, and rarely do we use powers outside the 2-6 mW range for THF and THF solutions. These pump powers lie well within the linear regime.

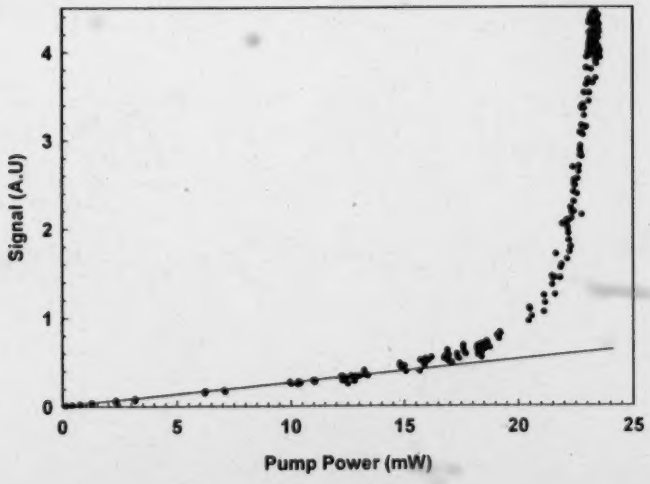

Figure 3.7: Dependence of DOKE signal on pump beam power for a THF standard. The solid line is a guide to the eye showing good signal linearity to well above 10 mW.

The Kerr signal is expected to be linear in probe intensity for all three detection setups. Figure 3.8 shows the probe beam power law for an iso-polydiacetylene dimer sample. This figure shows good linearity between the Kerr signal and probe beam intensity, in the low probe intensity region. Theoretically, there is no range of probe intensity for which a deviation from linearity is expected. However, since with DOKE detection there is always a photodiode that detects at least half of the complete probe intensity, detector saturation effects make it practical to only work with low probe powers. The typical probe power used for all of our Kerr experiments, regardless of sample, is roughly 50μW. Because it is detected directly, probe beam scatter is ever prominent, and the Kerr signals show increased noise. Nonetheless, the probe power ranges typically used in our experiments show great signal linearity.

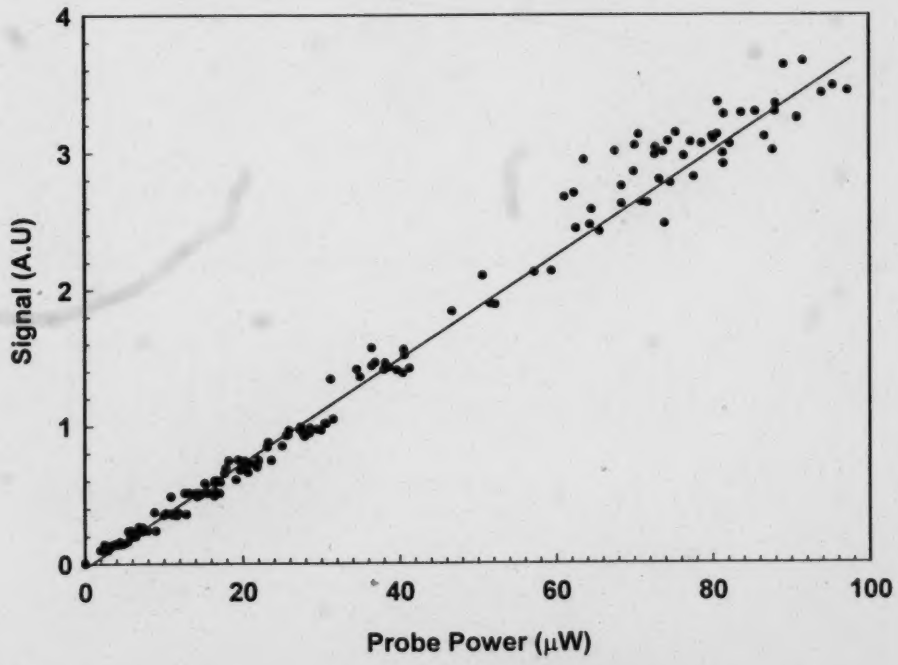

Figure 3.8: Dependence of DOKE signal on probe beam power for a dilute iso-polydiacetylene dimer sample in THF. Nonlinearities are kept below $\sin\phi < 0.1$. The solid line is a regression fit, showing good linear behaviour.

3.2.2 *DOKE Polarisation Conditions*

DOKE detection is heralded by the simplicity of its signal analysis. The most important aspects that must be confirmed in the DOKE layout are the equations presented in Appendix C. We can show that the equations are consistent with our data, but to verify the actual values that the equations and experiments yield is quite challenging. The standard way to do this is by comparing the new detection layout (DOKE) with another, established, scheme such as OHD-OKE or homodyne detection. In the absence of another working layout scheme in the lab, verifying ours in this way is not possible. However, we continue adding to the circumstantial evidence in an effort to prove that the DOKE system behaves as we predict. With that in mind, another aspect of the DOKE equations is examined in this section.

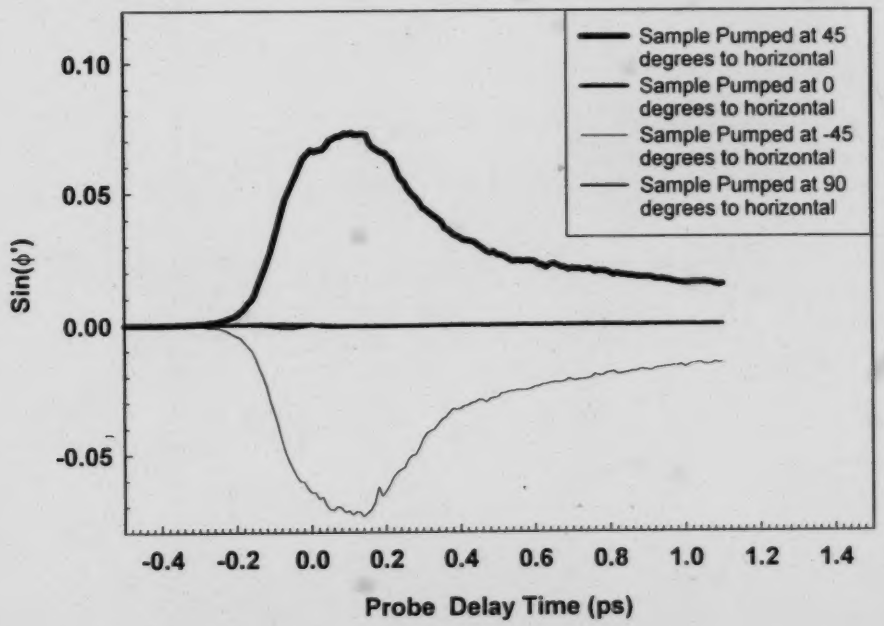

Figure 3.9: **CS_2 Kerr signals for the four DOKE polarisation conditions. This is an example of a sample with no $Im(\chi^{(3)})$ component.**

As discussed in Appendix C, there are essentially four useful pump polarisation conditions. When the sample is pumped either along, or orthogonal to the probe polariser setting we obtain an $(I_x-I_y)/(I_x+I_y)$ signal that is purely imaginary, and in the absence of nonlinear absorptive terms, the signal is zero. On the other hand, when the sample is pumped at either 45° or -45° to the polariser setting we obtain $(I_x-I_y)/(I_x+I_y)$ signals of $(\sin\phi')/(\cosh\phi'')$ and $(-\sin\phi')/(\cosh\phi'')$ respectively. Figure 3.9 shows CS_2 DOKE scans obtained at all four polarisation conditions. Because CS_2 has only real $\chi^{(3)}$ terms in the wavelengths used in our experiments, [43] we expect Eq. 2.2 to yield null signals. This figure clearly shows that the two polarisation conditions that are expected to yield negative or zero signals comply with predictions. Any changes from ideal, identical, signal shapes can be safely attributed to noise and slight misalignment issues with the non-ideal polarisers present in our setup. The mirroring of CS_2 DOKE signals offers further indication of the consistency of the DOKE detection technique.

4 EXPERIMENTAL

4.1 Sample Preparation

Most samples investigated by the optical Kerr effect are liquids and solutions. Exceptions include scans on thin fused-silica, fused-quartz and other glass samples traditionally used as reference standards for $\chi^{(3)}$ [14]. Liquid samples are typically held in high-quality quartz cuvettes, commonly used for infra-red spectroscopy, owing to their negligible absorption, manufacturing uniformity and ease of cleaning. The cuvettes used in our experiments are 3.0 mm thick. They consist of two 1.0 mm thick quartz walls and a 1.0 mm optical-path-length open-top sample chamber. The total sample volume held by the cuvette is approximately 0.40 ml.

Pure liquid samples such as CS_2, CCl_4 and THF are used as purchased. All cuvettes are cleaned with tetrahydrofuran (THF) and rinsed with spectroscopy-grade methanol. Finally, after drying, the outer cell walls are gently cleaned with methanol and lens paper.

Oligomer samples are prepared by weighing the samples into small sample containers and then diluting with THF. A 1.0 ml syringe equipped with a 0.22 μm Osmonics™ filter is used to transfer liquids into the cuvette. The filter prevents dust from entering the sample cell. Any dust in the cuvette will lead to scatter noise. Furthermore, we have observed that dust particles seem to aggregate at the pump beam-sample interface. Occasionally, when high accuracy of solvent volume delivery is essential, a volumetric pipette is used to measure and deliver THF to the sample containers.

Sample cuvettes are fitted with custom made teflon lids. These lids are not air-tight and allow slow evaporation of the samples. Pure THF in a lidded cuvette will evaporate to about half volume in 24 hours. Typically, sample solutions evaporate more slowly than pure liquids, as oligomer sample condensate seals the edges of the cuvette lids and prevents further evaporation. Due to fears of sample degradation and slight changes in concentration, once a sample is prepared, it is normally tested within 36 hours.

4.1.1 Cross-conjugated iso-polydiacetylene oligomer series

In this work the first OKE measurements on a novel cross-conjugated oligomer series are presented. For this project, we have synthesised the *iso*-polydiacetylene (*iso*-PDA) oligomers shown in Fig. 4.1. The phenylated *iso*-PDA oligomers were synthesised stepwise using a procedure analogous to that published for alkyl substituted derivatives [44]. All oligomers have been fully characterised by ^{13}C and ^{1}H NMR, IR and UV-Vis spectroscopies, and high-resolution mass spectroscopy (HMRS). These compounds are stable under ambient conditions and require no special handling precautions. Full synthetic details will be published elsewhere. Samples were prepared by dissolving solid oligomer samples in high-purity tetrahydrofuran (THF) to give solutions of 0.1M-0.23M. Typically, solutions were made to 0.6 ml as the quartz cuvette is able to hold 0.4 ml of solution. Sample nonlinearities and UV-Vis absorbance were measured within 36 hours of sample preparation. The sample nonlinearities were probed at 800 nm, far off resonance, as may be seen in Fig. 4.2.

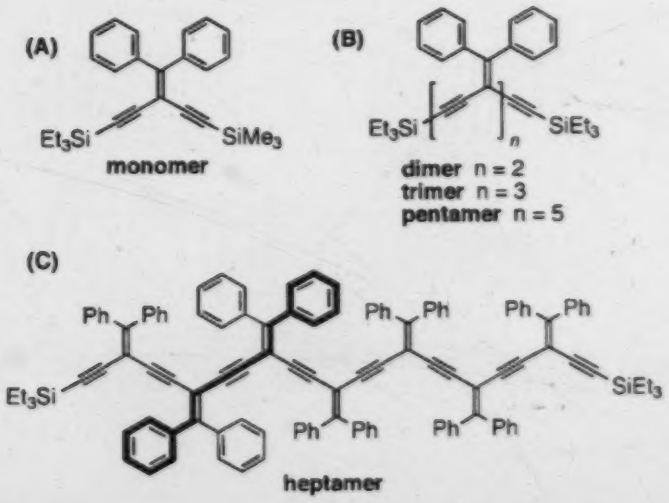

Figure 4.1: Chemical structure of the *iso*-polydiacetylene oligomers showing (a) the monomer, (b) the repeat unit, and (c) the heptamer sample. The longest linearly-conjugated segment present in the n ≥ 2 molecules is shown as a thick line in the heptamer structure.

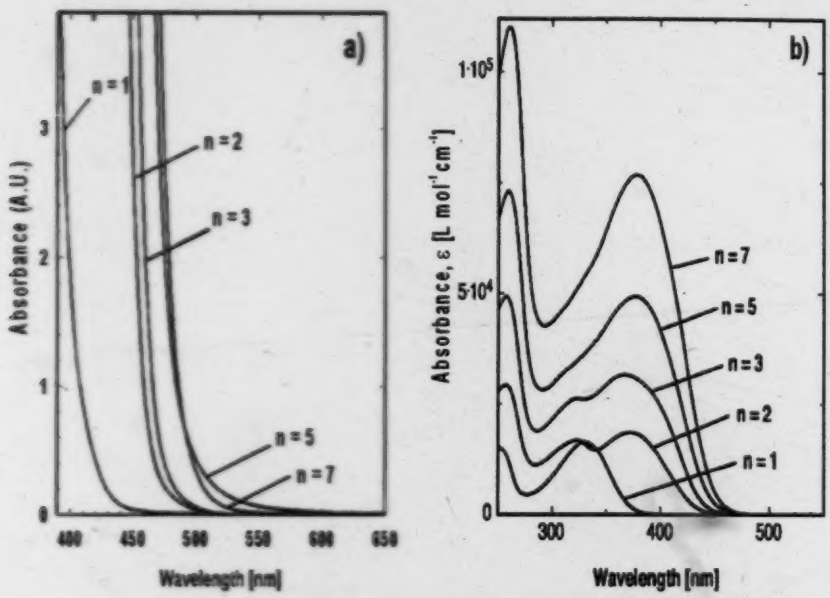

Figure 4.2: **(a) UV-Vis absorption spectra of the oligomer samples at the concentrations used for the OKE studies. The scale shows that the absorption edge, λ_0 has nearly saturated by the heptamer (n = 7) sample. (b) The full absorption spectrum for the oligomer samples. n is the number of repeat units in the sample. The lowest energy wavelength of maximum absorption, λ_{max}, does not appreciably shift from the dimer to the heptamer.**

4.2 Concentration Tests

Whereas $\chi^{(3)}$ is a property of a bulk sample, γ is a molecular coefficient. Thus, DOKE scans on a given sample in solution yield properties of the solution itself and not of the individual components. However $\chi^{(3)}$ can be converted to γ_{sample} by knowing the solution concentration and $\chi^{(3)}_{solvent}$ as was discussed in §1.2.2. The relationship between the nonlinear susceptibility and the hyperpolarisability is given by

$$\chi^{(3)} = L^4\left[N_{c\,(solute)}\langle\gamma_{solute}\rangle\right] + \chi^{(3)}_{solvent}, \qquad (1.17)$$

where $\chi^{(3)}$ is the measured quantity, $\chi^{(3)}_{solvent}$ is either measured or assumed from an acceptable literature value, and N_c is determined during sample preparation. Ideally, a single value of N_c is sufficient for the determination of γ.

There are several factors that may contribute to deviations from Eq. 1.17. First, when dealing with small sample volumes, exact concentrations are difficult to estimate. Thus, using a single value for the sample number density can lead to large uncertainty in γ. Second, the assumption that the solvent and solute are non-interacting is implicit in Eq. 1.17. If the sample number density is large enough, or if the sample and solvent are chemically active, there may be solvent-solute interactions. To account for these factors, many researchers prepare several solutions of varying concentrations. Then, a plot of $\chi^{(3)}$ as a function of N_c should be linear, yielding γ from the slope. This method also shows whether the concentration ranges used are low enough as to be in the non-interacting regime. Furthermore, small errors in concentration will not overly affect the results.

Despite the benefits of the method describe above, obtaining $\chi^{(3)}$ at various concentrations is not strictly necessary. If one is particularly careful in determining the sample concentration, and has further shown that the signals are linear with concentration, a fixed concentration $\chi^{(3)}$ scan should be sufficient to obtain γ.

In our case, the samples are difficult to synthesise. Total samples obtained may be less than 80 mg. Diluting such a small sample into various concentrations is prone to more error than is found in the fixed concentration method. Furthermore, solutions should be made to give several concentrations that are separated enough to provide a plot with adequate resolution. This entails even more difficulties in such small samples. For instance, a 65 mg dimer sample diluted to 0.6 ml with THF has a concentration of 0.164 M. To obtain precise, repeatable results, 0.4 ml of solution is needed in the cuvette. Due to sample loss and difficulties inherit to transferring sub-millilitre volumes, the next diluted concentration may be expected to be two-thirds of the first, and so on; each step introducing larger uncertainties and smaller concentrations. By about the fourth dilution, the concentration is below the signal resolution. Better analytical technique and equipment as well as an increase in sample availability should provide considerable improvements to the dilution procedure. Perhaps at that time, a concentration dependence of $\chi^{(3)}$ will be obtainable for every sample.

Since we are not able to obtain the concentration dependence of $\chi^{(3)}$ for each compound, we are forced to use the fixed concentration method. Despite the difficulties in preparing different sample concentrations, it is important to present at least one concentration test. The results of such a concentration test, conducted on the dimer sample, are presented in Fig. 4.3. An obvious concern with our concentration test is that it only contains two concentration data points and a blank. Initially, four samples were made, two of which, as a result of preparation difficulties, were found to be inadequate for analysis. However, the three data points in Fig. 4.3 are sufficient to show superb linearity down to zero concentration. This concentration test verifies that there is no interaction between the oligomer and THF molecules at these concentrations. Furthermore, it verifies Eq. 1.17 and simplifies the analysis considerably. This is particularly true since the scan values given are actually $\chi^{(3)}_{Dimer+THF+cuvette}$. Thus, we may separate $\chi^{(3)}_{Dimer+THF+cuvette}$ into $\chi^{(3)}_{Dimer} + \chi^{(3)}_{THF+cuvette}$. Further discussion on the effect of the sample cuvette may be found in the next section.

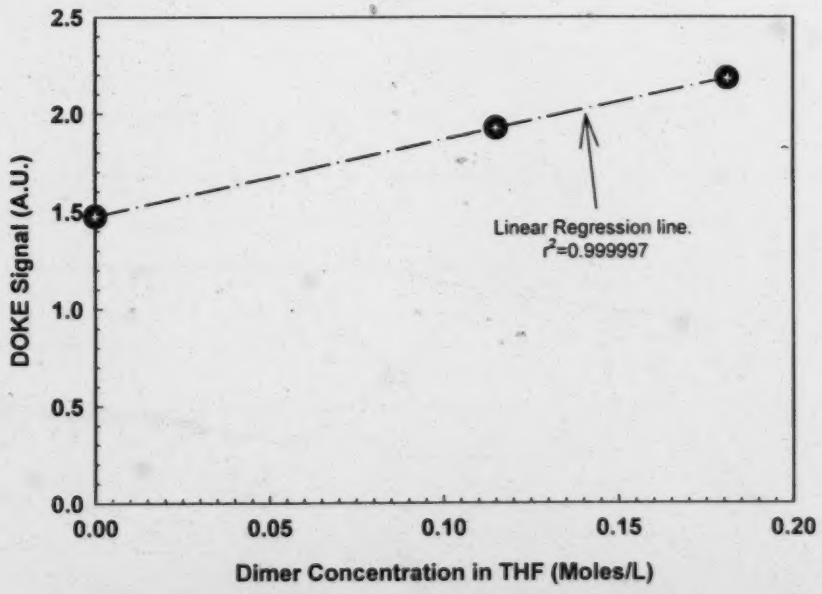

Figure 4.3: Concentration test for an iso-polydiacetylene dimer. A concentration of 0M represents a pure THF blank. Dashed line is a linear fit showing excellent linearity in this concentration range.

4.3 *Cuvette Effects and Blank Measurements*

Defining an experimental "control" or "blank" is a crucial step in any scientific investigation. For many systems, a blank is simply a null result, or the absence of a sample. Our DOKE setup offers some complications with finding a proper control. The presence of a reference, which is used to calibrate all Kerr measurements that yield nonlinear coefficients, should not be confused with a blank. Specifically, there are four conditions to consider: The first is a "true blank", or null experiment, in which no sample or sample holder is placed at the pump-probe intersection. This condition represents a background scan yielding a kerr measurement of the ambient air in the lab, utilising the full measure of pump-probe interaction length. Second, is a measurement of an empty, un-evacuated quartz cuvette. This procedure represents a classical blank experiment in which the sample holder alone is scanned. Third, the sample holder filled with THF or some other reference material is scanned. The results of this experiment are our "reference" signals. Finally, there are the "sample" scans. These scans represent the signal of the sample holder, the THF solvent matrix, and the dissolved sample molecules.

The "true blank" measurements indeed yield a null measurement and may be ignored for all future experiments; unless the pump beam intensity is significantly increased, at which time the ambient lab atmosphere may contribute to the nonlinear signal. However, the empty sample holder does not yield a similar null result. In fact, the quartz cuvette yields a signal of significant contribution to the reference scans. Hence, the reference measurements do not represent a "control", but are used for calibration and normalisation purposes only. As a matter of clarity, this work refers to measurements of THF in the sample holder as reference measurements, and $\chi^{(3)}_R$ reflects the combination of the two signals. The pure signal for THF, after it is separated from the reference measurements, yields $\chi^{(3)}_{THF}$ and γ_{THF}. However, aside from the distinct definition of their respective nonlinearities, both are interchangeably referred to as reference signals.

Despite the preceding discussion, separating contributions from reference and sample signals is not that difficult. Careful attention must be taken, however, to the reporting of nonlinear values. The third-order nonlinearity of a sample is often comprised of a simple sum of the individual component nonlinearities. As shown in the previous

section, the concentration test in Fig. 4.3 illustrates that at any given concentration, the sample signal is given by a sum of the sample compound's nonlinearity weighed by its concentration, and the THF solvent matrix. However, these signals also include the signal from the sample holder. Thus, the intercept in the figure is represented by a sum of the THF and blank cuvette signals, or "reference" signals. Hence, obtaining $\chi^{(3)}_{THF}$ values from a reference scan involves separating the cuvette signal from the THF signal. We have shown that such separation is easy in solvent mixtures, but can we separate the signal of a liquid sandwiched between two glass walls, from the signal of the walls themselves? There are several possible complications in such a procedure. One consideration has to be the fact that the cuvette-solution system does not represent the same kind of additive mixture of molecules that a solvent-solute system does. The cuvette is solid and separate from the liquid it contains. This consideration actually simplifies the analysis, as molecular number density is not an issue, and an expression of $\chi^{(3)}_{R} = \chi^{(3)}_{quartz_wall} + \chi^{(3)}_{THF} + \chi^{(3)}_{quartz_wall}$ is obtained. The second, and most important consideration is the fact that the pump and probe beam overlap is finite and represents a varying overlap gradient as the two beams approach complete overlap. If the overlap is tightly focused on the sample, the interaction length may not be long enough to encompass the entire cuvette. These considerations are presented in Fig. 4.4. Furthermore, the signal from the outer regions of the cuvette walls may be smaller than that from the inner edges of the walls as the overlap becomes more complete. This raises two concerns: i) can $\chi^{(3)}_{R}$ be given by $\chi^{(3)}_{cuvette} + \chi^{(3)}_{THF}$ instead of $\chi^{(3)}_{quartz\ wall} + \chi^{(3)}_{THF} + \chi^{(3)}_{quartz\ wall}$; and (ii) if $\chi^{(3)}_{cuvette}$ is to be calculated, can we assume the same beam intensity profiles as those used to calculate $\chi^{(3)}_{THF}$?

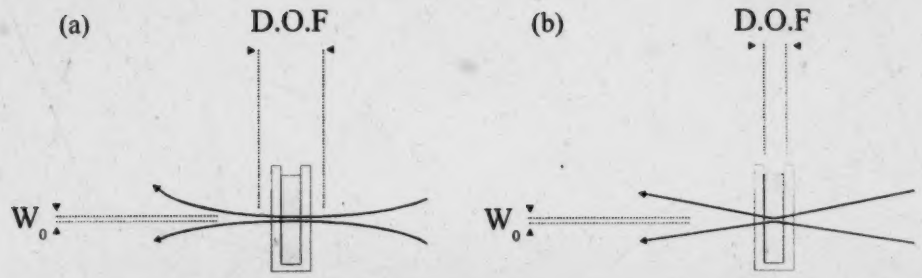

Figure 4.4: **Depth of focus (D.O.F) and Gaussian beam waist (W_0). (a) A gradual focus allows for a long depth of focus, and the entire sample cell experiences a similar beam intensity profile. (b) A sharp focus with a short depth of focus; the sample in the centre experiences a markedly different intensity profile than the outer cell walls. The depth of focus is the range over which the beam diameter, W, is smaller than $\sqrt{2} \times W_0$.**

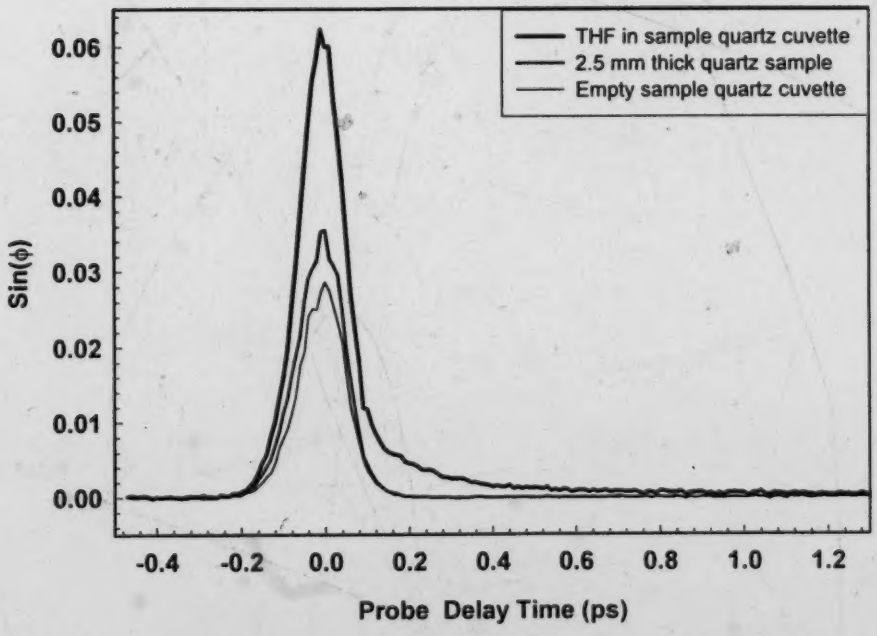

Figure 4.5: **A comparison of Kerr signals from a THF sample, a 2.5mm sample of Quartz, and an empty quartz sample cuvette.**

These questions can be answered by examining Fig. 4.5. In Fig. 4.5 three DOKE signals are presented; a THF reference, an empty cuvette and a 2.5 mm thick piece of quartz glass. This is a typical result in which the typical "blank" signal (that of the sample holder) is not zero, and is roughly half of the THF reference signal [45]. As mentioned previously, the cuvette is comprised of a 1.0 mm quartz wall, followed by a 1.0 mm long sample chamber and another 1.0 mm quartz wall. Ideally, the cuvette signal should equal that of a 2 mm solid quartz sample placed at the sample location. The signals in Fig 4.5 are directly proportional to $\chi^{(3)}$ and the pump-probe interaction length. The 2.5 mm quartz sample yields an approximate signal of $\sin\phi=0.034$. This corresponds to a signal of $\sin\phi=0.027$ for a 2.0 mm sample of quartz, at the sample location. Since the blank cuvette signal is, indeed, $\sin\phi=0.027$ it may be concluded that the two individual 1.0 mm walls of the cuvette may be considered a single 2.0 mm thick piece of quartz. Furthermore, because the cuvette signal is equal to the signal from a 2.0 mm thick quartz sample, it may be concluded that the pump-probe interaction length is greater than 3.0 mm, and the overlap intensity profile may be considered constant over the entire cuvette. Thus, the reference signal may be broken down into two components, yielding $\chi^{(3)}_{THF}$ and γ_{THF} from $\chi^{(3)}_{R} = \chi^{(3)}_{cuvette} + \chi^{(3)}_{THF}$.

4.4 *Comparing results with the literature*

There are many factors that contribute to incongruent third-order nonlinearity values reported in the literature. First of all, it is difficult to compare exact $\chi^{(3)}$ and γ values from two different experimental or theoretical techniques [19,46]. Such techniques include third harmonic generation (THG), degenerate four wave mixing (DFWM) and the optical Kerr effect. With that said, there are innumerable traps both in the experiments themselves as well as in their analysis that give rise to such incongruities [13]. Experimentally, the following factors, among others, must be considered; resonant contributions to the nonlinearities; dispersion effects when working with different wavelengths; accurate mapping of the spatial overlap of the pulses as well as beam spot diagnostics; and different local field effects arising in liquid, solid, and gas-phase

samples. Finally, the beam's pulse width is of extreme importance as different pulse widths excite different Kerr signal profiles, and may lead to the reporting of $\chi^{(3)}$ values that contain large, non-instantaneous components. There are several definitions of $\chi^{(3)}$ in the literature, each varying by some small factor from the others. Thus, there is a need for a consistent convention of defining the nonlinearity when reporting $\chi^{(3)}$ values [47]. In addition, the current trend of extrapolating the bulk third-order nonlinear susceptibility, $\chi^{(3)}(100\%)$, from that of a solution is questionable as it is normally derived from weight-percent, rather the molecular concentration. Furthermore, $\chi^{(3)}(100\%)$ is popularly reported as a pure, bulk value of the solute [48], when in practice it is often obtained from the solvent density and index of refraction. Therefore there is the added problem of considering the solvent matrix used when comparing $\chi^{(3)}(100\%)$ values. An alternative method of accounting for sample concentration in $\chi^{(3)}$ is presented in Appendix F.

Despite the problems with obtaining and comparing exact $\chi^{(3)}$ and γ values, it is extremely useful to report the nonlinearities relative to some reference material. Quite often, that reference material is the solvent. Thus, when reporting exact values obtained from relative values, the values for the reference material should be reported (see §5.1).

From the discussion above, it is clear that simply generating $\chi^{(3)}$ values that are comparable to those reported in the literature may not be a sufficient indication of proper Kerr effect detection. However, there are several typical material responses which can act as verification of proper detection. Two such features are the slow decay tail of the CS_2 Kerr effect signal, and the excitation of vibrational modes in CCl_4. The Kerr responses of these samples are reported in Appendix D.

5 RESULTS AND DISCUSSION

5.1 Absolute reference and THF Nonlinearities

In general, the THF reference is measured in order to eliminate the need for exact $\chi^{(3)}$ and γ values, allowing relative values to be reported instead. With the aid of references, exact values can be calculated by comparing the relative nonlinearities of the samples with the exact nonlinearity of the references. Thus, exact reference nonlinearity values are required.

Figure 4.5 may also be used to calculate the third-order nonlinearities of the reference, as well as of pure THF. A pump power of 4.0 mW ± 0.1 mW is incident on the sample with a spot size of 490 μm ± 20 μm [49]. The induced phase retardations are ϕ_R=0.062±0.002 and $\phi_{cuvette}$=0.027±0.002, giving a retardation of ϕ_{THF}=0.035±0.004 from $sin\phi_R = sin(\phi_{cuvette}+\phi_{THF})$ and $sin\phi \cong \phi$ for $sin\phi < 0.1$. Using Eqs. 1.12, 1.19 and 1.22, along with the preceding conditions, the third-order nonlinearities of the reference and of pure THF are found to be:

$$\chi^{(3)}_R = (2.1 \pm 0.3) \times 10^{-14} \text{ esu} \tag{5.1}$$

$$\chi^{(3)}_{THF} = (1.2 \pm 0.3) \times 10^{-14} \text{ esu} \tag{5.2}$$

Equation 1.16 allows us to calculate γ_{THF} from the nonlinear susceptibility.

$$\gamma_{THF} = (5.2 \pm 1.3) \times 10^{-37} \text{ esu} \tag{5.3}$$

The above values are exact (non-relative) values and are not reference dependent. They are used as reference values when relative $\chi^{(3)}$ and γ values are computed from the various experimental results. Sample calculations for Eq. 5.2 and Eq. 5.3 are provided in

Appendix G. The relative third-order nonlinearity for any sample is obtained directly from the DOKE peak signals (such as those presented later in Fig. 5.1) using

$$\chi_S^{(3)} = \chi_R^{(3)}\left(\frac{\phi_S}{\phi_R}\right), \tag{5.3}$$

or

$$\gamma_S = \frac{\chi_R^{(3)}\left(\frac{\phi_S}{\phi_R} - 1\right)}{L^4 N_C}. \tag{5.4}$$

where $\chi_S^{(3)}$, γ_S, $\chi_R^{(3)}$, and γ_R are the sample susceptibility, sample hyperpolarisability, reference susceptibility, and reference hyperpolarisability, respectively; ϕ_S and ϕ_R are, respectively, the measured rotation in polarisation of the sample and reference. We use THF as a reference for all samples. It should be noted that each sample scan will have its own THF reference signal, obtained in close succession, allowing for individual referencing of each sample signal. Thus, the reference values presented in Eqs. 5.1-5.3 are independent of $\sin\phi_S/\sin\phi_R$ signals used in Eq. 5.4. and Eq. 5.5.

5.2 *Scan Series*

In order to obtain reportable nonlinearity values, several scans must be conducted on each sample. Not only are several consecutive scans averaged to make a single profile, as discussed in §2.3, but several averages taken at different times must also be obtained to assure repeatability. Since the samples are somewhat perishable (in part, due to solvent evaporation), we must obtain many scans of various samples in fast succession, guaranteeing the maximum number of profiles from which final $\chi^{(3)}$ and γ values may be reported. As mentioned previously, THF references are obtained before and after nearly

every sample scan to assure more accurate referencing. Often, reference scans are averaged to yield a reference profile for that particular "sandwiched" sample scan. Since long-term stability in the spatial overlap of the pump and probe beams is difficult to attain, and depends, for the most part, on the D-mirror alignment, scan series are normally obtained at a particular D-mirror setting. Once alignment-drift becomes apparent, the D-mirror position is readjusted and a new scan series begins. Thus, it is possible that one scan series will have overall larger Kerr signals than another. It is also possible, however, to collect a scan series where signals are still high, but where referencing shows results inconsistent with the other scan series. Furthermore, it is generally true that as the experiment progresses, fluctuations in the laser beam reduce and overall laser drift diminishes, providing consistent Kerr signals with reduced-noise. Thus, the first scan series of an experiment is often yields low-quality results compared with later scans.

In order to study sample dynamics and relaxation times, only time-resolved scans may be used. However, sole interest in γ values permits two types of Kerr scans; time-resolved, and on-peak. Each time-resolved scan provides a $\chi^{(3)}$ value from the peak signal at τ_D=0. The error in such a measurement is difficult to ascertain, and to obtain a value with which we are confident involves taking numerous scans. Considerable on-peak noise provides for large on-peak signal uncertainties in time resolved scans. However on-peak scans, in which hundreds of data points are taken at τ_D=0, provide a good indication of the error associated with each peak value. A drawback of such scans is the absence of any time-resolved information. Thus, on-peak scans are used in conjunction with time-resolved scans to bolster the number of $\chi^{(3)}$ values added to the overall population, giving us a good indication of the average $\chi^{(3)}$ values along with their uncertainties. In the past, research groups, only interested in absolute $\chi^{(3)}$ values rather than time-resolved nonlinearity profiles, have exclusively used on-peak scanning [50].

5.3 *Oligomer Series Nonlinearities*

5.3.1 *Time-Resolved Scans*

Figure 5.1 presents an example of the type of DOKE signals obtained for the iso-polydiacetylene oligomer series. As described in §2.2, *sinϕ'* is obtained by dividing the A-B signal by the post-sample probe reference, A+B signal. However, these scans are not normalised to the THF reference, and the full reference signal is presented in the figure. The sample concentrations decrease as the chain length increases due to reduced availability of the longer oligomers. Thus, for example, the heptamer sample shows a nonlinear response that is nearly equal to that of the pentamer sample response.

This data shows incredibly low baseline noise, with a signal-to-noise ratio exceeding 1,500:1! The only modifications made to the raw Kerr signals is a slight shifting of the signal levels to yield a zero baseline at negative probe delay times. Our DOKE signals always show increased noise on-peak. This noise is evident in Fig 5.1. The smooth signal slopes give way to jagged tops. Each of the Kerr signals presented in Fig. 5.1 is an average of 5 scans. Small, random noise averages to give excellent signal-to-noise ratios everywhere except on-peak. The individual, unaveraged, scans show some noise throughout the signal profile. However, the on-peak noise is often excessive. This effect has been seen by many research groups and has been attributed to transient, coherent grating effects [26,34]. We have observed that, in general, it is possible to align the D-mirror in a manner where such grating effects are minimised, yielding smoother signal peaks. Nonetheless, it is nearly impossible to estimate the amount of noise that is present on-peak without obtaining a scan. Thus, aligning the D-mirror to a position that has little on-peak noise is difficult, and approximately one-in-ten tries yields an overlap condition with little on-peak noise. To counter this, scan averaging is employed, and as seen in Fig. 5.1, such averaging is sufficient to yield acceptably smooth on-peak signals. It is this on-peak noise that gives rise to the large uncertainty in $\chi^{(3)}$ values, since only the

peak value in time-resolved scans contributes to the measurement and calculation of nonlinear coefficients in materials dominated by electronic nonlinearities.

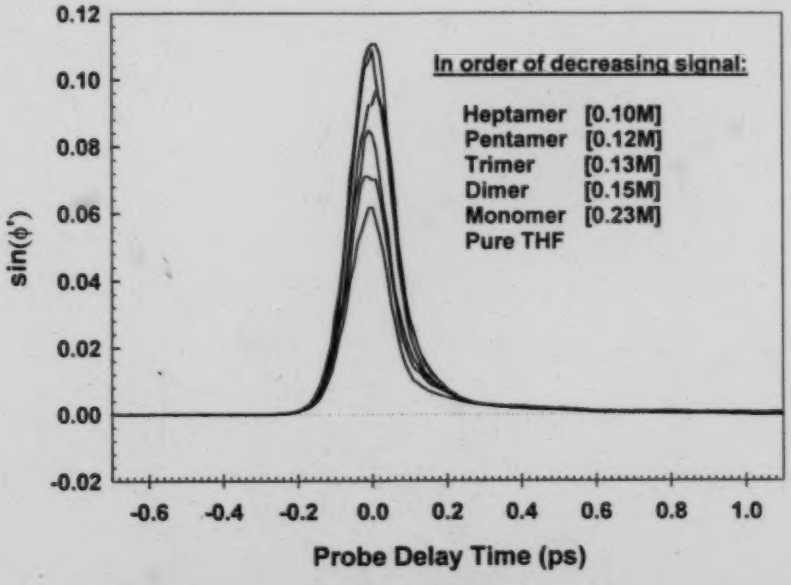

Figure 5.1: Time-resolved Kerr response of THF reference/solvent and iso-PDA oligomer sample solution. The molarity of each sample in THF is indicated in square brackets.

5.3.2 On-Peak Scans

As mentioned in §5.2, on-peak scans are employed to provide a better indication of the statistically-averaged nonlinearities. Figure 5.2 presents an example of a single on-peak, τ_D=0, scan obtained for the monomer sample. Clearly, there is considerable on-peak noise. This scan consists of 300 data points. The nonlinear signal, A-B, shows a mean of 2.54 A.U. with a standard deviation of 0.20 A.U., corresponding to 8% of the signal. On the other hand, the reference signal, A+B, shows a mean of 2.01 A.U. with a standard deviation of 0.02 A.U., corresponding to 1% of the signal. Thus, the on-peak Kerr response shows considerably greater noise than that found in the reference signal.

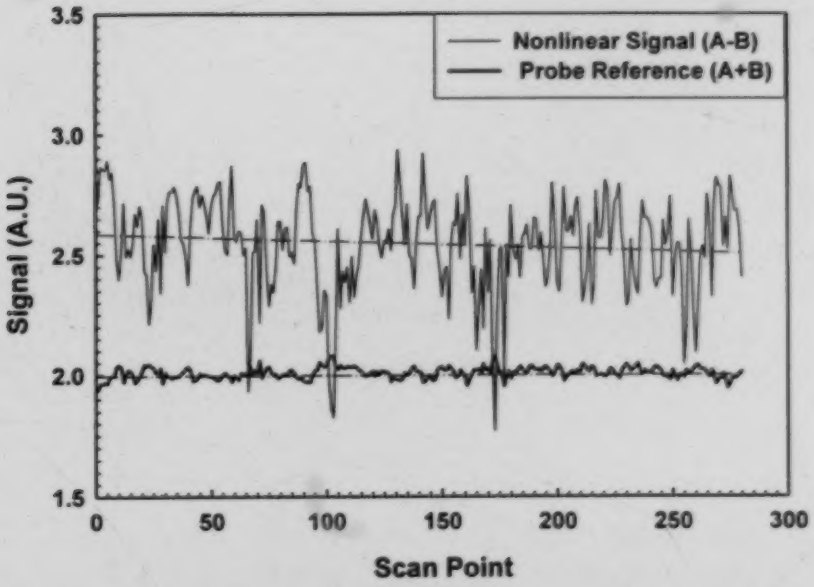

Figure 5.2: On-peak A-B (nonlinear Kerr response) and A+B (probe reference) signals for a monomer sample. The nonlinear response shows considerably more noise than the probe reference signal. Dashed lines are guides to the eye.

The A-B signal shows three kinds of noise. First, is the random noise observed in the A+B signal. This noise is due to laser fluctuations and electronic noise; it is unavoidable, random, and relatively small. Second, is the noise inherent to τ_D=0 overlap that fluctuates evenly above and below the mean value. This noise level changes each time the pump-probe overlap is realigned. This noise is generally seen to disappear at overlap times removed from τ_D=0. The third noise source is seen in Fig. 5.2 as large downwards spiking of the A-B signal. This noise is due to laser misfiring. Hence, this noise is systematic and always skews the signal to lower values. Because the lock-in amplifier averages signals over several time constants, such misfiring of the laser does not produce a zero signal; it does, however, reduce the signal considerably. Following the statistical analysis given in [51], a lower and upper hinge method for outlier removal was used in an attempt to remove laser misfiring noise. We were able to remove several outliers from the signal presented in Fig. 5.2, yielding new mean and standard deviation

values for A-B. The statistically corrected nonlinear signal, A-B, shows a new mean of 2.57A.U. with a standard deviation of 0.16 A.U, corresponding to 6% of the signal. Thus, the removal of laser misfiring does not seem to significantly alter the results. Although laser misfiring does not seem to affect $\chi^{(3)}$ measurements taken on-peak, it does affect the time-resolved scans. With time-resolved scans it is not practical to obtain hundreds of data points on peak, and we are only able to resolve the peak with 5-10 data points. Thus, on peak noise seriously compromises our ability to provide a precise $\chi^{(3)}$ value from time-resolved scans. Therefore, the two types of scans, time-resolved and on-peak, complement each other and provide us with a good indication of the samples' third-order nonlinearities.

5.3.3 Sample Second Hyperpolarisabilities

For each sample, all individual time-resolved and on-peak scans combine to produce a single γ value. Table 5.1 lists relevant properties and results for the oligomer series. Figure 5.3 presents the final, relative hyperpolarisabilities of the various oligomer samples. The magnitude of γ for this compound series is around 10^{-35}esu. The cross-conjugated oligomers are not expected to yield high nonlinearities compared with counterpart linearly-conjugated polydiacetylenes (see §1.1). Nonetheless, the oligomer samples show large nonlinearities compared with our THF reference. The monomer sample is of the same order of magnitude as our reference, while the heptamer shows an increased nonlinearity of an order of magnitude over the monomer sample. With the limited oligomer length extension, we see that the third-order nonlinearities of these samples increase monotonically as a function of chain length for all samples studied. This result is expected from the increase in the number of linear chain segments resulting from an increase in the number of repeat units. Thus, at the very least, it is shown that the third-order nonlinearities of an oligomer possessing a cross-conjugated backbone increase as a function of oligomer length.

Table 5.1: **Summary of results for the iso-polydiacetylene oligomer series. γ_s and γ_{THF} are the second hyperpolarisabilities of the oligomer samples and THF reference, respectively. n is the number of repeat units in the oligomer.**

Sample	n	Concentration (M)	γ_S $\times 10^{-36}$esu	$\frac{\gamma_S}{\gamma_{THF}}$
Monomer	1	0.23	9.2±0.4	17.7±0.8
Dimer	2	0.15	30.3±0.3	58.2±0.5
Trimer	3	0.13	49±4	94±7
Pentamer	5	0.12	69±5	134±9
Heptamer	7	0.10	95±4	181±9

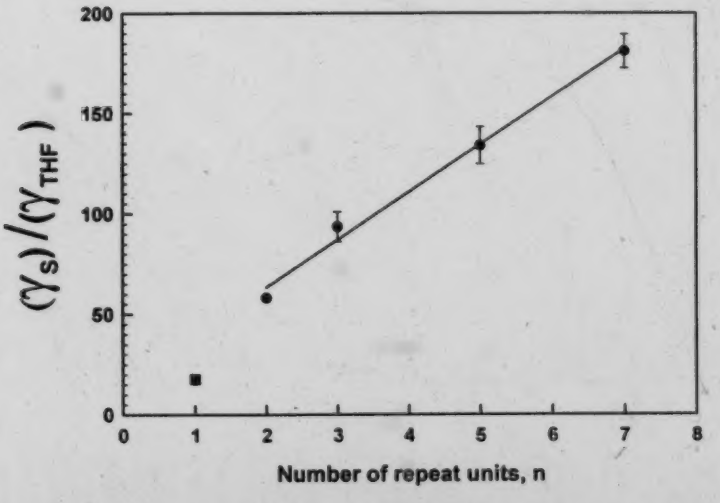

Figure 5.3: **Molecular second hyperpolarisability of the oligomer samples, γ_S, relative to the absolute THF hyperpolarisability, γ_{THF}, as a function of oligomer repeat length, n. The solid line is a linear fit to the data for n = 2, 3, 5, and 7 (dimer to heptamer).**

The general theory holds that no added communication in long cross-conjugated molecules should be present beyond that due to the linearly-conjugated path. As the number of repeat units is increased, there is an increase both in the total number of linearly-conjugated paths and an increase in the cross-conjugated path length. Adding repeat units increases the number of fixed-length linearly-conjugated paths, while

increasing the length of the contiguous cross-conjugated backbone. Adding a repeat unit to the dimer, adds one linearly-conjugated segment; likewise for the trimer, pentamer and so forth. Thus, the effect of communication due to linear-conjugation should appear as a linear relationship in Fig. 5.3. Increases in γ due to bolstered delocalisation along the cross-conjugated backbone is expected to produce a super-linear relationship between γ and the number of repeat units, n. The regression line in Fig. 5.3 implies the absence of cross-conjugated communication, as the monomer-to-heptamer nonlinearities increase linearly with chain length. Cross-conjugated communication, however, is expected to be quite small, and may not be observable for such small oligomer lengths. Extending the experiment to longer conjugation paths should afford more conclusive results.

It should be noted that in Fig. 5.3 the monomer is not expected to contribute linearly to γ. Although increasing n, from 2 to 3 adds a full fixed length linear-conjugation segment to the dimer, in the monomer sample, the length of the linear-conjugated path has not yet saturated, as may be seen in Fig. 4.1. Thus, in going from the monomer to dimer samples, some increases in γ are attributable to increases in conjugation length, as discussed in §1.1. Other evidence for fundamental differences between the monomer and the rest of the series may be seen from the differences in λ_{max} values displayed in Fig. 4.2(b). In these samples, the band gap energy is seen to be fairly constant from the dimer to the heptamer, consistent with the idea that π-delocalisation does not increase much with an increasing number of repeat units. In analogy to coupled harmonic oscillators, where each repeat unit is a single oscillator, the ease of electronic communication from one unit to the next is a measure of the coupling strength in these systems [52]. It has been shown that for strongly coupled systems, such as some linearly-conjugated oligomers, not only do the third-order nonlinearities increase with increasing coupling strength, but the linear absorption increases as well. In this framework, it may be concluded that the fact that λ_{max} is fairly stationary for $n>2$ is further evidence for limited communication across the cross-conjugated bridge. However, Fig. 4.2 shows that λ_{max} increases considerably from the monomer to the dimer, implying a significant lowering of the band gap.

Attempting to model the monomer and dimer responses by carefully tallying the number and length of the linear-conjugation paths is tedious and of limited use. Instead,

by looking at the longest linear-conjugation length (the property that contributes most to the molecular hyperpolarisability) one may predict that the dimer, having a longest path nearly double in length of the monomer path, should show at least a doubling of the nonlinearity. Furthermore, the length-normalised response may be expected to remain constant between the monomer and dimer. However, in the monomer and dimer samples, the end groups make up a large part of the molecule, as well as a large part of the linear conjugation length. Linear conjugation in the monomer extends from an aryl group to a silicon, while in the dimer, the conjugation is between two aryl groups. Thus, differences in electron-donor/acceptor characteristics of the functional groups contribute to the differences in hyperpolarisabilities between the monomer and the rest of the oligomer series [11]. Again, as the oligomer chain length increases, changes in end-group layout become less pronounced, and the major change in the molecule becomes the number of repeat units. Thus, because of differences both in end-group geography and linear conjugation path lengths, comparisons of the monomer's nonlinearities to those of the rest of the oligomer series are ambiguous.

The preceding results contribute to the idea of structure-property additivity. As mentioned in §1.1, several research groups have found additivity rules for many functional groups, providing added terms to a "formula" that may predict the effects of various molecular environments on sample nonlinearities. The results of our experiments have shown that a system constructed via cross-conjugated building blocks will add to the molecular nonlinearities as an isolated entity.

5.3.4 *A Non-Instantaneous Sample Response Component*

In solution, unless the samples exhibit marked differences in nonlinear molecular dynamics from the solvent, the time-resolved excitation profiles will follow that of the solvent. The THF signal shows a nearly symmetric excitation attributed to the purely-electronic polarisation. There is a small, non-instantaneous component to the signal. This component is due to the small asymmetry in THF and is attributed to nuclear responses. The small nuclear response is easy to resolve when comparing THF Kerr signals to those of samples with purely electronic (instantaneous) responses such as fused quartz (see Fig. 4.4). On initial inspection of the sample signals in Fig. 5.1, it appears that their excitation profiles follow that of the THF reference, showing no inherit long-time dynamics. However, as seen in Fig. 5.4, close inspection clearly reveals a feature that can be described as a distinct hump that arises out of the otherwise smooth signal decay tail at 0.4 ps. More information regarding how the concentration normalising was obtained for the signals in Fig. 5.4 may be found in Appendix F. This feature is unique to the oligomer samples as it is clearly absent from the solvent response. Furthermore, this excitation appears to have a fairly quick rise time as is seen from the sharp "kink" in the heptamer signal. The feature is very small, at a little less than 1% of the peak electronic signal, and cannot at present be separated from the relaxing signal tail. In addition, the feature is seen to grow in strength from the monomer to the heptamer, yet it remains at the same delay time for all of the samples. The low signal and limited resolution currently prevent further analysis, and the origin of this feature is not fully understood at this time. Future studies, especially with *iso*-PDAs extended to longer chain length, should yield better resolution of this feature.

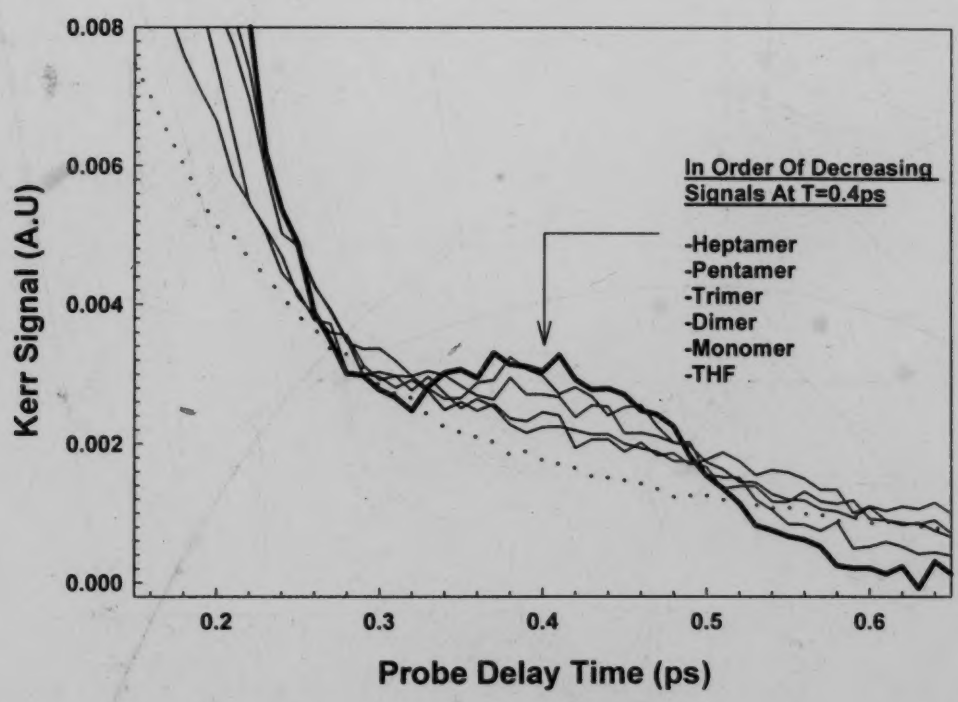

Figure 5.4: **Magnified view of the tail region of the Kerr response for the oligomer samples showing a non-instantaneous excitation feature at 0.4 ps. The size of the hump increases with n, but remains at the same temporal position for all samples. The dotted line is a THF reference showing no deviation from smooth signal decay. To emphasise the presence of the hump, Kerr signals for each sample have been normalised to the monomer concentration. The hump does not appear at negative time delays.**

6 CONCLUSIONS

We have constructed a modular optical Kerr gate that may be used to study the ultrafast third-order nonlinearities of liquid samples. In contrast to most setups used in this field, we employ amplified, 800 nm, 1 kHz repetition rate, 100 fs laser pulses, to both excite and probe the molecular and bulk sample nonlinearities. In addition to showing that our setup is capable of both the standard homodyne and heterodyne (OHD-OKE) detection techniques, we have developed a new detection layout, differential optical Kerr effect (DOKE). DOKE detection represents a considerable modification of the OHD-OKE technique. The advantages to this new technique are that signal detection is both simpler and more intuitive than the OHD-OKE technique, while maintaining the ability to separate the real and imaginary components of the third-order nonlinear susceptibility. Furthermore, as in OHD-OKE detection, the DOKE technique provides Kerr response signals that are linear in both pump and probe beam intensities. DOKE signals are both larger in magnitude and have a larger dynamic range of linear signal behaviour compared with other techniques. Both mathematical and physical descriptions of DOKE detection have been given, with the goal of presenting proof of proper detection as well as instruction to those who may wish to use DOKE detection as their Kerr gate technique. In addition, practical issues associated with ultrafast laser spectroscopy have been addressed and possible solutions to these problems were discussed.

DOKE detection was used to study the third-order nonlinearities of iso-polydiacetylenes (iso-PDAs); a novel class of compounds that contain cross-conjugated backbones. Unlike traditional polydiacetylenes that contain long linearly-conjugated backbones, iso-PDAs are composed of a cross-conjugated framework. This particular phenylated iso-PDA oligomer series has a long cross-conjugated backbone that is hatched with fixed-length linearly-conjugated arms. In these compounds, the longest linearly-conjugated path does not increase with the number of repeat units. Instead, the number of fixed-length linearly-conjugated paths increases. Thus, we no longer have a molecule that polarises freely along its entire length, as compared with polydiacetylene oligomers. This property significantly affects the absorption energies of the oligomer. *iso*-PDAs

exhibit high energy absorption edges and are transparent at much longer chain lengths as compared to the polydiacetylenes [9]. The samples are completely transparent at 800 nm. Furthermore, for the cross-conjugated oligomer series, λ_0 values have reached saturation near the stage of the heptamer. These oligomers have the additional feature that, although one dimension has lower π-delocalisation along the cross-conjugated backbone, the transverse axis is hatched with linearly-conjugated arms affording increases in γ, compared to the monomer, without significant reduction of the optical transparency; an important property of all-optical switching. Values of $\gamma_{monomer}=(9.2\pm0.4)\times10^{-36}$ esu, $\gamma_{dimer} = (30.3\pm0.3)\times10^{-36}$ esu, $\gamma_{trimer} = (49\pm4)\times10^{-36}$ esu, $\gamma_{pentamer} = (69\pm5)\times10^{-36}$ esu, and $\gamma_{heptamer} = (95\pm4)\times10^{-36}$ esu were obtained, relative to a THF reference of $\gamma_{THF} = (0.52\pm0.12)\times10^{-36}$ esu. These compounds show a linear rise in the molecular second hyperpolarisability, γ, as the chain length is increased from the dimer to the heptamer. This increase in γ can be attributed to an increase in the number of fixed-length linearly-conjugated paths. The monomer sample fits sublinearly with the rest of the series due to a shorter linearly-conjugated path than the higher oligomers. No added contribution to the nonlinear response attributable to the cross-conjugated backbone has been observed for these iso-PDAs. To the best of our knowledge, this work represents the first time that the third-order nonlinearities of iso-polydiacetylenes have been investigated. Furthermore, this also represents the first study of the relationship between second hyperpolarisability and chain length for a fully cross-conjugated system.

Non-instantaneous behaviour is also observed in the samples. This behaviour arises in the oligomer signals roughly 0.4 ps after maximum pump-probe overlap and is not present in the solvent signal. In the heptamer sample, this feature appears as a kink in the decay profile, illustrating the quick rise-time of this feature. The low signal and limited resolution currently prevent further analysis, and the origin of this feature is not fully understood at this time.

7 Future Directions

This work established the validity of the DOKE detection setup. However, more work should be done to directly compare the OHD-OKE and DOKE techniques. We believe that quantitatively testing the limits of both techniques should indicate many advantages to DOKE detection over OHD-OKE.

Although we have shown how DOKE detection may be used to obtain the imaginary components to sample third-order nonlinearities, the detailed examination of samples with known $\mathrm{Im}(\chi^{(3)})$ processes should be undertaken to verify that aspect of the DOKE technique. There are some specific details that still need to be addressed in signal analysis for samples with nonlinear absorptive properties. The DOKE equations provide a clear starting point for such analysis, but they do not specifically account for the fact that the A+B signal is detected at the probe repetition frequency of 1kHz, while A-B is detected at the pump beam chopper frequency of 125Hz.

Finally, it is possible that small contributions to electronic communication along cross-conjugated paths will be resolved in oligomers longer than those studied. Furthermore, longer oligomers may undergo ordered folding/stacking that may have interesting nonlinear properties. Thus, extension of the iso-PDA series to longer oligomers should provide more concrete trends in sample nonlinearities. The study of longer oligomer lengths is in progress.

Appendix A

Lock-in Amplifier Considerations

Line Filters

Most Lock-in amplifiers have a "Line" filter and a "Line-2" filter. These filters remove 60 Hz and 120 Hz signal, respectively. Typically, the Line filter is quite useful because of ambient radiation from alternating-current in laboratory electronics, such as the florescent laboratory light fixtures. This radiation will often give background noise and removing it electronically is necessary. There is also the possibility 120 Hz light–that is, the direct florescent light—might add to the background noise. Thus Line-2 filters, that remove 120 Hz light, are often useful as well. However, these filters are not extremely narrow and still filter out some signal at up to double their designed frequencies. Our signal is modulated at 125 Hz, a frequency that is well within the range of the Line-2 filter. Figure A.1 illustrates the effects of these filters on a typical DOKE scan. Clearly, the line filter at 60 Hz does not affect our signal, as it neither has more noise nor less signal than the scans taken with the filters out. However, the Line-2 filter removes much of our signal. Thus, it is important to disable the Line-2 filter on the lock-in amplifier for any signals detected at 125 Hz. These scans were obtained with some, but minimal laboratory light on, thus, the ambient light does not seem to overly affect the scans.

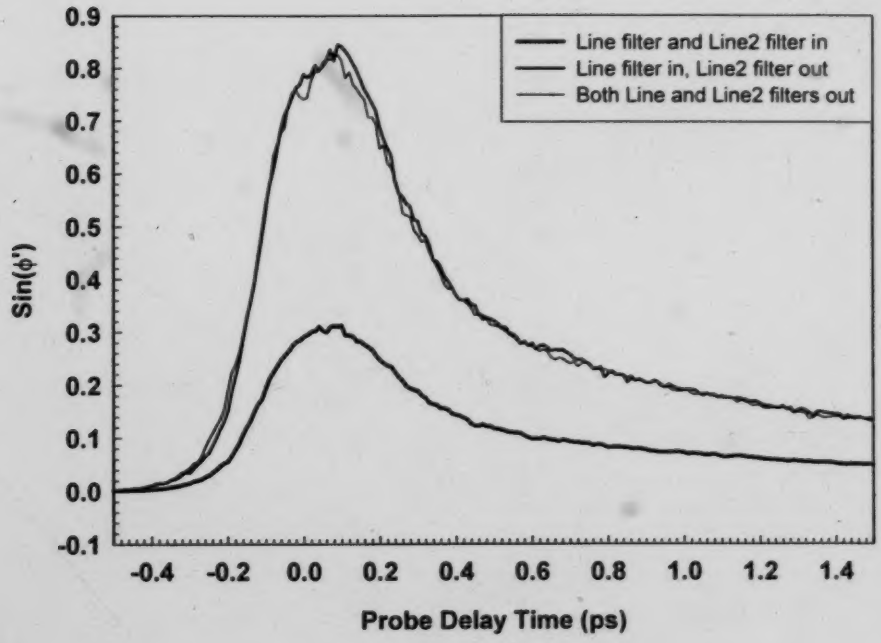

Figure A.1: CS_2 Kerr signals for various lock-in amplifier Line filter settings, showing significant signal removal.

Appendix B

Pump Beam Reference Detection

Our DOKE gate layout presented some challenges with regards to detection of a pump reference beam. First, the pump beam, by its very nature is intense and thus difficult to detect directly without saturating a photodiode detector. Second, real-estate issues restricted the use of large attenuators such as neutral-density filter wheels. Furthermore, there was no room for the pump reference beam setup at the same (6 inch) height at which the entire Kerr gate operated.

One method of sampling a portion of the beam is by use of a pellicle beam-splitter. This optical component is composed of an extremely thin, tightly stretched, dielectric. Because the polymer is very thin, the pellicle beam-splitter does not normally introduce any dispersions or deviations in the transmitted beam. Although the pellicle beam-splitter can be used to pick-off less than 5% of the total beam power, this amount is still enough to saturate the detector. In our setup, we need very low pump reference powers, even when the sample is being pumped with high intensities. For this application, we found that a glass slide-cover acting as a Brewster's window is ideal. Figure B.1 illustrates the pump beam reference setup. In our setup, the glass plate is mounted such that the pump beam is incident at Brewster's angle (53°) to the glass plate, and is then reflected downwards. At Brewster's angle, only beam components polarised normal to the plane of incidence (i.e. polarised horizontally) are reflected [53]. For our setup, the beam is polarised vertically and no light is reflected off the plate when it is mounted at Brewster's angle. Tilting the window slightly away from Brewster's angle allows an extremely small amount of light to be reflected downwards. Thus, we can pick-off some of the pump beam without saturating our reference detectors. In addition, because the slide cover is only 0.3 mm wide, it adds negligible dispersion and deviation to the pump beam. Light polarised horizontally is not as sensitive to the angle of the Brewster window and any such component in our beam will add considerably to the reference detector signal. Thus, a polariser is added to the reference arm to remove horizontally polarised light. With this

setup, we are able to obtain 5000:1 extinction ratios! Also, adjusting the window's tilt away from Brewster's angle allows us to work in various dynamic ranges. After the pick-off beam is directed downwards, it is maintained at the 3" height, below the 6" level of the Kerr gate. This provides us with more room for the reference beam detection. A drawback for this method of pump beam reference detection is that it is prone to misalignment at the slide-cover.

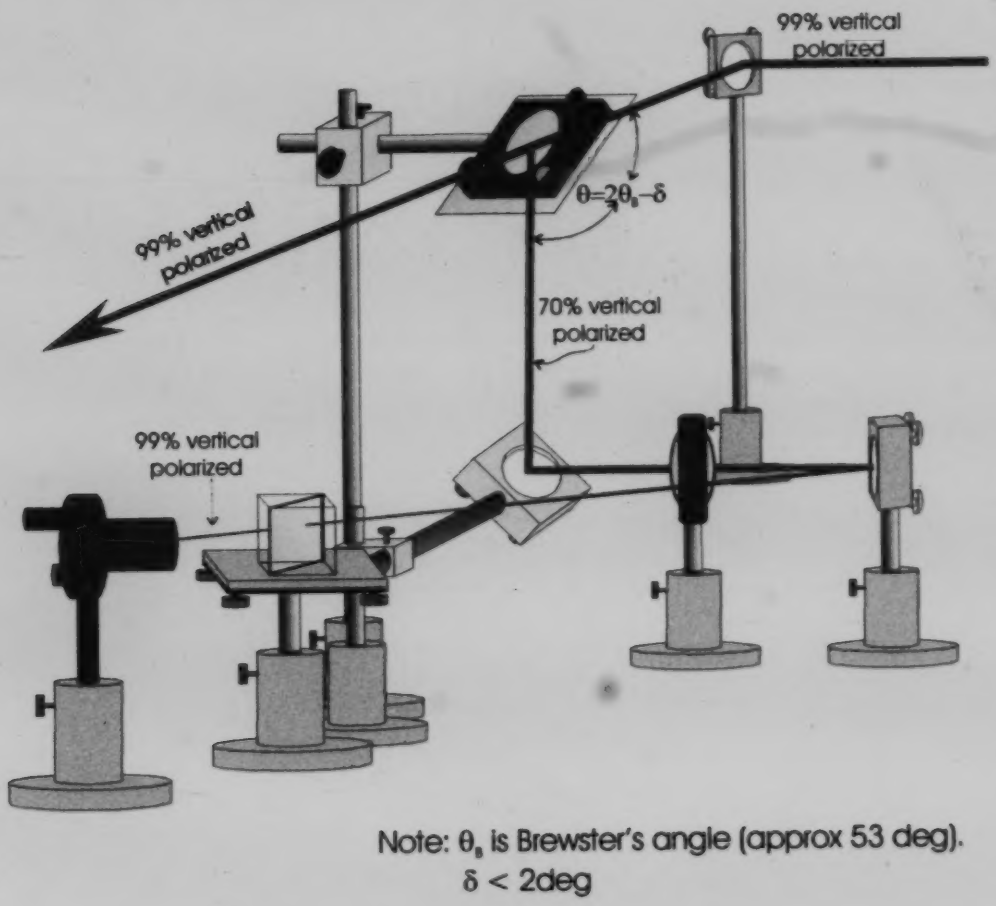

Figure B.1: **Pump beam reference detection layout. The pump beam is split by a glass window set at Brewster's angle, and sent downwards from the 6" height to the 3" height. Pump beam is initially polarised vertically.**

Appendix C

OHD-OKE and DOKE signal detection

The fundamental differences between optically heterodyned detection set-ups and differential optical Kerr effect detection set-ups have been discussed in §2.1. Briefly, OHD-OKE uses the polariser-quarter wave plate differently than DOKE. Furthermore, OHD-OKE detects only one element of the out-going probe beam, namely, the x-component, whereas differential detection separates the horizontal x-component from the vertical y-component and uses both for signal detection.

The following is a matrix algebra derivation of the equations given in §2.2. Some of the abbreviations used in the derivation are found in Table C.1. Note that brackets after a matrix symbol denote angle of alignment or the angle of pumping polarisation. For example, λ/4(45) represents a quarter-wave plate oriented with the fast axis at 45° to the horizontal; while S(90) represents a sample pumped with a vertically polarised pump beam. All angles are with respect to the horizontal, where positive angles denote counter-clockwise rotation when looking along the beam.

In general, the induced phase retardation, ϕ, is a complex variable such that $\phi = \phi' + i\phi''$. Both OHD-OKE and DOKE are designed to separate the real and imaginary signal components.

Table C.1: **Some symbols and matrix representations for various optical elements.**

Symbol	Description	Matrix Representation	Notes
λ/4(45)	Quarter-Wave Plate	$\begin{bmatrix} i & 0 \\ 0 & 1 \end{bmatrix}$	Fast axis aligned 45 degrees to horizontal
P	Polariser	$\begin{bmatrix} 0 \\ 1 \end{bmatrix}$	Allows only, y (vertical light) through
A	Analyser	$\begin{bmatrix} 1 & 0 \end{bmatrix}$	Allows only x (horizontal light through)
DA	Differential Analyser	$\begin{bmatrix} 1 & 1 \end{bmatrix}$	Separates the horizontal from the vertical light.
S	Sample	$\begin{bmatrix} 1 & 0 \\ 0 & e^{i\phi} \end{bmatrix}$	Sample is a retarder allowing a ϕ phase retardation.
R(45)	Rotation Matrix	$\frac{1}{\sqrt{2}}\begin{bmatrix} 1 & -1 \\ 1 & 1 \end{bmatrix}$	Rotation of 45 degrees
R(δ)	Rotation Matrix	$\begin{bmatrix} \cos\delta & -\sin\delta \\ \sin\delta & \cos\delta \end{bmatrix}$	General rotation matrix

Standard OHD-OKE

The standard optical heterodyne detection layout is P(θ)-λ/4(90)-S(45)-A(0), where the probe beam is incident, in order, upon a polariser set at an angle, $\theta = \pi/2 + \delta$, slightly off vertical; a quarter-wave plate aligned with fast axis along vertical; a sample that was pumped at 45° to horizontal; and an analyser that only passes horizontal light through allowing only the x-component of the out-coming beam to be detected.

$$D=\frac{1}{2}\begin{bmatrix}1 & 1\\ -1 & 1\end{bmatrix}\begin{bmatrix}1 & 0\\ 0 & e^{i\phi}\end{bmatrix}\begin{bmatrix}1 & -1\\ 1 & 1\end{bmatrix}\begin{bmatrix}i & 0\\ 0 & 1\end{bmatrix}\begin{bmatrix}\cos\delta & -\sin\delta\\ \sin\delta & \cos\delta\end{bmatrix}\begin{bmatrix}0\\ 1\end{bmatrix}$$

Where D is the detector signal matrix. Multiplying out, we get

$$D=\begin{bmatrix}D_x\\ D_y\end{bmatrix}=\frac{1}{2}\begin{bmatrix}-i\sin\delta\left(1+e^{i\phi}\right)-\cos\delta\left(1-e^{i\phi}\right)\\ i\sin\delta\left(1-e^{i\phi}\right)+\cos\delta\left(1+e^{i\phi}\right)\end{bmatrix}$$

OHD-OKE is only concerned with detecting the x-component of the signal. Thus, the detected beam intensity is

$$I_x=D_xD_x^*=\frac{1}{4}\left[-i\sin\delta\left(1+e^{i\phi}\right)-\cos\delta\left(1-e^{i\phi}\right)\right]\left[i\sin\delta\left(1+e^{-i\phi^*}\right)-\cos\delta\left(1-e^{-i\phi^*}\right)\right]$$

Where "*" denotes the complex conjugate.

$$\begin{aligned}I_x=&\frac{1}{4}[\sin^2\delta\left(1+e^{i\phi}+e^{-i\phi^*}+e^{i\phi-i\phi^*}\right)-i\cos\delta\sin\delta\left(1-e^{-i\phi^*}+e^{-i\phi}-e^{-i\phi^*+i\phi}\right)\\
&+i\cos\delta\sin\delta\left(1+e^{-i\phi^*}-e^{-i\phi}-e^{-i\phi^*+i\phi}\right)+\cos^2\delta\left(1-e^{i\phi}-e^{-i\phi^*}+e^{i\phi-i\phi^*}\right)]\\
=&\frac{1}{4}[\sin^2\delta\left(1+2e^{-\phi^*}+e^{-2\phi^*}\right)-i\cos\delta\sin\delta\left(1+2i\sin\phi^*e^{-\phi^*}-e^{-2\phi^*}\right)\\
&+i\cos\delta\sin\delta\left(1-2i\sin\phi^*e^{-\phi^*}-e^{-2\phi^*}\right)+\cos^2\delta\left(1-2e^{-\phi^*}+e^{-2\phi^*}\right)]\\
=&\frac{1}{4}[\sin^2\delta\left(1+2e^{-\phi^*}+e^{-2\phi^*}\right)+\cos^2\delta\left(1-2e^{-\phi^*}+e^{-2\phi^*}\right)\\
&-i\cos\delta\sin\delta\left(1+2i\sin\phi^*e^{-\phi^*}-e^{-2\phi^*}-1+2i\sin\phi^*e^{-\phi^*}+e^{-2\phi^*}\right)]\\
=&\frac{1}{4}[\sin^2\delta\left(1+2e^{-\phi^*}+e^{-2\phi^*}\right)+\cos^2\delta\left(1-2e^{-\phi^*}+e^{-2\phi^*}\right)+4\cos\delta\sin\delta\sin\phi^*e^{-\phi^*}\end{aligned}$$

$$I_x = \frac{1}{4}[1 + e^{-2\phi''} + 2e^{-\phi''}\cos\phi'(\sin^2\delta - \cos^2\delta) + 4\cos\delta\sin\delta\sin\phi' e^{-\phi''}]$$

$$= \frac{1}{4}[(1 - e^{-\phi''})^2 + 2e^{-\phi''} + 2e^{-\phi''}\cos\phi'(1 - 2\cos^2\delta) + 4\cos\delta\sin\delta\sin\phi' e^{-\phi''}]$$

$$= \frac{1}{4}[(1 - e^{-\phi''})^2 + 2e^{-\phi''}(1 + \cos\phi' - 2\cos^2\delta\cos\phi' + 2\cos\delta\sin\delta\sin\phi')$$

$$= \frac{1}{4}(1 - e^{-\phi''})^2 + \frac{1}{2}e^{-\phi''}(1 - \cos\phi'(2\cos^2\delta - 1) + \sin(2\delta)\sin\phi')$$

$$= \frac{1}{4}(1 - e^{-\phi''})^2 + \frac{1}{2}e^{-\phi''}(1 - \cos\phi'(\cos^2\delta - \sin^2\delta) + \sin(2\delta)\sin\phi')$$

$$I_x = \frac{1}{4}(1 - e^{-\phi''})^2 + \frac{1}{2}e^{-\phi''}(1 - \cos\phi'\cos 2\delta + \sin(2\delta)\sin\phi')$$

$$= \frac{1}{4}(1 - e^{-\phi''})^2 + \frac{1}{2}e^{-\phi''}(1 - \cos(\phi' + 2\delta))$$

$$\boxed{I_x = \frac{1}{4}(1 - e^{-\phi''})^2 + e^{-\phi''}\sin^2\left(\frac{1}{2}\phi' + \delta\right)} \qquad \text{(C.1)}$$

This expression seems rather formidable and cumbersome for data analysis purposes.

Furthermore, using the differential detection technique in which we collect both I_x and I_y to yield an expression of $\left(\frac{I_x - I_y}{I_x + I_y}\right)$ does nothing so simplify the expression as will be shown presently: Collecting the vertical probe beam component gives a detected intensity of

$$I_y = D_y D_y^* = \frac{1}{4}[\sin\delta(1 - e^{i\phi}) + i\cos\delta(1 + e^{i\phi})][-\sin\delta(1 - e^{-i\phi''}) - i\cos\delta(1 + e^{-i\phi''})]$$

With simplification steps analogous to those used for I_x, we obtain an expression for I_y of:

$$\boxed{I_y = \frac{1}{4}(1 - e^{-\phi''})^2 + e^{-\phi''}\cos^2\left(\frac{1}{2}\phi' + \delta\right)} \qquad \text{(C.2)}$$

Thus,

$$I_x + I_y = \frac{1}{4}\left(1 - e^{-\phi'}\right)^2 + e^{-\phi'}\sin^2\left(\frac{1}{2}\phi' + \delta\right) + \frac{1}{4}\left(1 - e^{-\phi'}\right)^2 + e^{-\phi'}\cos^2\left(\frac{1}{2}\phi' + \delta\right)$$

$$= \frac{1}{2}\left(1 - e^{-\phi'}\right)^2 + e^{-\phi'}$$

$$I_x + I_y = \frac{1}{2}\left(1 + [\text{illegible}]\right)$$

And,

$$I_x - I_y = \frac{1}{4}\left(1 - e^{-\phi'}\right)^2 + e^{-\phi'}\sin^2\left(\frac{1}{2}\phi' + \delta\right) - \frac{1}{4}\left(1 - e^{-\phi'}\right)^2 + e^{-\phi'}\cos^2\left(\frac{1}{2}\phi' + \delta\right)$$

$$= e^{-\phi'}\left(\cos^2\left(\frac{1}{2}\phi' + \delta\right) - \sin^2\left(\frac{1}{2}\phi' + \delta\right)\right)$$

$$= e^{-\phi'}\cos\left(\phi' + 2\delta\right)$$

yielding,

$$\boxed{\frac{I_x - I_y}{I_x + I_y} = \frac{2e^{-\phi'}\cos\left(\phi' + 2\delta\right)}{1 + e^{-2\phi'}}} \qquad \text{(C.3)}$$

This expression is just as cumbersome as, and offers no improvement to, the standard OHD-OKE technique.

DOKE

By rotating the quarter-wave plate so that its long axis is oriented at 45° to horizontal and the vertically polarised probe beam, the differential detection becomes very useful. Such an arrangement is described by P(90)-λ/4(45)-S(45)-DA(0). In this

case, the probe beam has circular polarisation, after the quarter-wave plate, as it is incident on the sample.

The detector signal matrix is given by

$$D=\frac{1}{2}\begin{bmatrix}1 & 1\\ -1 & 1\end{bmatrix}\begin{bmatrix}1 & 0\\ 0 & e^{i\phi}\end{bmatrix}\begin{bmatrix}1 & 0\\ 0 & i\end{bmatrix}\begin{bmatrix}1 & -1\\ 1 & 1\end{bmatrix}\begin{bmatrix}0\\ 1\end{bmatrix}$$

$$D=\begin{bmatrix}D_x\\ D_y\end{bmatrix}=\frac{1}{2}\begin{bmatrix}-1+ie^{i\phi}\\ 1+ie^{i\phi}\end{bmatrix}$$

Separating the x and y components with a differential polariser (our Glan-laser) yields,

$$\begin{aligned}I_x = D_x D_x^* &= \frac{1}{4}\left(-1+ie^{-i\phi'}\right)\left(-1-ie^{-i\phi''}\right)\\ &= \frac{1}{4}\left(1+ie^{-i\phi'}e^{-\phi''}-ie^{i\phi'}e^{-\phi''}+e^{i\phi'-\phi''-i\phi'-\phi''}\right)\\ &= \frac{1}{4}\left(1+ie^{-\phi''}\left(e^{-i\phi'}-e^{i\phi'}\right)+e^{-2\phi''}\right)\\ &= \frac{1}{4}\left(1-2i^2\sin\phi' e^{-\phi''}+e^{-2\phi''}\right)\end{aligned}$$

$$\boxed{I_x=\frac{1}{4}\left(1+e^{-2\phi''}\right)+\frac{1}{2}\sin\phi' e^{-\phi''}} \qquad \text{(C.4)}$$

$$\begin{aligned}I_y = D_y D_y^* &= \frac{1}{4}\left(1+ie^{i\phi'}\right)\left(1-ie^{-i\phi''}\right)\\ &= \frac{1}{4}\left(1-ie^{-i\phi'}e^{-\phi''}+ie^{i\phi'}e^{-\phi''}+e^{i\phi'-\phi''-i\phi'-\phi''}\right)\\ &= \frac{1}{4}\left(1+ie^{-\phi''}\left(-e^{-i\phi'}+e^{i\phi'}\right)+e^{-2\phi''}\right)\end{aligned}$$

$$\boxed{I_y=\frac{1}{4}\left(1+e^{-2\phi''}\right)-\frac{1}{2}\sin\phi' e^{-\phi''}} \qquad \text{(C.5)}$$

$$I_x+I_y=\frac{1}{2}\left(1+e^{-2\phi''}\right)=\frac{1}{2}e^{-\phi''}\left(e^{\phi''}+e^{-\phi''}\right)=e^{-\phi''}\cosh\phi''$$

$$I_x - I_y = \sin\phi' e^{-\phi''}$$

$$\boxed{\frac{I_x - I_y}{I_x + I_y} = \frac{\sin\phi'}{\cosh\phi''}} \qquad \text{(C.6)}$$

Clearly, simply detecting I_x, as in homodyne detection gives no improvement over the traditional OHD-OKE detection. However, differential detection yields a simplified expression in Eq. C.6. In the absence of absorptive terms, all ϕ'' are zero and differential detection gives an extremely useful expression

$$\boxed{\frac{I_x - I_y}{I_x + I_y} = \sin\phi' \approx \phi'} \qquad \text{for small } \phi'. \qquad \text{(C.7)}$$

In the case of two-photon absorption terms, $\phi''\neq 0$ and there is a need to separate the real and imaginary components of the nonlinearity. With DOKE detection, there is an elegant method that may be used to accomplish this. After following the DOKE detection procedure outlined above, the polarisation of the pump may be rotated so that it is parallel to the initial polarisation the probe. Now, we have an arrangement that is described by P(90)-λ/4(45)-S(90)-DA(0). The detector signal matrix is given by

$$D = \frac{1}{2}\begin{bmatrix} 1 & 0 \\ 0 & e^{i\phi} \end{bmatrix}\begin{bmatrix} 1 & 1 \\ -1 & 1 \end{bmatrix}\begin{bmatrix} 1 & 0 \\ 0 & i \end{bmatrix}\begin{bmatrix} 1 & -1 \\ 1 & 1 \end{bmatrix}\begin{bmatrix} 0 \\ 1 \end{bmatrix}$$

$$D = \begin{bmatrix} D_x \\ D_y \end{bmatrix} = \frac{1}{2}\begin{bmatrix} -1+i \\ e^{i\phi} + ie^{i\phi} \end{bmatrix}$$

Separating the x and y components with a differential polariser (our Glan-Laser) yields,

$$I_x = D_x D_x^* = \frac{1}{4}(-1+i)(-1-i) = \frac{1}{4}(1+i-1+1)$$

$$I_x = \frac{1}{2}$$

$$I_y = D_y D_y^* = \frac{1}{4}\left(e^{i\phi} + ie^{i\phi}\right)\left(e^{-i\phi^*} - ie^{-i\phi^*}\right)$$

$$= \frac{1}{4}\left(e^{i\phi - i\phi^*} + ie^{i\phi - i\phi^*} - ie^{i\phi - i\phi^*} + e^{i\phi - i\phi^*}\right)$$

$$= \frac{1}{4}\left(2e^{i\phi' - \phi'' - i\phi' - \phi''}\right) = \frac{1}{2}e^{-2\phi''}$$

$$I_x - I_y = \frac{1}{2} - \frac{1}{2}e^{-2\phi''} = \frac{1}{2}e^{-\phi''}\left(e^{\phi''} - e^{-\phi''}\right)$$

$$= e^{-\phi''}\sinh\phi''$$

$$I_x + I_y = \frac{1}{2} + \frac{1}{2}e^{-2\phi''} = \frac{1}{2}e^{-\phi''}\left(e^{\phi''} + e^{-\phi''}\right)$$

$$= e^{-\phi''}\cosh\phi''$$

$$\boxed{\frac{I_x - I_y}{I_x + I_y} = \tanh\phi''} \qquad \text{(C.8)}$$

Clearly, if there are no absorptive terms, this expression is zero, as intuitively expected from a sample pumped with light polarised parallel to the probe beam. Since this expression only has a ϕ'' term, it may be used together with Eq. C.6 to extract the real component of the nonlinearity. Thus, the prescribed DOKE detection technique leads to simple expressions in the phase retardation and allows for easy separation of the real and imaginary terms.

Two polarisation conditions have been outlined in the preceding derivations. However, there are four useful polarisation conditions in DOKE detection. Pumping at a polarisation 45° to analyser polarisation has been shown to yield a signal given by Eq.

C.6. However, it can be shown that pumping at a polarisation -45° to analyser polarisation yields a signal that is simply a negative of Eq. C.6. Pumping with a polarisation parallel to that of the analyser was shown to yield a signal given by Eq. C.8. Likewise, it can be shown that pumping with an orthogonal polarisation to the analyser yield a signal that is the negative of Eq. C.8. Thus, there are four important polarisation conditions in the DOKE technique.

A graphical comparison

Although DOKE detection typically uses $(I_x-I_y)/(I_x+I_y)$ for signal analysis, a comparison of the transmitted light through the Kerr gate, I_x, for Homodyne, Heterodyne and Differential detection techniques is instructive. Major motivations for the DOKE layout are the linearity range and intensity levels of the signals. Figure C.1 displays the transmitted light through the Kerr gate for the three detection techniques, normalised to the total incident probe light (for purely real responses). The homodyne signal, obtained from setting $\delta=0$ in Eq. C.1, is a zero background, square dependence for small phase changes, ϕ'. The strictly-square dependence lasts only for small responses, after which the signal approaches the linear regime. It is in the beginning of this linear regime where OHD-OKE looks to reside. Setting $\delta=15°$ in Eq. C.1 provides OHD-OKE signals that are progressively linear. However, for negative phase changes, OHD-OKE signals are not linear and approach the squared power-law regime of homodyne detection. The OHD-OKE light is not detected from a zero background, instead, some "local oscillator" light provides a positive background level, improving signal-to-noise over the heterodyne technique (scattered light noise). Equation C.6 is presented in Fig. C.1, showing that DOKE signals are optically biased to give strictly-linear responses. In addition, this technique provides a larger background level, reducing the signal-to-noise from that of OHD-OKE. Furthermore, the slope of the linear range in DOKE is steeper than in OHD-OKE, providing larger signals than OHD-OKE.

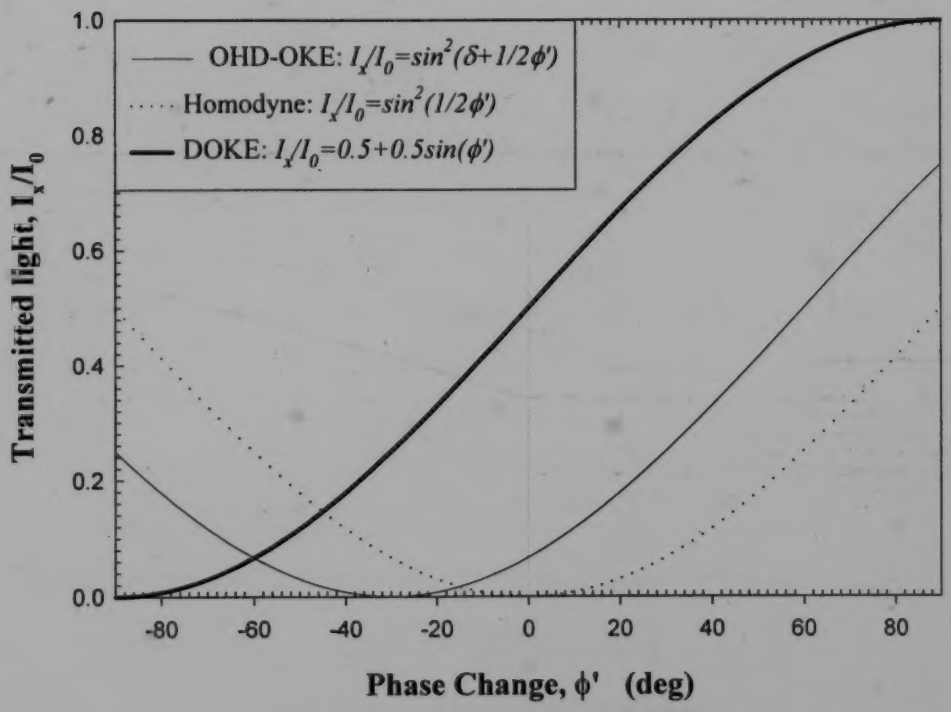

Figure C.1: **Transmitted light through the Kerr gate for three detection techniques. δ, is the heterodyning angle, where the homodyne technique operates at $\delta=0$. The OHD-OKE signal is shown for a heterodyning angle of 15°.**

Appendix D

Kerr Signals From Various Materials

As discussed in §4.4, obtaining exact third-order nonlinearity values that compare well with other literature values may not be adequate to show proper signal detection and analysis. Since $\chi^{(3)}$ values for any one material may vary by three orders of magnitude in the literature, obtaining $\chi^{(3)}$ values that don't match those obtained by other groups may not indicate improper Kerr spectroscopy. However, there are many material "finger prints" that, when obtained, may indicate proper detection of the Kerr response. This Appendix presents two such fingerprint signals—those of CS_2 and CCl_4—that match those given in the literature, and provide further indication that the DOKE detection technique works well.

In addition, the Kerr response of a thin, amorphous, arsenic-doped selenium sample is presented. Although this sample is not a typical standard in the field of Kerr spectroscopy, it does yield an interesting response profile that helps substantiate proper DOKE detection.

Carbon Tetrachloride, CCl_4

Along with tetrahydrofuran (THF), carbon disulfide (CS_2), fused silica (SiO_2) and carbon tetrachloride (CCl_4) are used as OKE standards [14,15]. CCl_4 is a symmetric molecule and does not exhibit nuclear reorientation contributions to $\chi^{(3)}$. Thus, with mere electronic components contributing to the third-order nonlinearities, CCl_4 DOKE signals should follow the pulse autocorrelation. Figure D.1 presents a typical CCl_4 DOKE signal. This time-resolved scan shows the nonlinearity in CCl_4 to be more symmetric than in THF (see, for example, Fig. 4.5), with a shorter post peak relaxation. An interesting feature in the CCl_4 profile is the rise of a post peak, long-term periodic "ringing". This feature has been previously described in the literature [26,54,55] and is attributed to optically excited phonon modes. A Fourier transform of the Kerr signal yields the

phonon frequencies [56]. Figure D.1(b) shows two clear modes excited in CCl_4. The first mode, which is somewhat broad in the figure, appears at approximately $220cm^{-1}\pm10cm^{-1}$. The second mode, which is less intense, appears at $313cm^{-1}\pm10\ cm^{-1}$. The vibrational spectrum of CCl_4 shows the actual excitations at $218cm^{-1}$ and $314cm^{-1}$ [26,54,55].

Our ability to resolve vibrational modes in samples such as CCl_4 indicates that our detection layout and resolution is exceptional. Furthermore, Figure B.1 shows a pulse width of 130fs at FWHM and a pulse duration of 90fs, confirming that CCl_4 scans can act as in-situ autocorrelations.

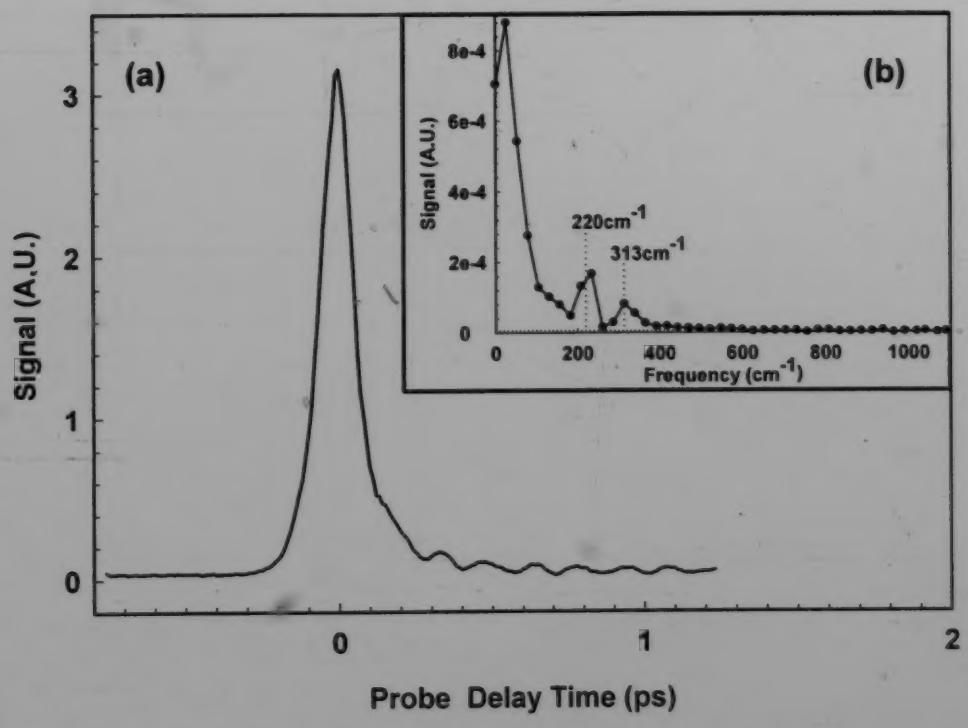

Figure D.1: Kerr response of CCl_4 showing the excitation of phonon modes. (a) Time-resolved CCl_4 Kerr signal and (b) the FFT spectrum of the Kerr response, showing the excitation of two modes at 220 cm^{-1} and 313 cm^{-1}.

Carbon Disulphide, CS_2

CS_2 is a liquid that has been used as a $\chi^{(3)}$ standard for decades. Primarily, its large nonlinearities and low absorption have made it the reference material of choice for optical Kerr spectroscopy. Furthermore, CS_2 displays large, non-instantaneous components in its nonlinear response, attributable to molecular dynamics [57]. One of the signature features of the CS_2 response is a long relaxation-time in the Kerr response. This particular feature has been attributed to molecular reorientation. Figure D.2 displays the time-resolved Kerr response of CS_2 compared to that of CCl_4. Clearly, CS_2 displays large, non-instantaneous components that are absent from the CCl4 signal which is primarily an instantaneous, electronic response. Furthermore, the molecular dynamics in CS_2 shift the peak in the Kerr signal to a positive probe delay time, indicating that the instantaneous electronic response does not dominate the overall signal. A relaxation time of 1.72 ps compares favourably with CS_2 decay times in the range of 1.7 ps to 1.79 ps reported extensively in the literature [57-60].

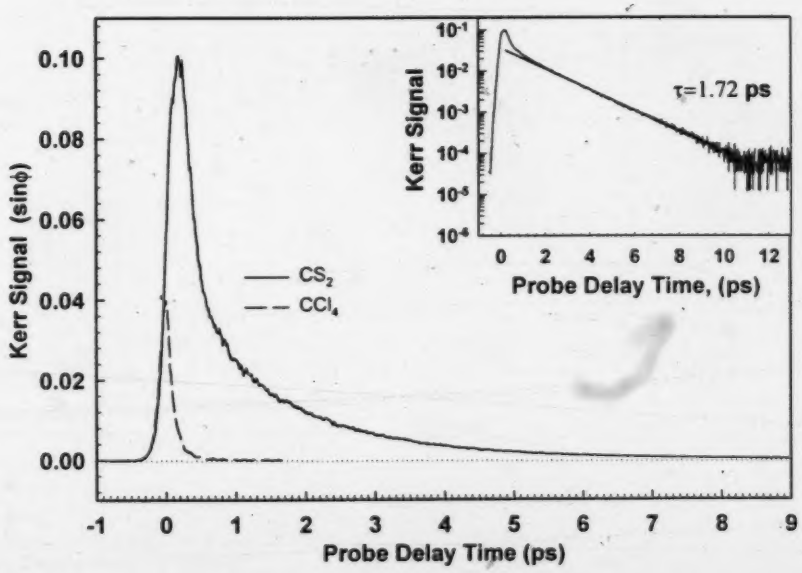

Figure D.2: Kerr signals from CS_2 and CCl_4 standards. Inset: semi-log plot showing a 1.72 ps relaxation time (straight line) in the tail of the CS_2 signal.

Amorphous Arsenic-Doped Selenium

Solid samples are typically difficult to study with OKE. However, fused silica is often used as a standard for $\chi^{(3)}$, even by OKE researchers. Since amorphous As-doped Se is expected to show two-photon absorption at 800nm, we tried to obtain a DOKE scan on a thin As-doped Se amorphous sample, with hopes of observing imaginary $\chi^{(3)}$ components. Because all of the samples and standards we previously studied showed an absence of nonlinear absorption at the pump intensities we typically use, we were hoping to see the effect of two-photon absorption on our DOKE signals. Figure D.3 shows some preliminary DOKE scans on an As-doped Se sample and a THF scan obtained as a reference. Both samples were pumped with the same pump intensity. However, the THF scans used 58 μW of probe power, while for the solid, As-doped Se sample, a 180 μW probe beam was used. This scan does not represent a quantitative study of the sample, but does show some interesting characteristics.

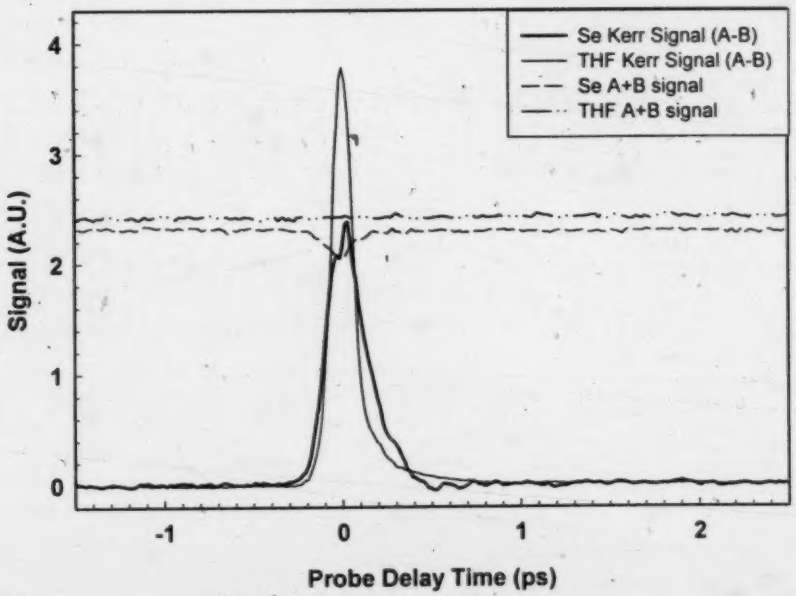

Figure D.3: DOKE responses of a 0.3 mm thick sample of arsenic-doped selenium and THF (for comparison). In addition, the post-sample probe reference signals, A+B, are provided.

First, the effects of linear absorption are apparent from the need to increase the probe power for the Se scans. The A+B signal, which acts as a post-sample probe reference is roughly at the same level for different pre-sample probe powers. The A+B THF signal is 1.04 times larger than the A+B Arsenic signal, but the pre-sample Se probe power is 3.1 times higher than that of THF. Thus, we may conclude that in order to obtain equal post-sample probe powers, the Se sample needs about 3.22 times more signal. If the drop in probe signal is due to linear absorption, a 69% probe power loss would be represented. In other words, the Se sample seems to transmit only about 31% of the probe beam in our DOKE gate. Figure D.4 shows the infrared absorption spectrum of our As-doped Se sample. The absorption spectrum reveals that at 800nm, our sample only transmits about 32% of incident light. Thus, the need for different probe powers between THF and Se samples is due to linear absorption in Se.

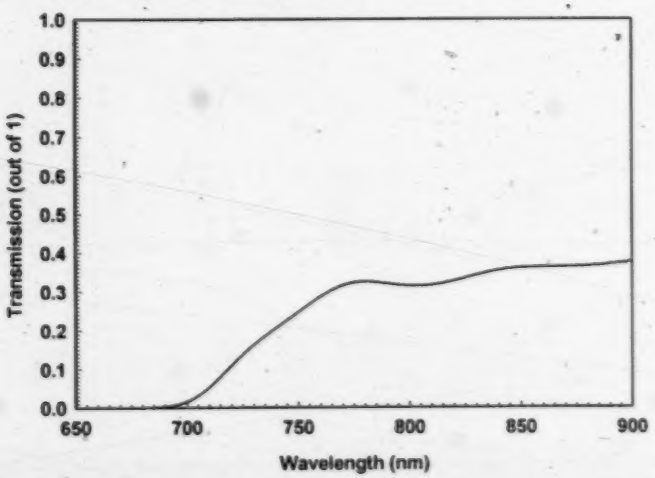

Figure D.4: Absorption spectrum of a 0.3 mm arsenic-doped selenium sample, showing considerable absorption at 800 nm.

Second, As-doped Se also presents a good example of nonlinear absorption. Unlike the A+B signal of THF, the A+B signal of the As-doped Se sample shows a transient dip in the time-domain response. The A+B baseline represents the probe power in the absence of a pump beam. However, a temporary drop in post-sample probe power

when the pump and probe beams are temporally overlapped represents nonlinear absorption. This absorption should follow the equations laid out in Appendix C. However, these scans are preliminary and the A+B data is quite noisy, preventing further analysis. This sample should be studied again to extract ϕ'' values. In addition, the sample is a thin, solid flake of glassy material and is not the ideal type of sample for Kerr spectroscopy. Nonetheless, this test shows that our DOKE system is capable of observing imaginary $\chi^{(3)}$ effects.

Finally, as with CCl_4, phonon modes in As-doped Se may be optically excited. Figure D.5 shows the post-peak Fourier transform of the As-doped Se DOKE signal. Clearly, an optical mode is excited in As-doped Se, as is seen both from the time-domain and frequency domain spectra. The DOKE signal shows the rise of a mode at $243cm^{-1} \pm 6cm^{-1}$. This mode is surrounded by other peaks that may represent other modes. The large peak at $243cm^{-1}$ is consistent with the large vibrational mode reported in the literature in the vicinity of $250cm^{-1}$ for similar amorphous selenium and arsenic/selenium glasses [60].

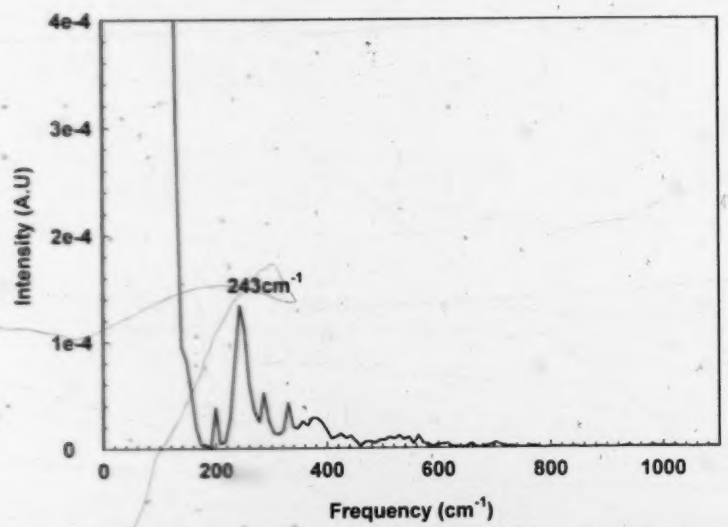

Figure D.5: FFT spectrum of the Kerr response of a 0.3 mm thick, amorphous, sample of arsenic-doped selenium. A vibrational mode is excited at 243 cm^{-1}.

Appendix E

Balanced Photodiode Schematics and Calibrations

Schematics

The balanced photodiode detector used in our DOKE measurements is a copy of another detector used for a separate experimental layout in our lab. Figure E.1 is a schematic of the detector circuitry.

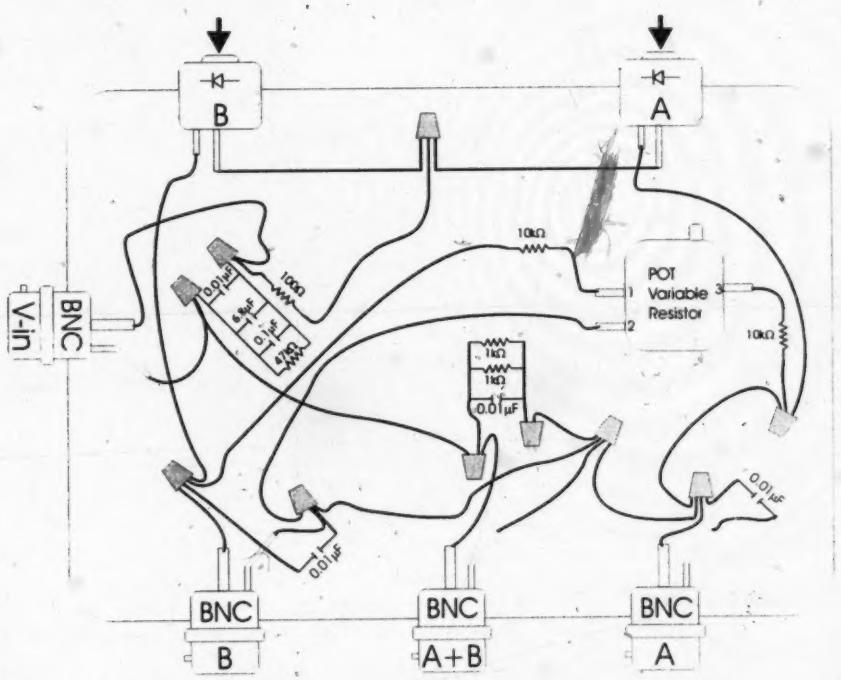

Figure E.1: A schematic of the balanced photodiodes detector used for our DOKE measurements. All details needed to build a suitable replica are provided.

The silicon photodiodes have a detection range of 5V. However, signals are kept to below 1V in all of the experiments presented in this work.

Calibration

Our detector is designed to obtain equal signals from channels A and B when equal amounts of light are incident on the two photodiodes. Furthermore, it is necessary to calibrate the detector so that A and B photodiodes contribute equally to the A+B signal output. The summing is obtained by use of a common resistor element. A variable resistor allows for careful balancing of the signals. Balancing the photodiodes is achieved as follows: a bright light source is placed far enough away from the detector to approximate parallel light incident on the photodiodes. The A+B signal is recorded when each photodiode is blocked in turn. The variable resistor is adjusted to yield equal A+B signals when either photodiode is blocked. Furthermore, the A+B output should be twice the value of that when either A or B photodiodes are blocked. It should be noted that although it is ideal for A and B photodiodes to output equal signals for equal amounts of light, a slight disparity between the photodiodes is not terribly detrimental, as long the photodiodes behave equally to light. Since we are ultimately concerned with detecting Δ(A-B), it is not crucial for the steady state signals to yield (A-B)=0. Slight offsets in photodiodes A or B do not affect the results as long as ΔA and ΔB match. In this case, it is still important to calibrate A+B such that it is equal to the sum of A+B signals when each photodiode is blocked.

"A+B" to "A"+"B" Calibration

Our main DOKE analysis equation is $\frac{A-B}{A+B}=\frac{\sin\phi'}{\cosh\phi''}$. To use this equation it is important that "A-B" signals equal signals "A"-"B" individually. Likewise, "A+B" signals must equal "A"+"B" individually. With the first there is no problem because A and B are directly input to a lock-in where the signals are subtracted. However, "A+B" signals are generated in the balanced photodiode detector where there is attenuation of the individual A and B signals before the sum is generated. Thus, the A+B output is not equal to the sum of the individual A and B signal outputs. To correct for this problem, the signals may be calibrated from the lock-in output as follows: for a given signal, output A

is sent to one lock-in amplifier, while output B is sent to a separate detector and output A+B is sent to yet a third detector. Once all signal phases and sensitivities are optimised on the lock-in amplifiers, the three lock-in output signals are read on a voltmeter. The total sum of A and B detector outputs is compared with the A+B output to obtain a calibration value. This value should be compared for various photodiode ranges to make sure that the calibration value is a constant for the range of signals typically obtained in sample scans.

For our balanced photodiodes, the calibration is given by:

$$\text{“A+B”} \times 8.0 = \text{“A”} + \text{“B”} \tag{E.1}$$

Thus, when analysing signal, 8.0(A+B) replaces A+B in our equations.

A+B as a post-sample probe reference

Throughout this work it is claimed that the balanced photodiode A+B signal acts as a probe beam reference. Intuitively, this makes sense because in DOKE detection the entire probe beam is collected after the sample. This contrasts with OHD-OKE and other detection layouts where some of the beam is rejected by the analyser. However the actual ability of A+B to act as a probe reference must be illustrated. Furthermore, to separate the horizontal from the vertical light a Wollaston prism is typically used in the field of spectroscopy [41]. Instead, we use a Glan-Laser polariser to separate the two beam polarisations. The Glan-Laser polariser is not equally efficient for both polarisations. Hence questions regarding our ability to use this polariser instead of a Wollaston must be answered. Figure E.2 presents a diagnostic test of the A+B detector. Here, the behaviour of A+B signal is examined as a function of the well-characterised pre-sample probe reference signal. The linear behaviour, as seen in Fig. E.2, indicates that our A+B detection is working properly. Our reference detection has been separately shown to be linear with light intensity, thus, so is A+B detection.

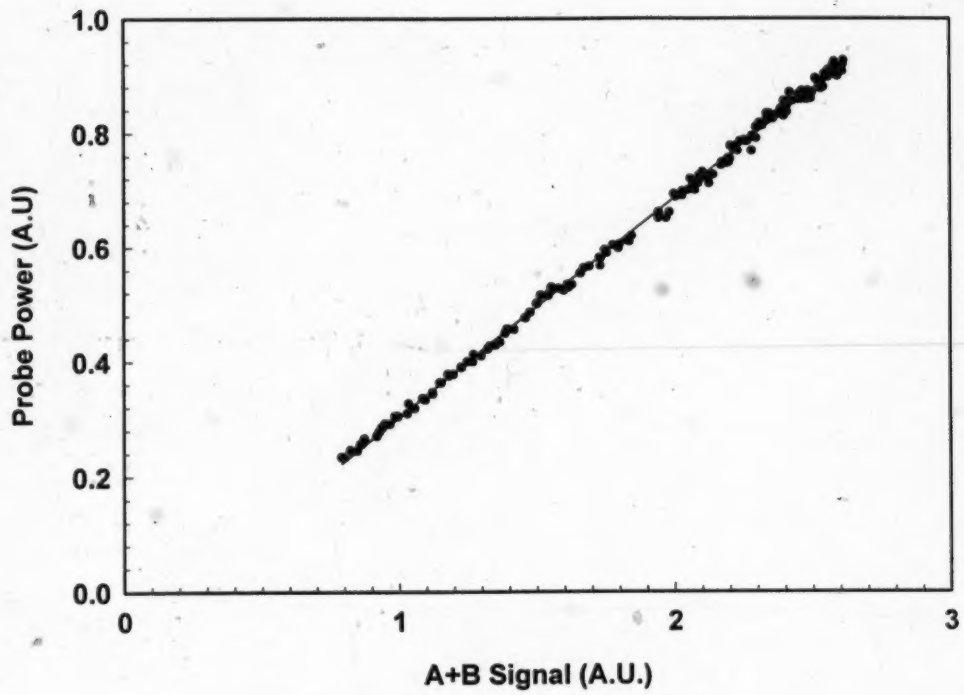

Figure E.2: **A+B detection as a true probe reference detector. Comparing A+B signal behaviour with that of a well characterised probe reference detector. A+B proves to be linear with probe power and an appropriate post-sample detector.**

Appendix F

Concentration Normalisation of $\chi^{(3)}$ Signal In Figure 5.4

OKE scans of sample nonlinearities yield the bulk third-order nonlinear susceptibilities, $\chi^{(3)}$, for that particular sample. Comparisons of various sample susceptibilities based on concentration are very difficult. Because concentration is a measure of molecular density in solution, the best way to account for concentration differences is by comparing the compounds' second hyperpolarisabilities, γ. However, time-resolved Kerr scans are direct measurements of $\chi^{(3)}$, and if scan signals are to be compared between samples of different concentrations, it is convenient to find a method for normalising these signals. Specifically, a procedure for normalising the oligomer samples' nonlinear response is required if we are to compare the type of signals presented in Fig. 5.4. Much care must be taken if the normalised signal values are to be used for comparing and reporting nonlinear values. Such care, however, is not needed if the normalisation is conducted for display purposes only. This is the case with Fig. 5.4.

As mentioned in §4.3, the nonlinear susceptibility of a sample solution may be given as a sum of nonlinearities of non-interacting components as

$$\chi^{(3)}_{sample} = \chi^{(3)}_{compound} + \chi^{(3)}_{solvent}. \qquad (F.1)$$

Where $\chi^{(3)}_{compound}$ is concentration dependent, yet when the solution is dilute, $\chi^{(3)}_{solvent}$ is considered constant. Introducing a concentration factor into Eq. F.1 provides

$$\chi^{(3)}_{sample} = [C_{compound}]\chi^{(3)}_{compound} + \chi^{(3)}_{solvent}, \qquad (F.2)$$

where $[C_{compound}]$ is the compound concentration in mol/L. To normalise compound signals (Compound A) to that of another compound (Compound B) the following relationship may be used:

$$\chi^{(3)}_{sample-A-normalized} = \left(\chi^{(3)}_{sample-A} - \chi^{(3)}_{solvent}\right)\frac{[C_{compound-B}]}{[C_{compound-A}]} + \chi^{(3)}_{solvent}, \quad \text{(F.3)}$$

where $\chi^{(3)}_{\text{sample-A-normalised}}$ is the Sample-A signal, normalised to the concentration of Sample-B. The last term in Eq. F.3 allows the normalised signal to be compared with that of the solvent signal. The signals presented in Fig. 5.4 are normalised to that of the monomer, so that, for example, the normalised pentamer signal is given by

$$\chi^{(3)}_{pentamer-normalized} = \left(\chi^{(3)}_{pentamer} - \chi^{(3)}_{THF}\right)\frac{[0.23M]}{[0.12M]} + \chi^{(3)}_{THF}. \quad \text{(F.4)}$$

In reality, the samples' nonlinear responses, and not $\chi^{(3)}$, are displayed in the figure. The nonlinear signal is, however, directly proportional to the third-order susceptibility. Furthermore, a subtraction of susceptibilities implicitly contains time-resolved signal information such that $\chi^{(3)}_{pentamer} - \chi^{(3)}_{THF}$ actually represents $\chi^{(3)}_{pentamer}(t) - \chi^{(3)}_{THF}(t)$, a subtraction of the nonlinearity time-profile. Clearly, this normalisation procedure maintains time-resolved information.

Appendix G

Sample Calculations For $\chi^{(3)}_{THF}$ and γ_{THF}

The following present sample calculations, producing the values in Eq. 5.2 and Eq. 5.3, for the bulk and molecular nonlinearities of pure THF.

Table G.1: A list of values to be used in calculating $\chi_{THF}^{(3)}$ and γ_{THF}

Variable Name	Symbol	Value
Reference phase rotation	ϕ_{ref}	0.062 ± 0.002
Blank (Cuvette) phase rotation	$\phi_{cuvette}$	0.027 ± 0.002
Spot size	D	$490\ \mu m \pm 20\ \mu m$
Pump Power	P_{Ave}	$4.0\ mW \pm 0.1\ mW$
Wavelength	λ	$800\ nm \pm 5\ nm$
Laser repetition rate	f	1000 Hz
Pulse duration	τ_{pump}	$100\ fs \pm 5\ fs$
THF Linear index of refraction	n_0	1.41
Sample interaction length	l	$1.03\ mm \pm 0.01\ mm$

In order to calculate the pump intensity per unit area, the spot area, and beam intensity must be calculated. The spot area is given by

$$A = \frac{\pi}{4} D^2 = \frac{\pi}{4} \left(4.9 x 10^{-6} m\right)^2 = \left(1.89 \pm 0.09\right) x 10^{-7} m^2 \qquad \text{(G.1)}$$

The intensity is given by

$$P_{pump} = \frac{I_{pump}}{A} = \frac{P'_{Ave}}{\tau_{pump} f} = \frac{(3.7mW)}{(1000Hz)(100fs)} = 37MW \pm 3MW \qquad \text{(G.2)}$$

where P'_{Ave} is the pump power corrected for a 7% reflection loss on the cuvette walls; $P'_{Ave} = 0.93P_{Ave}$. From Eqs. 1.19, 1.22 and G.2 we can find the induced birefringence for THF, using $\phi_{THF}=\phi_{ref}-\phi_{cuvette}$, (the responses are small enough such that $\sin\phi \approx \phi$.)

$$n'_2 = \frac{\lambda\phi}{2\pi d(3.9x10^{-6})}\frac{A}{P_{pump}} = \frac{(800nm)(0.035)(1.89x10^{-7}m^2)}{(37MW)(2\pi)(1.03mm)}$$
$$= (2.2 \pm 0.6)x10^{-20}\left(\frac{m^2}{W}\right) \qquad \text{(G.3)}$$

The third-order bulk susceptibility for THF, is then given by Eq. 1.12,

$$\chi^{(3)}_{THF} = \frac{n_0^2}{(3.9x10^{-6})}n'_2 = \frac{(1.41)^2(2.2x10^{-20})}{(3.9x10^{-6})} = (1.2 \pm 0.3)x10^{-14}esu \qquad \text{(G.4)}$$

and is reported in Eq. 5.2. Furthermore, to find the molecular second hyperpolarisability The Lorentz field factor, L^4, given by Eq. 1.15, is needed.

$$L^4 = \left(\frac{n_0^2+2}{3}\right)^4 = \left(\frac{1.41^2+2}{3}\right)^4 = 3.123 \qquad \text{(G.5)}$$

With this, we may use Eq. 1.16 to obtain γ_{THF} as,

$$\gamma_{THF} = \frac{\chi^{(3)}_{THF}}{L^4 N_c} = \frac{(1.2x10^{-14})}{(3.123)(7.4x10^{21}cm^{-3})} = (5.2 \pm 1.3)x10^{-37}esu, \qquad \text{(G.6)}$$

given in Eq. 5.3. Furthermore, this value compares favourably with $\gamma=4.8x10^{-37}$esu, presented in the literature [61].

References

1. William T. Silfvast, **Laser Fundumentals**, (Cambridge University Press, Cambridge, 1996) pp. 487-496.
2. G. I. Stegeman and A. Miller in **Photonics in Switching Vol I, Background and components**. J. E. Midwinter, editor. (Academic Press, San Diego, 1993).
3. J. L. Bredas, C. Adant, P. Tackx and A. Persoons, Chem. Rev. **94**, 243 (1994).
4. J. E. Midwinter in **Photonics in Switching Vol I, Background and components**. J. E. Midwinter, editor. (Academic Press, San Diego, 1993).
5. K. Mullen and G. Wegner, **Electronic Materials: The Oligomer Approach**. (Wiley-VCH, Chichester, 1998).
6. L-T. Cheng, W. Tam, S. R. Marder, A. E. Stiegman, G. Rikken and C. W. Spangler, J. Phys. Chem, **95**, 10643 (1991).
7. L-T. Cheng, W. Tam, S. R. Marder, A. E. Stiegman, G. Rikken and C. W. Spangler, J. Phys. Chem, **95**, 10631 (1991).
8. R. E. Martin and F. Diederich, Angew. Chem. Int. Ed. **38**, 1355 (1999).
9. R. Giesa and R. C. Shultz, Polymer International, **33**, 43 (1994).
10. A. Mathy, K. Ueberhofen, R. Schenk, H. Gregorius, R. Garay, K. Mullen, and C. Bubeck, Phys. Rev. B. **53**, 4367 (1996).
11. Christian Bosshard, **Third-Order Nonlinear Optics In Polar Materials**. Inaugural Thesis, Institute of Quantum Electronics, Zürich, Switzerland, 1998.
12. C. Bosshard, R. Preiter, P. Gunter, R. R. Tykwinski, M. Schreiber, and F. Diederich, Adv. Mater. **3**, 231 (1996).
13. R. R. Tykwinski, U. Gubler, R. E. martin, F. Diederich, C. Bosshard and P. Gunter, J. Phys. Chem. B. **102**, 4451 (1998).
14. H. S. Nalwa in **Nonlinear Optics of Organic Molecules and Polymers**. H. Nalwa and S. Miyata, editors. (CRC Press, New York, 1998) pp. 611-798.
15. **Characterisation Techniques and Tabulations for Organic Nonlinear Optical Materials**. Mark G. Kuzyk and Carl W. Dirk, editors. (Marcel Dekker, New York, 1998).
16. N. F. Phelan and M. Orchin, J. Chem. Ed, **45**, 633 (1968).

17. M. D. Levenson and G. L. Easley, Appl. Phys, **19**, 1, (1979).

18. Paras N. Prasad & David J. Williams, **Introduction To Nonlinear Optical Effects In Molecules & Polymers**, (Wiley Interscience, New York, 1991).

19. H. S. Nalwa in **Nonlinear Optics of Organic Molecules and Polymers**. H. Nalwa and S. Miyata, editors. (CRC Press, New York, 1998) pp. 571-609.

20. Paul N. Butcher and David Cotter, **The Elements of Nonlinear Optics**. (Cambridge University Press, Cambridge, 1990). pp. 79-85.

21. H. A. Lorentz, **The Theory of Electrons**. (Dover, New York, 1951).

22. Note: In this work, molecular second hyperpolarisabilities, γ, are obtained from bulk liquid solution nonlinear susceptibilities, $\chi^{(3)}$. Thus, in practice, all molecular nonlinearities presented herein are the rotationally averaged, $\langle\gamma\rangle$. However, for the sake of simplicity, these are referred to as γ in the rest of the text, and the rotational isotropy in solution is presumed.

23. William M. Robertson, **Optoelectronic Techniques for Microwave and Milimiter-Wave Engineering**. (Artech House, Boston, 1995). p. 105.

24. P. P. Ho and R. R. Alfano, Phys. Rev. A, **20**, 2170 (1979).

25. A. A. Ho in **Semiconductors Probed By Ultrafast Laser Spectroscopy, Vol II**. R. R. Alfano, editor. (Academic Press, Orlando,1984).

26. D. Mcmorrow, W. T. Lotshaw and G. A. Kenney-Wallace, IEEE J. Quant. Elec. **24**, 443 (1988).

27. M. E. Orczyk, M. Samoc, J. Swiatkiewicz and P. N. Prasad, J. Chem. Phys, **98**, 2524 (1993).

28. K. Kamada, M. Ueda, T, Sakaguchi, K. Ohta and T. Fufumi, Chem. Phys. Lett. **4263**, 215 (1996).

29. Q. Wu, M. Litz and X.-C. Zhang, Appl. Phys. Lett. **68**, 2924 (1996).

30. K. P. H. Lui and F. A. Hegmann, Appl. Phys. Lett. **78**, 3478 (2001).

31. Stephen Kershaw in Two Photon Absorption

32. Paul N. Butcher and David Cotter, **The Elements of Nonlinear Optics**. (Cambridge University Press, Cambridge, 1990). pp. 9-11,94-101.

33. D. N. Nikogosyan, Appl. Phys. A, **52**, 359 (1991).

34. C. Kalpouzos, W. T. Lotshaw, D. McMorrow and G. A. Kenney-Wallace, J. Phys. Chem, **91**, 2028 (1987).

35. D. N. Fittinghoff, B. C. Walker, J. A. Squire, C. S. Toth, C. Rose-Petruck and C. P. J. Barty, IEEE Journal of selected topics in quantum electronics, **4**, 430 (1998).

36. B. S. Prade, J. M. Schins, E. T. J. Nibbring, M. A. Franco and A. Mysyrowicz, Opt Comm. **113**, 79 (1994).

37. **Femtosecond Laser Pulses: Principles and Experiments**. C. Rulliere, editor. (Springer-Verlag, Heidelberg, 1998).

38. Y. Ishida and T. Yajima, Opt. Comm, **62**, 197 (1987).

39. K. L. Cheng, W. Bosenberg, F. W. Wise, I. A. Walmsley and C. L. Tang, Appl. Phys. Lett, **52**, 519 (1988).

40. William M. Robertson, **Optoelectronic Techniques for Microwave and Milimiter-Wave Engineering**. (Artech House, Boston, 1995). pp. 95-102.

41. **1994 Newport Catalog: Scientific and Laboratory Products**. (Newport, 1994). p. 114.

42. A ninety minute delay between reference scans is abnormally long. This delay was due to computer problems and the data would normally be rejected. However, in this case the delay was serendipitous, illustrating quite clearly the effect of drift in laser pointing.

43. K. Ohta, T, Sakaguchi, K. Kamada, and T. Fufumi, Chem. Phys. Lett. 274, 306 (1997).

44. Y. Zhao and R. R. Tykwinski, J. Am. Chem. Soc,. **121**, 458 (1999).

45. Kenji Kamada, Photonics Research Institute, National Institute of Advanced Industrial Science and Technology (AIST), Ikeda, Osaka 563-8577, Japan: **private communication**, November 2001.

46. A. Willetts, J. E. Rice and D. M. Burland, J. Chem. Phys. **97**, 7590 (1992).

47. Paul N. Butcher and David Cotter, The elements of nonlinear optics, Appendix 5. (Cambridge University Press, Cambridge, 1990) pp 306-308.

48. K. Morita, T. Suehiro, Y. Yokoh and H. Ashitaka, J. Photopolym, Sci. Technol, **6**, 229 (1993).

49. Typically, 7% of the pump beam is reflected by the cuvette walls. Thus only 93% of the pump power is incident on the sample; it is this value that is used in subsequent calculations.

50. M. E. Orczyk, M. Samoc, J. Swiatkiewicz, N. Manickam, M. Tomoaia-Cotisel and P. N. Prasad, Appl. Phys. Lett. **60**, 2837 (1992).

51. J. L. Myers and A. D. Well, **Research Design and Statistical Analysis**. (Lawrence Erlbaum Associates, Hillsdale, 1995), pp. 11-15.

52. P. N. Prasad, E. Perrin and M. Samoc, J. Chem. Phys. **91**, 2360 (1989).

53. Eugene, Hecht, **Optics, 3rd edition**. (Addison Wesley, 1998)., pp. 343, 590.

54. K. Kamada, M. Ueda, T. Sakaguchi, K. Ohta, and T. Fukumi, J. Opt. Soc. Am. B **15**, 838 (1998).

55. T. Hattori, A. Terasaki, T. Kobayashi, T. Wada, A. Yamada and H. Sasabe, J. Chem. Phys. **95**, 937 (1991).

56. Note: Figure A.1(b) presents only post-peak transformed data. Fourier transforms of the entire scan show a broad low energy component that extends beyond 300cm^{-1} and washes out the two phonon modes.

57. B. J. Loughnane, A. Scodinu, R. A. Farrer, J. T. Fourkas, and U. Mohanty, J. Chem. Phys. **111**, 2686 (1999).

58. A. Idrissi, M. Ricci, P. Bartolini, and R. Rhigini, J. Chem. Phys. **111**, 4148 (1999).

59. T. Hattori and T. Kobayashi, J. Chem. Phys. **94**, 3332, (1991).

60. N. F. Mott and E. A. Davis, **Electronic Processes in Non-crystalline Materials**, 2nd edition. (Clarendon Press, Oxford, 1979), pp. 303-306.

61. P. L. Porter, S. Guha, K. Kang and C. C. Frazier, Polymer **32**, 1756 (1991).